

NORTHWESTERN UNIVERSITY

Direct Methane Solid Oxide Fuel Cells and Their Related Applications

A DISSERTATION

SUBMITTED TO THE GRADUATE SCHOOL
IN PARTIAL FULFILLMENT OF THE REQUIREMENTS

for the degree

DOCTOR OF PHILOSOPHY

Field of Materials Science and Engineering

By

Yuanbo Lin

EVANSTON, ILLINOIS

June 2007

© Copyright by Yuanbo Lin 2006
All Rights Reserved

ABSTRACT

Direct Methane Solid Oxide Fuel Cells and Their Related Applications

Yuanbo Lin

Solid oxide fuel cells (SOFCs), renowned for their high electrical generation efficiency with low pollutant production, are promising for reducing global energy and environmental concerns. However, there are major barriers for SOFC commercialization. A primary challenge is reducing the capital cost of SOFC power plants to levels that can compete with other generation methods. While the focus of this thesis research was on operation of SOFCs directly with methane fuel, the underlying motivation was to make SOFCs more competitive by reducing their cost. This can be achieved by making SOFCs that reduce the size and complexity of the required “balance of plant”.

Firstly, direct operation of SOFCs on methane is desirable since it can eliminate the external reformer. However, effective means must be found to suppress deleterious anode coking in methane. In this thesis, the operating conditions under which SOFCs can operate stably and without anode coking were investigated in detail, and the underlying mechanisms of coking and degradation were determined. Furthermore, a novel design utilizing an inert anode barrier layer was developed and shown to substantially improve stability against coking.

Secondly, the direct methane SOFCs were investigated for use as electrochemical partial oxidation (EPOx) reactors that can co-generate electricity and synthesis gas (CO+H₂) from methane. The results indicated that conventional SOFCs work quite well as methane partial oxidation reactors, producing syngas at relatively high rates. While this approach would not decrease the cost of SOFC power plant, it would improve prospects for commercialization by increasing the value of the power plant, because two products, electricity and syngas, can be sold.

Thirdly, SOFCs utilizing thin (La,Sr)(Ga,Mg)O₃ electrolytes were demonstrated. This highly conductive material allows lower SOFC operation temperature, leading to the use of lower-cost materials for sealing, interconnection, and balance of plant. Deleterious electrolyte/electrode reactions and electrolyte La loss were avoided during high-temperature co-firing by using thin La-doped ceria barrier layers, allowing very high power densities at moderate operating temperatures. (La,Sr)(Ga,Mg)O₃-(La,Sr)(Fe,Co)O₃ composite cathodes were investigated and optimal processing parameters that yield low interfacial polarization resistance at intermediate temperature were determined.

Thesis Advisor: Prof. Scott A Barnett

Acknowledgements

I would like to thank my thesis advisor, Professor Scott Barnett, for accepting me into his research group and for the guidance, advice, encouragement, inspiration and friendship he has offered during the past five years. From the very beginning until now, the experience has been really enjoyable and definitely unforgettable. Thanks are also due to Professor Katherine Faber, Professor Harold Kung and Professor Thomas Mason for their time and help as my committee members in my qualification and the final examination. Their insights, collaborations and suggestions are greatly appreciated.

I gratefully acknowledge the financial support from the Department of Energy SECA program during the course of my research that makes my training and learning at Northwestern University as an international student possible.

I am also grateful for the training program provided by Dr. David King and Dr. Yong Wang at Pacific Northwest National Laboratory, who introduced me into the catalytic field and offered me the opportunity to work side-by-side with the most talented catalytic scientists on this planet.

I feel indebted to all the members of the Barnett Group, past and present, for their support, encouragement, contributions, and sharing, both at work and outside of it. All of them have been such invaluable resources to me. I would like to thank Dr. Jiang Liu, who led my first project here and offered me the initial momentum to overcome the barrier of solid oxide fuel cells research. I am always motivated by Dr. Zhongliang Zhan's enthusiasm and curiosity for new

research directions. Special thanks are given to Dr. Brian Madsen for his extra time and work to setup all kinds of systems. Thank you for your free service for the entire group to make the whole laboratory an easier place to work. You have set me an ideal example of good patience and willing heart to help others. Also, I would like to thank Mae Kobsiriphat, Dr. Manoj Pillai and Magna Shih for their generosity and understanding to spare the furnaces and testing systems for me. Blake Stevens, thank you for your support and tolerance to let me occupy the white testing furnace for such a long time. It is always enjoyable to talk with James Wilson and Paul Von Dollen about life and research. I was always cheered by Dr. Tammy Lai whose smile kindled the lights in the laboratory in spite of the gloomy Chicago weather. David Bierschenk, I am really glad to know you and feel lucky for you to be in this group. I believe that you will have more to appreciate when you graduate from this group.

Thank you, for your technical support, FCT members: Dr. Ilwon Kim, Dr. Yi Jiang, Dr. Negar Mansourian, John Szfraniec, Daniel Gostovic and Nikkia McDonald.

I would express my appreciations to the staff members in our department: Joanna Gwinn, Peggy Adamson, Nehala Fatima and many more. Without your support, I do not think I can make it through the graduate school so easily. Thanks should also be given to the whole department graduate students and faculty members, thank you for your service to make the graduate life so diverse and meaningful.

I would also like to acknowledge use of the following facilities at Northwestern University: the Ceramics Facility for ceramics powder processing, Optical Microscopy and Metallography Facility for sample grinding and polishing, Impedance Spectroscopy Facility for electrochemical

impedance analysis, the Electron Probe Instrumentation Center (EPIC) for use of the SEM and J. B. Cohen X-Ray Diffraction Facility for XRD analysis. More importantly, I'd like to express my gratitude to the excellent facility managers that had always been so helpful, Dr. Kathleen Stair, Jerry Carsello, Benjamin D. Myers and many more.

Finally, I would like to give special thanks to my family for all of their encouragement, support and patience. Thanks to my parents who always give me encouragement and wisdom of tackling with tough situations during my study in the United States. I would like to say, what I am today and have achieved so far is due to their influence in my life. I love you so much. To my perfect wife, Wendy, who has been such a tremendous blessing from God, I can hardly find exact words to express my appreciation of your love, understanding, support, encouragement, comfort, patience, humor, and everything else. It is impossible for me to pull through the tough time in the last stage of the graduate school without you at my side. Thank you for being in my life and I love you forever.

Table of Contents

ABSTRACT.....	3
Acknowledgements.....	5
Table of Contents.....	8
List of Tables	12
List of Figures.....	13
Chapter 1: Introduction.....	18
Chapter 2: Background.....	24
2.1 Fuel Cell Introduction.....	24
2.1.1 Fuel Cell History.....	24
2.1.2 Fuel Cell Types and Working Mechanism	24
2.1.3 Fuel Choice and Advantages of SOFC	27
2.2 Fuel Types and Fuel Processing	29
2.2.1 Hydrogen and Hydrocarbon Fuels.....	29
2.2.2 Carbon Deposition	33
2.2.3 Fuel Processing.....	36
2.2.3.1 Steam Reforming	36
2.2.3.2 Dry Reforming.....	36
2.2.3.3 Partial Oxidation.....	37
2.2.3.4 Autothermal Reforming.....	37
2.3 Direct Hydrocarbon Operation	38
2.3.1 Direct Electrochemical Oxidation Mechanism.....	38

	9
2.3.2 Internal Reforming and Electrochemical Oxidation Mechanism	39
2.4 Operating and Thermodynamic Principles of SOFC	41
2.4.1 Operating Principles.....	41
2.4.2 Thermodynamic Principles	43
2.4.3 SOFC Efficiency	45
2.4.3.1 Thermodynamic Efficiency	46
2.4.3.2 Fuel Utilization Efficiency.....	46
2.4.3.3 Electrolyte Efficiency	47
2.4.3.4 Voltage Efficiency	49
2.5 Materials of SOFCs Components	53
2.5.1 Electrolyte Materials	53
2.5.1.1 Stabilized-Zirconia Electrolyte Materials	55
2.5.1.2 Doped Ceria Electrolyte Materials.....	59
2.5.1.3 Doped Lanthanum Gallate Electrolyte Materials	60
2.5.2 Cathode Materials	62
2.5.2.1 LaMnO ₃ Based Cathode Materials	64
2.5.2.2 LaCoO ₃ Based Cathode Materials	65
2.5.3 Anode Materials.....	67
2.5.3.1 Cermet Anode	68
2.5.3.1 Ceramic Anode	71
2.6 Summary	73
Chapter 3: Direct Operation of Solid Oxide Fuel Cells with Methane Fuel.....	76
3.1 Introduction.....	76
3.2 Experimental Procedure.....	78
3.3 Experimental Results	80
3.3.1 Current-Voltage Measurements.....	80

	10
3.3.2 Cell Stability Tests.....	83
3.3.3 Electrochemical Impedance Spectroscopy (EIS).....	89
3.3.4 Mass Spectrometer Measurements	92
3.4 Discussion.....	94
3.5 Summary and Conclusions	99
Chapter 4: Improving the Stability of Direct-Methane Solid Oxide Fuel Cells Using Anode Barrier Layers	102
4.1 Introductions	102
4.2 Experimental Procedure.....	104
4.3 Results and Discussion	105
4.4 Summary and Conclusions	111
Chapter 5: High-Rate Electrochemical Partial Oxidation of Methane in Solid Oxide Fuel Cells	113
5.1 Introductions	113
5.2 Experimental Procedures	115
5.2.1 Equilibrium Calculations	115
5.2.2 Fuel Cell and Barrier Layer Preparation.....	116
5.2.3 Fuel Cell Testing and Mass Spectrometer Measurement	117
5.3 Results and Discussion	118
5.3.1 Equilibrium Calculations	118
5.3.2 SOFC Electrical Test Results.....	121
5.3.3 Product Gas Composition	124
5.4 Summary and Conclusions	129
Chapter 6: Co-Firing of Anode-Supported Solid Oxide Fuel Cells with Thin $\text{La}_{0.9}\text{Sr}_{0.1}\text{Ga}_{0.8}\text{Mg}_{0.2}\text{O}_{3-\delta}$ Electrolytes.....	131
6.1 Introduction.....	131
6.2 Experimental Procedure.....	133

	11
6.2.1 Powder Preparation	133
6.2.2 Cell Fabrication.....	134
6.2.3 Cell Testing.....	135
6.3 Results and Discussion	135
6.4 Summary and Conclusions	142
Chapter 7: A Study of $\text{La}_{0.9}\text{Sr}_{0.1}\text{Ga}_{0.8}\text{Mg}_{0.2}\text{O}_{3-\delta}$ - $\text{La}_{0.6}\text{Sr}_{0.4}\text{Fe}_{0.8}\text{Co}_{0.2}\text{O}_{3-\delta}$ Composite Cathode for Intermediate-Temperature Solid Oxide Fuel Cells Electrolytes.....	144
7.1 Introduction.....	144
7.2 Experimental Procedure.....	145
7.2.1 Fabrication of the Support Pellet	145
7.2.2 Preparation of the Symmetrical Cell.....	145
7.2.3 Electrochemical Characterization	146
7.3 Results and Discussion	147
7.3.1 Chemical Compatibility of LSGM and LSCF	147
7.3.2 Effect of Sintering Temperature	148
7.3.3 Effect of Cathode Composition	151
7.3.4 Effect of Oxygen Partial Pressure.....	155
7.3.5 Stability of LSCF-LSGM Composite Cathode.....	156
7.3.6 Cell Performance with LSCF-LSGM composite cathode	157
7.4 Summary and Conclusions	158
Chapter 8: Conclusions and Future Work.....	161
8.1 Conclusions.....	161
8.2 Future Work.....	163
References.....	165

List of Tables

Table 2.1 Summary of fuel cell types	26
Table 2.2 Comparison of energy densities for selected fuels (Values of energy densities are based on low heating value (LHV)).....	32
Table 2.3 Thermal and mechanical properties of 8-YSZ [8,38]	59
Table 2.4 Summary of the perovskite oxygen ionic conductors for electrolyte application	60
Table 2.5 List of the perovskite oxides for cathode application	63
Table 2.6 List of the perovskite oxides for cathode application [114-118,120]	72
Table 3.1 Resistance values obtained for fits to the impedance spectra in Figure 3.8.	91
Table 4.1 Steam reforming activity of barrier layer materials.....	110
Table 7.1 Summary of the total interfacial polarization resistances for the cathodes with 50wt% LSGM – 50wt% LSCF sintered at different temperatures. The electrochemical testing was taken at various temperatures from 550 to 800°C.....	150

List of Figures

Figure 2.1 Diagrams of how different fuel cells, (a) Alkaline fuel cell, (b) PEM fuel cell, (c) PAFC fuel cell, (d) molten carbonate fuel cell and (e) SOFC fuel cell, work.. Figures from Department of Energy[11].	27
Figure 2.2: Fuel cell types and the influence of fuel processing[13].	28
Figure 2.3 Calculated CO/CO ₂ ratios at equilibrium with graphitic carbon, based on reaction (2.2).	35
Figure 2.4 Current flows for a SOFC with (a) an ideal electrolyte and (b) an actual electrolyte.	47
Figure 2.5 Schematic plot of I-V curve showing voltage loss due to different polarizations [50].	52
Figure 2.6 Crystal structures of electrolyte materials: (1) fluorite structure, Oxygen ions (eight large grey balls) occupy all the face-centered cubic positions and metal cations (small black balls, Zr ⁴⁺ or Ce ⁴⁺ in this case) fill up all of the eight tetrahedral sites. (2) perovskite structure, the six large light balls in the face center positions are oxygen ions, eight grey balls (A cation, La ³⁺ for LaGaO ₃) are located on cubic vertices, the central black ball is B cation (Ga ³⁺).	54
Figure 2.7 Composition dependence of the electrical conductivity at 1000°C for (ZrO ₂) _{1-x} (Ln ₂ O ₃) _x (Ln=Sc, Yb, Er, Y, Dy, Gd) system [51].	57
Figure 2.8 Dopant concentration with highest ionic conductivity at 1000°C versus dopant cation radius curve in Figure 2.7, for ZrO ₂ -Ln ₂ O ₃ (Ln=Sc, Yb, Er, Y, Dy, Gd) system [51].	58
Figure 3.1 Schematic view of experimental setup	78
Figure 3.2 Voltage and power density vs. current density of a SOFC operated on humidified hydrogen (a) and methane (b).	80
Figure 3.3 Open circuit voltage values versus T for both hydrogen and methane. Also shown are the values predicted by assuming that the humidified methane reaches an equilibrium composition.	82
Figure 3.4 Cell voltage versus time at constant current J for SOFCs operated in humidified methane at 650 (a), 700 (b), 750 (c), and 800°C (d). The cells were operated at different J values for 3-6 h in each step, starting at high J and reducing J in steps.	85

Figure 3.5 Results of an extended SOFC test at $800\text{mA}/\text{cm}^2$ in humidified methane at 700°C	86
Figure 3.6 Fracture cross-sectional SEM micrographs and EDX spectra taken from anodes after stable SOFC operation in (a) humidified hydrogen and (b) humidified methane at 750°C , and $J = 1.2\text{A}/\text{cm}^2$ (near maximum power). Image contrast and EXD spectra did not vary with position in the anode.....	87
Figure 3.7 Cross-sectional SEM micrographs and EDX spectra from an anode after cell operation under conditions leading to performance degradation. Part (a) shows a region near the anode free surface, and part (b) shows a region near the electrolyte...	89
Figure 3.8 Electrochemical impedance spectra measured at $J = 400\text{mA}/\text{cm}^2$ and 600°C (a) and 700°C (b), for hydrogen and methane. The fitted curves were obtained using the circuit model shown in (c) with the parameters shown in Table 3.1.	90
Figure 3.9 Real-time changes in the exhaust gas composition for different cell current densities J during SOFC operation in humidified methane at 800°C , observed via the mass 44 (CO_2) signal (a) and mass 18 (H_2O) signal (b).	93
Figure 3.10 Changes in the concentrations of various species versus SOFC current density during operation in humidified methane at 800°C , derived from the mass spectrometer data.	94
Figure 3.11 Thermodynamic prediction of the equilibrium anode gas composition and fraction of CH_4 cracking to form C, assuming an input fuel composition of humidified ($\sim 3\% \text{H}_2\text{O}$) CH_4 , versus the oxygen-to-methane ratio, at 700 (a) and 800°C (b).	95
Figure 3.12 Simplified schematic illustration of how reactant and product gas concentrations are expected to vary with position during SOFC stack operation.	98
Figure 4.1 Simplified schematic illustration of how reactant and product gas concentrations are expected to vary with position during SOFC operation without (left) and with (right) barrier layers.	103
Figure 4.2 Cell voltage versus time at constant current J for SOFCs operated in humidified methane at 800°C without (a) and with (b) barrier layer. The cells were operated at different J values for 6 h in each step, starting at high J and reducing J in steps.	106
Figure 4.3 Voltage and power density versus time for a SOFC operated in humidified methane at 750°C and $0.6\text{A}/\text{cm}^2$ with barrier for $\sim 155\text{hr}$	107
Figure 4.4 Cell voltage versus time at a constant current density $J = 1 \text{ A cm}^{-2}$ for SOFCs operated in humidified methane at 750 and 800°C with (solid dots) and without (open dots) barrier.	108

- Figure 4.5 Voltage vs. current density of SOFCs with (solid dots) and without (open dots) barrier layer operated on 30sccm humidified methane at 750°C and 800°C. 109
- Figure 5.1 Schematic of fuel cell testing setup..... 118
- Figure 5.2 Predicted equilibrium fuel gas composition versus O^2-/CH_4 ratio at $T = 750^\circ C$, with the assumption that solid carbon does not form. 119
- Figure 5.3 O^2-/CH_4 ratio predicted to yield thermo-neutral SOFC operation versus cell operating voltage at 750°C. Also shown are the percentage of methane reacted and the syngas content of the product for the thermo-neutral condition. 120
- Figure 5.4 Voltage and power density versus current density (and O^2-/CH_4 ratio) for the SOFC NiO-YSZ|YSZ|YSZ-LSM, LSM, tested in 30 sccm dry methane in the anode and ambient air in the cathode at 750°C. 122
- Figure 5.5 Voltage versus time for the SOFC, Ni-YSZ|YSZ|LSM-YSZ,LSM, with a catalyst layer, Ru-CeO₂|PSZ|Ru-CeO₂, and 3.5 A ($O^2-/CH_4=0.82$). 123
- Figure 5.6 Fracture cross-sectional SEM micrographs and EDX spectra taken from anodes after stable SOFC operation in (a) humidified hydrogen and (b) dry methane at 750°C and $J = 1.46A/cm^2$ 124
- Figure 5.7 Typical mass spectra of SOFC reaction products at 750°C for 30 sccm dry methane at O^2-/CH_4 values of (a) 0, (b) 0.7 and (c) 1.16. 126
- Figure 5.8 The product gas peak intensity versus O^2-/CH_4 ratio measured during the test shown in Figure 5.4..... 127
- Figure 5.9 Methane utilization versus O^2-/CH_4 ratio for SOFCs operated on 30 sccm dry methane at 750°C. Results are compared for identical SOFCs with the standard (■) and modified (◇) gas-flow geometries indicated schematically in the insets (the arrows illustrate the fuel flow path). 128
- Figure 6.1 XRD patterns of (a) LSGM powder and (b) LDC powder prepared by solid-state reaction at 1250°C for 12hrs. 134
- Figure 6.2 Cross-sectional SEM image of a typical LDC/LSGM/LDC electrolyte tri-layer and also showing portions of the Ni-LDC anode support and LSGM-LSCF/LSCF cathode. 136
- Figure 6.3 Voltage and power density vs. current density of a thin-LSGM SOFC operated on air and humidified hydrogen with a flow rate of 100 mL/min. 138
- Figure 6.4 EDX linear scans of (a) Co, (b) Fe and (c) Ni peak intensities across the (I) Ni-LDC anode, (II) LDC buffer layer, (III) LSGM electrolyte, (IV) LDC buffer layer, and (V) LSCF-LSGM cathode..... 139

- Figure 6.5 Electrochemical impedance spectra from a thin-LSGM SOFC measured at open-circuit potential in air and humidified hydrogen. 140
- Figure 6.6 Total ohmic resistance R vs. $10000/T$ for a thin-LSGM SOFC. Shown for comparison are the calculated ohmic resistances of YSZ and LSGM thin films [172]. 141
- Figure 7.1 Schematic views of electrochemical impedance testing setup or symmetric cell EIS measurements. The upper one is a side view; lower one is a top view of the setup. 147
- Figure 7.2 XRD patterns from (a) pure LSCF powder, (b) pure LSGM powder, mixture of LSCF and LSGM (50:50 wt%) (c) after ball milling, (d) after firing at 1000°C for 4 hours, (e) 1100°C for 4 hours, (f) 1200°C for 4 hours. All peaks correspond to those for the perovskite structure. 148
- Figure 7.3 Cross-sectional SEM images of the composite cathodes (50wt% LSGM-50wt% LSCF) sintered at (a) 1000, (b) 1100, (c) 1200 and (d) 1300°C for 1 hours respectively with the LSGM substrate at the bottom. 149
- Figure 7.4 Total R_{AS} of composite cathodes as a function of LSCF content from 600 to 700°C 152
- Figure 7.5 Temperature dependence of the total R_{AS} values for different LSCF-LSGM compositions measured over a temperature range of $550\text{-}800^{\circ}\text{C}$ in air under open circuit condition. 153
- Figure 7.6 Plot of total conductivity versus temperatures for different cathode compositions. 155
- Figure 7.7 Total interfacial polarization resistance, R_{AS} , versus oxygen partial pressure for various LSCF-LSGM cathode compositions measured at 650°C 156
- Figure 7.8 Long-term stability behavior of the cathode with 70 wt% LSCF- 30wt% LSGM under a constant current load of $0.5\text{A}/\text{cm}^2$ at 650°C in air. The insert plot shows the symmetric cell under current load for the EIS measurements. 157
- Figure 7.9 Voltage and power density vs. current density of a thin-film LSGM-electrolyte SOFC, with 50wt%LSCF-50wt% LSGM cathode, operated on air and humidified hydrogen with a flow rate of 100 mL/min. 158

CHAPTER ONE

Introduction

Chapter 1: Introduction

A fuel cell is an energy conversion device that produces electricity and heat by electrochemically combining gaseous fuels (e.g. hydrogen, hydrocarbon, gasified coal) and oxidants across an ionic conductor. Fuel cells operate like batteries, but do not need to be recharged, and continuously generate electronic power as long as fuel and oxidant are replenished.

Fuel cells offer great advantages over conventional power generators: low pollutant production, low noise, high-energy conversion efficiency, modular construction to suit load, excellent load following capability and potential for cogeneration. The absence of fuel combustion limits harmful nitrous oxide, sulfur oxide and carbon dioxide emissions. Since chemical energy of the fuel is directly converted to electricity and the conversion involves no intermediate mechanical or thermal processes, fuel cells are renowned for lower noise output and higher efficiency than any other conventional technologies such as steam turbines. Efficiencies of fuel cells are not limited by the Carnot cycle of heat engines and can be further improved with the utilization of steam and heat generated from fuel cell operation for cogeneration.

Because of their excellent properties, fuel cells are being investigated for wider applications than their initial applications for space and defense. Demonstration fuel cells are powering buses, boats, trains, planes, scooters and even bicycles. Fuel cell-powered vending machines, vacuum cleaners and highway road signs have been developed as pre-commercial products. Miniature fuel cells for cellular phones, laptop computers and portable electronics are on their way to market. Hospitals, credit card centers, police stations, and banks are all using pre-commercial demonstration fuel cells to provide power to their facilities. Wastewater treatment plants and

landfills could use fuel cells to convert the methane gas they produce into electricity [1]. Fuel cells could help revolutionize the power industry with a shift from central power station plus long distribution lines to dispersed generation at the end users.

Until now, a number of fuel cell systems have been developed such as Alkaline Fuel Cells (AFC), Phosphoric Acid Fuel Cell (PAFC), Polymer Electrolyte Membrane Fuel Cell (PEMFC), Molten Carbonate Fuel Cell (MCFC) and Solid Oxide Fuel Cell (SOFC), which will be discussed later.

As a highly promising fuel cell, SOFCs have distinct advantages over other types of fuel cells: use of cheap materials, high operating temperature, no liquid involved in the fuel cell and invariant electrolyte. Adoption of solid oxides instead of noble metals like Pt as electrodes and electrolyte reduces the cost of materials. High operating temperature (generally $>600^{\circ}\text{C}$) promotes rapid reaction kinetics without noble metals and provides high-quality byproduct heat for cogeneration. The all-solid-state construction eliminates material corrosion that can occur with liquid electrolytes and can be figured into unique shapes. In summary, the SOFC is an ideal candidate for high-power applications in residential and industrial electricity generation, as well as in motor vehicles or as auxiliary power units (APU).

All types of fuel cells will operate on hydrogen gas as a fuel. However, it is difficult to store hydrogen in a useful form for fuel cell operation other than in a high-pressure tank, and the cost of supplying hydrogen is too high to be available for general public. In contrast, hydrocarbons offer a lot of advantages as the fuel for SOFCs such as higher energy density, lower cost, lower pressure for storage and ready availability. Accordingly, hydrocarbon based SOFCs have attracted worldwide investigation.

To utilize hydrocarbon fuels, most fuel cell power plants employ complete or nearly complete reforming prior to the fuel reaching the SOFCs anode. However, either additional hardware is needed; increasing the cost of the SOFC system, or the fuel is partially oxidized with an efficiency penalty. All these drawbacks would be solved with direct operation on hydrocarbon without the need for external reforming or partial oxidation. Despite the tremendous attraction of the direct operation of SOFCs on hydrocarbon, several major problems need to be solved. These include the carbon coking at the anode and impurities poisoning effect, which lead to a great loss in cell performance and a poor durability of cell operation.

Among hydrocarbons, methane, the major component of natural gas, is a widely available fuel and it poses lesser challenges in the coking than heavier hydrocarbons. Accordingly, direct-methane operation has been the focus of considerable attention. Moreover, it has been shown that SOFCs with traditional Ni-based anodes can be operated stably with methane at temperatures $<700^{\circ}\text{C}$, or at higher temperatures if a substantial cell current density is maintained [2-5].

In this thesis, the target was to realize the stable operation of SOFCs directly on methane and to explore the related applications of direct-methane SOFCs. The Ni-yttria-stabilized zirconia(YSZ) anode-supported SOFCs were addressed because they have been well developed with high power densities. Direct methane testing was carried out to determine the stable non-coking operation regime. As an effective way to depict the performance of SOFCs with time, life testing was used to map out the stable operation conditions at different temperatures. Since high current densities are desired for the stable operation of Ni-based anode without carbon coking and structure degradation at temperatures $>700^{\circ}\text{C}$, a novel design for direct methane

SOFCs was proposed, *i.e.* a separate barrier layer was introduced between the fuel stream and anode. Thus, the SOFC's operation products (CO_2 and H_2O) will not diffuse freely from the anode due to the barrier layer. The atmosphere near anode free surface, which is highly susceptible to carbon formation, will be changed so that coking is thermodynamically less favorable. Lower current densities are needed for stable operation and the non-coking regimes will be broadened at higher temperatures. At lower operation temperatures, the carbon deposition rate is much slower, however, the internal resistance from YSZ-electrolyte is too high to yield high performance due to the low oxygen-ion conductivity. Reduced temperature SOFCs with novel strontium, magnesium-doped lanthanum-gallate (LSGM) electrolyte were developed and operated with methane. The performance of anode-supported SOFCs operating at temperatures below 800°C is largely limited by the cathode due to large activation overpotentials [6,7]. LSGM-based composite cathodes were prepared and investigated to meet the performance requirements at the low operation temperatures.

Traditional SOFCs are designed to fully utilize fuels by complete oxidation of methane into CO_2 and H_2O while generating electricity and heat. Partial oxidation of methane with ceramic membrane reactors (CMR) are used to produce synthesis gas (syngas, H_2+CO), an important feedstock for the production of various chemicals including methanol and liquid hydrocarbons. With similar structure as that of CMR, SOFCs can act as electrochemical partial oxidation (EPOx) reactors to produce both electricity and syngas under appropriate conditions. The co-production of electricity and syngas improves the economics of both syngas production and fuel cell electricity production. Further work was done on CMR with novel mixed

ionic-electronic conductor (MIEC) materials to improve the oxygen conductivity in the membrane at intermediate temperature range (700-800°C).

CHAPTER TWO

Background

Chapter 2: Background

2.1 Fuel Cell Introduction

2.1.1 Fuel Cell History

The fuel cell concept dates back to early 1800s and was first demonstrated by Sir William Grove operating a hydrogen-oxygen cell with dilute sulfuric acid as the electrolyte material in 1839[8], which is generally considered as the start of fuel cell history. It was 60 years later before Nernst applied solid-oxide electrolytes, using the so-called Nernst mass (15% Y_2O_3 -doped ZrO_2) in a lamp [9]. The first working SOFC was demonstrated nearly 100 years later by Baur and Preis (1937). Their cell used the Nernst mass as an electrolyte with coke and magnetite as a fuel and oxidant, respectively[10].

2.1.2 Fuel Cell Types and Working Mechanism

The classification of fuel cells is based primarily on the type of electrolyte materials they employ. The electrolyte will determine the operation temperature range, the chemical reactions mechanism, the catalysts types and the fuel required [11]. These characteristics, in turn, affect the applications for which these cells are most suitable. There are five fuel cell types generally incorporated in the discussions on commercialization of fuel cell technology. Based on the working temperature determined by electrolyte, they can be classified into low-temperature fuel cells and high-temperature fuel cells. Alkaline Fuel Cells (AFC), Proton Exchange Membrane Fuel Cell (PEMFC), Phosphoric Acid Fuel Cell (PAFC) belong to the low-temperature system with aqueous electrolytes, while Molten Carbonate Fuel Cell (MCFC) and Solid Oxide Fuel Cell

(SOFC) are high-temperature fuel cells with molten salt or solid oxide as electrolytes. Table 2.1 shows the summary of different fuel cells [12].

A fuel cell consists of two electrodes (the anode and the cathode – where electrochemical oxidation or reduction reaction takes place) and an electrolyte (ion conductor). For a series of cells referred to as a stack, an extra component called an interconnect is used to connect the anode of one cell to the cathode of the next cell in a stack. During cell operation, a gaseous fuel is fed to the anode and oxidized with electrons released to the external circuit. An oxidant (e.g. oxygen or air) is fed to the cathode and reduced with electrons accepted from the external circuit. The electrons flowing from anode to cathode produces electricity. Figure 1.1 shows the diagrams of different fuel cells working mechanism.

Table 2.1 Summary of fuel cell types

	Proton Exchange Fuel Cell (PEFC)	Alkaline Fuel Cells (AFC)	Phosphoric Acid Fuel Cell (PAFC)	Molten Carbonate Fuel Cell (MCFC)	Solid Oxide Fuel Cell (SOFC)
Electrolyte	Solid proton exchange organic (Nafion ^a)	KOH solution (30-45% ^b or 85% ^c)	Liquid H ₃ PO ₄	Li/Na/K carbonate solution	Yttria Stabilized ZrO ₂
Operating Temperature	50 ~ 100°C	80~90 ^b or 200~250°C ^c	150 ~ 200°C	600 ~ 700°C	600 ~ 1000°C
Charge Carrier	H ⁺	OH ⁻	H ⁺	CO ₃ ²⁻	O ²⁻
Anode Catalyst	Pt or Pt/C	Pt/Pd/Au/Ni	Pt/C	Ni	Ni
Fuel	Pure Hydrogen Methanol	Pure Hydrogen	Hydrogen Reformed Natural Gas or Methanol	Hydrogen Natural Gas Gasified Coal	Hydrogen Natural Gas Gasified Coal
Applications	Back-up power Portable power Transportation	Military Space Program	Distributed generation	Electric utility Large distributed generation	Auxiliary power Electricity utility Large distributed generation

^a Registered trademark of Du Pont Inc., ^b Space Shuttle Orbiter, ^c Apollo Program

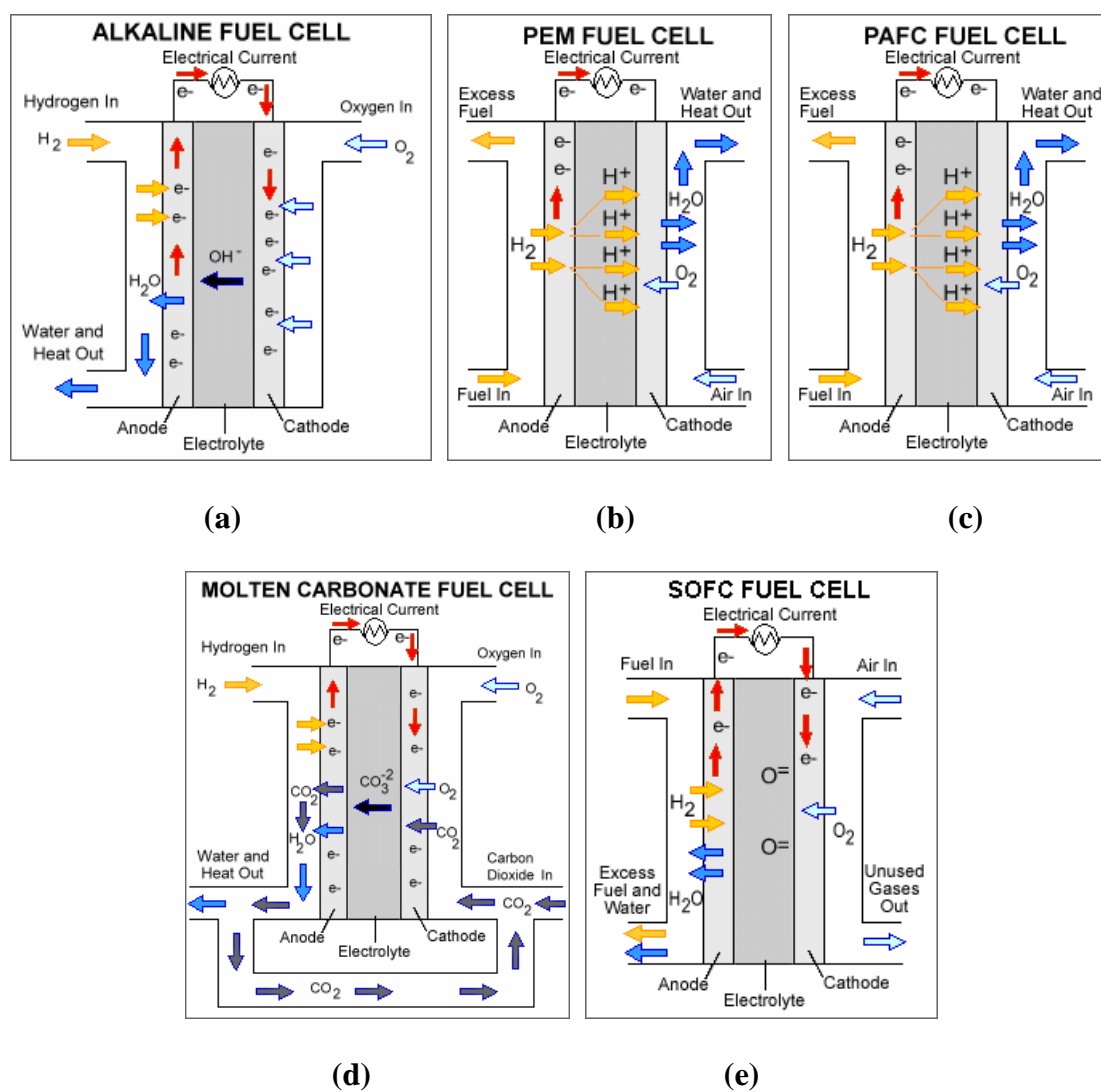


Figure 2.1 Diagrams of how different fuel cells, (a) Alkaline fuel cell, (b) PEM fuel cell, (c) PAFC fuel cell, (d) molten carbonate fuel cell and (e) SOFC fuel cell, work.. Figures from Department of Energy[11].

2.1.3 Fuel Choice and Advantages of SOFC

The choice of fuel has a significant influence on the design and commercialization of fuel cells. For AFC, PEMFC and PAFC, pretreatment of fuel is necessary to create pure hydrogen and

remove CO₂ and/or CO, which acts as a poison to the electrolyte or catalysts in electrodes. Fuel pretreatment introduces major system complexities, efficiency losses and significant cost penalties, which is illustrated in Figure 2.2.

Fuel Cell Types—Fuel Processing

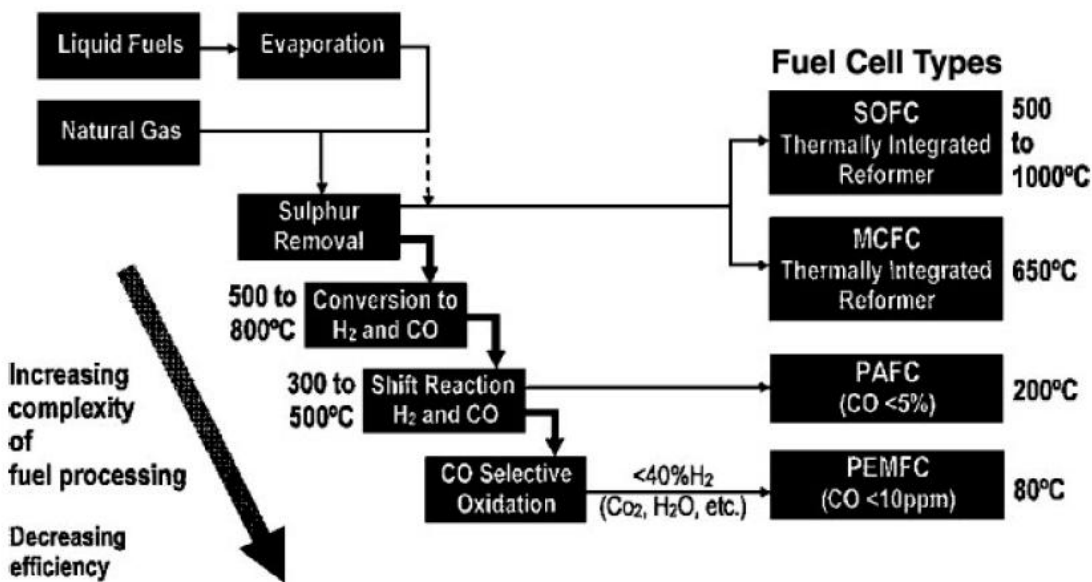


Figure 2.2: Fuel cell types and the influence of fuel processing[13].

It would be desirable to utilize hydrocarbon feedstock such as natural gas with little pretreatment in fuel cell operation. MCFC and SOFC are not prone to CO or CO₂ poisoning and even operate well on CO from reformed natural gas as fuel. Moreover, the high operating temperatures of MCFC and SOFC permit direct operation on hydrocarbon fuels by either electrochemical oxidation or reforming within the fuel cell (internal reforming), which make them the best candidates for direct utilization of hydrocarbon as fuel. However, the primary disadvantage of current MCFC technology is durability. The corrosive electrolyte plus high operation temperatures decrease cell life by accelerating component breakdown and corrosion, [11]. Because SOFC utilizes ceramics as the functional elements, the all-solid structure frees

SOFC from the plate-like construction configuration and the corrosion problems due to liquids/solutions parts typical of other fuel cell types. In addition, SOFC is also the most sulfur-resistant fuel cell type; it can tolerate several orders of magnitude more sulfur than other cell types. All these characteristics make SOFC suitable for a wide spread of applications ranging from stationary power generators (distributed power systems of 10-100kW and centralized power plants up to megawatts) to auxiliary power units for automotive and aviation.

2.2 Fuel Types and Fuel Processing

2.2.1 Hydrogen and Hydrocarbon Fuels

All types of fuel cells will operate on hydrogen gas as a fuel. SOFCs operating on hydrogen will provide better performance than by hydrocarbon. The only product from SOFCs fueled by hydrogen is water, which makes hydrogen the most environmentally hospitable fuel to decrease the greenhouse gas emission. However, hydrogen does not exist in nature in its elemental state. Now, hydrogen generation is realized either by reforming hydrocarbons, which is expensive, less efficient and emits as much greenhouse gas as combustion process, or via electrolysis of water with high-grade electricity from renewable or nuclear energy sources, which is associated with considerable energy loss. In the production processes alone, energy penalty and high cost make hydrogen less attractive as an efficient and economical energy carrier. Due to the highly-diffusive and explosive properties of hydrogen, the storage and transportation are difficult and dangerous. Even in a high-pressure tank, hydrogen storage incurs large gravimetric and volumetric energy density penalties. Additionally, the infrastructure for production, storage and transportation of hydrogen has not been established. It is estimated that the total investment in

the infrastructures needed for hydrogen economy is in the scale of trillions of dollars. All of these drawbacks will undoubtedly shadow the future of hydrogen economy.

In contrast, hydrocarbons offer many advantages over hydrogen as the fuel for SOFCs, such as ready availability, lower operation cost, easy storage and distribution, higher energy density, and established infrastructures. Take natural gas, whose major component is methane, as an example. It can be easily extracted from an estimated recoverable world reserve of 6112 trillion cubic feet by year 2006 [14]. Although the natural gas price to residential consumers has nearly doubled in the past five years, the transmission and distribution costs remain constant at around \$5 per thousand cubic feet (Mcf) [15]. The complex network of pipelines delivering natural gas to millions of residential consumers all over the country has been in service for decades. Underground storage facilities with gas inventories over trillions of cubic feet are used for withdrawal in the winter, when the additional requirements for heating cause total demand to exceed production and import capabilities. The infrastructures for natural gas production, storage and distribution, operated by government or private companies, have been well established.

Methane as well as other hydrocarbons provide much higher volumetric energy density than hydrogen. Even though hydrogen has the highest energy density by mass, for most practical applications, gravimetric energy density of gaseous or liquid energy carriers is of little relevance [16]. Most fuel storage facilities are limited by volume, especially in automotive applications. Also, the transportation capacity is determined by the pipeline diameter and the flow velocity. Therefore, in most cases, it is more meaningful to consider the energy content per unit volume. The energy densities for selected fuels are compared in Table 2.2 [17-19].

Accordingly, hydrocarbon based SOFCs have attracted worldwide investigation. Despite the tremendous attraction of the direct operation of SOFCs on hydrocarbon, several major problems need to be solved. These include the carbon deposition and impurity poisoning effects, which lead to great losses in cell performance and poor durability during cell operation.

Table 2.2 Comparison of energy densities for selected fuels (Values of energy densities are based on low heating value (LHV))

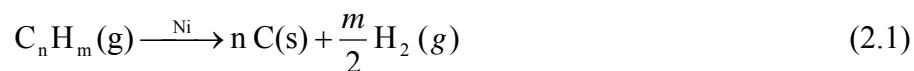
Fuel	State	Condition	Volumetric (Pre unit volume) Energy Density (MJ/Liter)	Gravimetric (Pre unit mass) Energy Density (MJ/Kg)	Molar (Per mole) Energy Density (KJ/mol)
Hydrogen	Gas	300K, 30MPa	2.0	120	240
Hydrogen	Liquid	20K, 1atm	8.5	120	240
Methane	Gas	Ambient*	21	50.1	801.6
Natural Gas	Gas	Ambient*	17.8	38.1	-**
Ethane	Gas	Ambient*	23.7	47.5	1143
LPG (Propane)	Gas/Liquid	300K, ~10atm	22.8	46.4	2042
Gasoline	Liquid	Ambient*	31.1	42.5~44.4	-**
Diesel	Liquid	Ambient*	35.0	43.0	-**
Methanol	Liquid	Ambient*	15.8	19.9	637
Ethanol	Liquid	Ambient*	21.2	26.8	1286.4
Coal	Solid	Ambient*	-	33.3	-**

*Ambient = 300K, 1atm; ** Mixtures, molecular weight unavailable;

2.2.2 Carbon Deposition

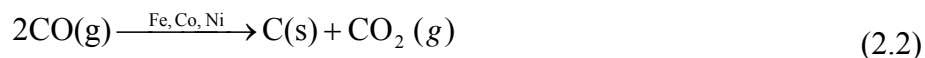
The problem of coke formation is present when carbon-containing fuels are utilized. Especially for the conventional Ni based SOFCs during direct operation on hydrocarbon, carbon deposition leads to rapid degradation and cell failure. Carbon formation occurs through several mechanisms:

Formation of filamentous or encapsulating carbon comes from hydrocarbon via thermal cracking reaction (pyrolysis) catalyzed by Ni anode or reforming catalysts like Co, Fe:



As a result, the mechanical strength incurred by filamentous carbon formation can lead to fracture of the anodes or catalyst pellets and the clogging of gas channels [20].

Another source of carbon deposition is disproportionation (Boudouard reaction) of carbon monoxide:



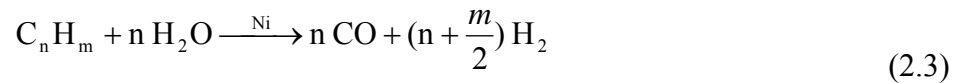
Fe and Co are reported to be most active in the CO decomposition forming amorphous flakes and filamentous carbon, which causes structure failure or disturbance of the fuel feed [21].

Other than on the catalyst surface, carbonaceous species can also form without catalysis in gas phase by free-radical cracking and polymerization. The final products, consisting of polycyclic aromatics[22], can flow with the gas stream and deposit on the anode surface. The precipitation forms a layer of non-reactive encapsulation and deactivates the catalyst surface [23]. Further cracking and condensation lead to surface carbon and tars. This type of carbon deposition is often a minor reaction for methane but severe with higher hydrocarbons.

Besides the presence of transition metals that act as coking catalysts, a number of other factors are responsible for carbon formation and deposition, which can be modified to avoid coking.

Temperature: Reaction (2.1) is an endothermic reaction, while reaction (2.2) proceeds exothermically. At low temperature, carbon deposition through reaction (2.2) will occur. As for higher temperature, direct pyrolysis of hydrocarbon will be prominent. Thus there should be a temperature window beyond which the affinity for either hydrocarbon pyrolysis or CO decomposition will be present. Indeed, based on the same argument, Barnett et al. have indicated that the optimal temperature range for SOFC stack operation on dry methane is, ~500-700°C [4].

Gas composition: Equilibria of reaction (2.1) and (2.2) are strongly dependant on the gas composition and also influenced by steam reforming (Eq. 2.3) and water-gas-shift reaction (Eq. 2.4).



Carbon free limits by thermodynamic calculation can be given as function of steam to carbon (S/C) or hydrogen to carbon (H/C) ratio. Generally, higher S/C or H/C ratio inhibits carbon formation. There also has been a simple equilibrium evaluation to determine carbon-deposition-free operation in CO-CO₂ mixtures based on reaction (2.2). As shown in Fig. 2.3, Lower CO/CO₂ ratios suppress carbon deposition at a given temperature [4].

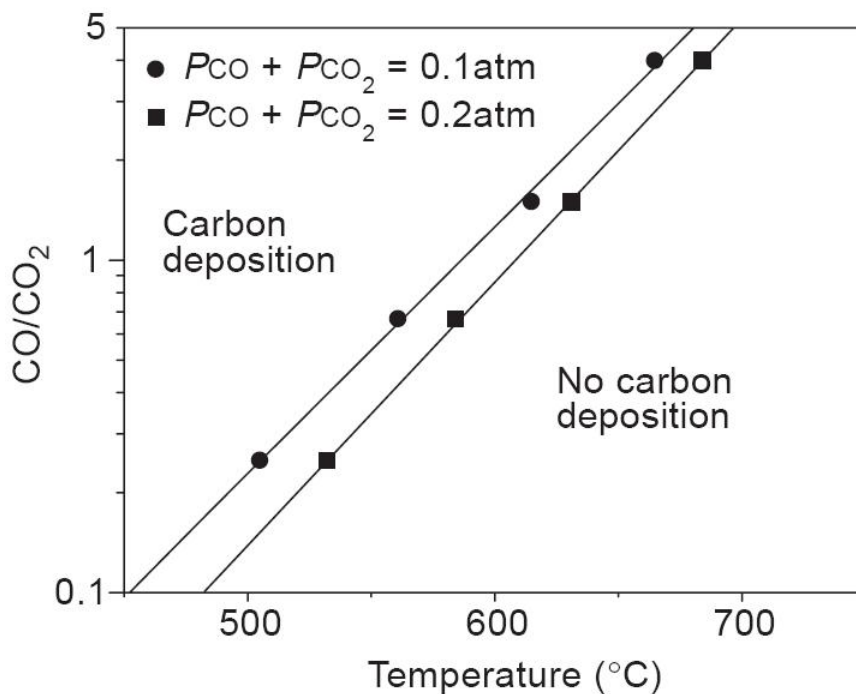


Figure 2.3 Calculated CO/CO_2 ratios at equilibrium with graphitic carbon, based on reaction (2.2).

However, great caution must be exercised in using a stability map like Figure 2.3 since kinetics instead of thermodynamics is more responsible for carbon coking.

Catalyst support: The acidity of the support has been considered important, with acidic supports such as Al_2O_3 to be avoided, and basic supports such as MgO or MgAl_2O_4 being preferred [24]. With the latter support, it is believed that adsorption of H_2O is increased, facilitating the gasification of carbon that is depositing on the surface [25].

Reaction (2.1) is inevitable with the presence of Ni in SOFC. As for reaction (2.2), it can also be catalyzed by the Ni-based SOFC anodes. Technically, there are two ways to avoid SOFC from carbon coking. One is avoiding the direct contact of hydrocarbon fuels with the anode; the other is suppressing the formation or build-up of carbon on the anode. The former is the principle of external reforming methods that hydrocarbons are converted into CO and H_2 , and then the

products are fed to fuel cell system. The latter is the foundation of direct oxidizing or internal reforming hydrocarbon within the fuel cell.

2.2.3 Fuel Processing

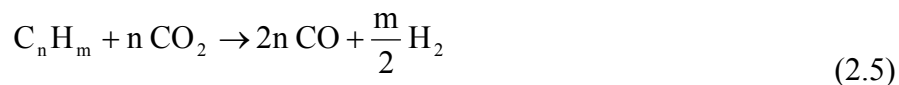
As a conventional fuel treatment processes, different reforming processes have been widely used in the production of synthesis gas (CO+H₂). According to the oxidants in the process, reforming can be classified into steam reforming, dry reforming, partial oxidation reforming and autothermal reforming (ATR).

2.2.3.1 Steam Reforming

Steam Reforming is based on reactions (2.3). The CO produced can be further utilized to generate H₂ by the shift reaction (2.4). To prevent the carbon deposition from CO decomposition reaction (2.2), steam reforming requires excessive water (generally with S/C ratio above 2) to promote shift reaction (2.4) to suppress the partial pressure of CO in the system. Even higher S/C ratio is necessary for reforming higher hydrocarbon than methane on Ni catalysts [26]. Extra costs are involved in heat exchangers and additional equipment for steam raising or recycling of the anode exhaust gas [23]. In addition, this reaction is highly endothermic. Thus, this process is also energy intensive because of the great heat demand for the reaction.

2.2.3.2 Dry Reforming

The term ‘dry reforming’ is used in comparison to steam reforming, in which CO₂ instead of H₂O is used to reform hydrocarbons on the following reaction. It is also called CO₂ reforming.



To suppress carbon deposition, an industrial process to produce CO-rich synthesis gas using a large excess of CO₂ has been adopted. High reforming temperature tends to offer carbon-free operation because of the exothermicity of CO decomposition. Various catalyst supports show a wide difference in carbon deposition rate. Among rare-earth oxides, La₂O₃ is the best [20]. While, the alkaline metal oxides (CaO or MgO) can enhance the resistance to coke formation [23]. Dry reforming is even more endothermic than steam reforming at high temperatures [27], however, CO₂ is a gaseous species and much easier to handle than steam at room temperature.

2.2.3.3 Partial Oxidation

Partial oxidation reforming uses air or oxygen to reform hydrocarbons into CO and H₂ as following:



The reaction is exothermic and part of the fuel energy was lost as heat. To avoid carbon formation, there is a lower limit for the oxygen to carbon ratio (O/C). Without the employment of steam, partial oxidation reforming has more compact design than steam reforming and is suitable for portable power system and small-scale cogeneration where system simplicity instead of system efficiency is a crucial factor.

2.2.3.4 Autothermal Reforming

Autothermal reforming integrates steam reforming with partial oxidation reforming with steam and air introduced to the fuel. Autothermal reforming needs less water and energy than steam reforming and enhances efficiency by utilizing the heat from the partial oxidation of fuels.

Autothermal reforming has a simpler design than steam reforming and higher system efficiency than partial oxidation reforming.

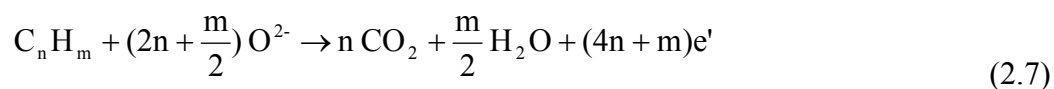
2.3 Direct Hydrocarbon Operation

To utilize hydrocarbon fuels, most fuel cell power plants employ complete or nearly complete reforming prior to the fuel reaching the SOFCs anode. However, either additional hardware is needed like steam reforming; increasing the cost of the SOFC system, or the fuel is partially oxidized with an efficiency penalty. All these drawbacks would be solved with direct operation on hydrocarbon without the need for external reforming or partial oxidation.

Possible reaction mechanisms of direct hydrocarbons operation was proposed to be either direct electrochemical oxidation of hydrocarbons [28-31], or internal reforming of hydrocarbon followed by consumption of reforming products (H_2+CO) in the fuel cell stack [32].

2.3.1 Direct Electrochemical Oxidation Mechanism

Direct electrochemical oxidation of hydrocarbons, without first reforming them into H_2 and CO , is theoretically possible in an SOFC because O^{2-} is the species that diffuses through the electrolyte. Direct hydrocarbon operation can be realized based on the hydrocarbon direct oxidation reactions:



In reaction (2.7), hydrocarbon fuels are completely oxidized by the oxygen ions from the cathode. As for reaction (2.8), hydrocarbons are partially oxidized into synthesis gas (CO+H₂). The products from partial oxidation are the same as the steam reforming. However, since the oxidant is oxygen ions instead of steam, there is less impurity in products than steam reforming. In addition, electricity is produced in this reaction. These make partial direct oxidation a potential technology for the massive production of hydrogen in industry. Compared to traditional reforming, direct oxidation can achieve both simple system design and high efficiency.

The primary difficulty encountered during direct oxidation of hydrocarbon is rapid deactivation due to carbon deposition on anode. Theoretically, it is possible to remove the carbon by direct oxidation reactions:



Electrochemical oxidation of soot has been reported [31]. Also, latest research results show that carbon deposited at or near the three phase boundaries is reversible and can be removed at a certain current load of thermodynamically carbon-free conditions [33]. By optimizing the anode microstructure or choosing appropriate cell operation conditions, carbon deposition could be reduced or even becomes negligible.

2.3.2 Internal Reforming and Electrochemical Oxidation Mechanism

Direct electrochemical oxidation of hydrocarbons, as pointed out by Marina et al. [34] and by Park, et al. [31], is unlikely to occur in one step. Even in the case of methane, the reaction (Eq. 2.11) must almost certainly occur in multiple steps to produce eight electrons.



Mogensen et al. indicate that the reaction steps at the anode proceed either by internal reforming with steam/ CO_2 from cell operation or by cracking of methane followed by electrochemical oxidation of the reforming/cracking products [32]. Despite the controversy in the literature over the precise meaning of "direct-oxidation" or "direct-utilization" of hydrocarbons in SOFC, internal reforming plus electrochemical oxidation mechanism has been widely accepted as the main process for SOFC with direct hydrocarbon operation.

Internal reforming reaction utilizes waste heat generated by fuel cell reactions and thus helps in stack thermal management. Furthermore, the products of reforming reactions (H_2+CO) are fuels for SOFC, and the SOFC operation products ($\text{H}_2\text{O}+\text{CO}_2$) are reactants for reforming reactions. Therefore, for direct hydrocarbon operation, the thermal and chemical features of the fuel cell and reforming reactions are uniquely complementary and the integration significantly increases the overall system efficiency. Besides the efficiency improvement, internal reforming eliminates the need for an external reformer and its related cost and system complexity.

In principle, direct hydrocarbon SOFC stack is simpler, more efficient and more flexible than external reforming SOFC system. However, with hydrocarbon in contact with the fuel cell, this technology faces more challenges from carbon deposition. Indeed, pre-reforming is adopted to convert higher hydrocarbons (C_2 , C_3 etc.) to methane, preventing coking on downstream reforming catalyst [35]. Among hydrocarbons, methane poses fewer challenges in the coking than higher hydrocarbons. Accordingly, direct-methane operation has been the focus of this thesis.

In summary, it would be desirable to have a fuel cell that operates directly on methane. This is the impetus for the research contained in this thesis on direct methane SOFC and its related applications.

2.4 Operating and Thermodynamic Principles of SOFC

2.4.1 Operating Principles

The operation principles of a solid-oxide fuel cell (SOFC) involves a multiple of physical and chemical processes, taking place at the same time on anode and cathode sides as well as through the electrolyte and external circuit, which is quite similar for all kinds of fuel cells and has been briefly introduced in 2.1.2. It is essential to understand the details of the operating principles of SOFC as to fully appreciate the potential of SOFC.

In this section, hydrogen and oxygen are used as fuel and oxidant for discussion. Nevertheless, the fundamentals are the same and still applicable to the cases of hydrocarbon as fuels and air as oxidant. The overall chemical reaction for SOFC is:



In reality, reaction (2.12) can be divided into individual process in cathode, anode, electrolyte and external circuit, as shown in Fig.2.3.

Cathode processes: Oxygen is fed to cathode compartment. Oxygen molecules diffuse through the porous cathode to the interface with electrolyte. On the interfacial area, there are electrochemically active sites called the triple-phase boundary (TPB), where electrochemical reactions are expected to take place. The TPB is defined as the line at which the electrolyte, the

electron-conducting phase and the gas phase all come together. The oxygen molecules are absorbed and get dissociated around the TPB, where oxygen atoms receive electrons from external circuit via electronic conductive phase at the TPB and reduction reaction occurs:



The oxygen ions formed from reaction (2.13) diffuse into the oxygen lattice vacancy in the electrolyte.

Anode processes: Hydrogen molecules take the similar path through porous anode and to the interfacial area. After absorption and dissociation, hydrogen atoms are oxidized by the oxygen ions from the electrolyte with electrons released to the external circuit via conductive phase (e.g. Ni) and interconnect, in the following reaction:



The final product steam as exhaust diffuses out of the anode into the same channels as the hydrogen supply.

Electrolyte process: Driven by the difference in oxygen chemical potential between the fuel and oxidant compartments, oxygen ions formed on the cathode side migrate through the electrolyte to the anode and consumed by hydrogen via oxidation reaction (2.14).

External circuit process: Driven by the electrical potential difference between anode and cathode, electrons released by hydrogen in Eq. (2.14) flow from anode through external load to cathode to complete the circuit. Thus, direct current electricity is generated and electrical energy is release in the process.

2.4.2 Thermodynamic Principles

An SOFC can be considered to be an oxygen permeation device. The chemical potential comes from the oxygen activity gradient (partial pressure difference for ideal gases) across the electrolyte. It is also the electromotive driving force for the electrons flowing through external circuit. The overall reaction for oxygen, which determines the cell voltage, can be represented by the following equation:



The chemical potential of oxygen at anode and cathode can be expressed in the equation (2.16) and (2.17):

$$\mu_{\text{O}_2}^{\text{anode}} = \mu_{\text{O}_2}^{\text{anode},0} + RT \cdot \ln \alpha_{\text{O}_2}^{\text{anode}} = \mu_{\text{O}_2}^{\text{anode},0} + RT \cdot \ln P_{\text{O}_2}^{\text{anode}} \quad (2.16)$$

$$\mu_{\text{O}_2}^{\text{cathode}} = \mu_{\text{O}_2}^{\text{cathode},0} + RT \cdot \ln \alpha_{\text{O}_2}^{\text{cathode}} = \mu_{\text{O}_2}^{\text{cathode},0} + RT \cdot \ln P_{\text{O}_2}^{\text{cathode}} \quad (2.17)$$

where $\mu_{\text{O}_2}^{\text{anode}}$ and $\mu_{\text{O}_2}^{\text{cathode}}$ are the oxygen chemical potentials at anode and cathode side respectively. Both $\mu_{\text{O}_2}^{\text{anode},0}$ and $\mu_{\text{O}_2}^{\text{cathode},0}$ are the chemical potential values at standard condition (STP, T=273K, P=101,325 Pa), moreover $\mu_{\text{O}_2}^{\text{anode},0} = \mu_{\text{O}_2}^{\text{cathode},0} = 0$. The parameters $\alpha_{\text{O}_2}^{\text{anode}}$ and $\alpha_{\text{O}_2}^{\text{cathode}}$ are the oxygen activities, and for an ideal gas, the activity is equal to its partial pressure $P_{\text{O}_2}^{\text{anode}}$ and $P_{\text{O}_2}^{\text{cathode}}$. The universal gas constant is R and T is absolute temperature. The Gibbs free energy change of reaction (2.15) is:

$$\Delta G = n \cdot (\mu_{\text{O}_2}^{\text{anode}} - \mu_{\text{O}_2}^{\text{cathode}}) \quad (2.18)$$

where n is the reaction molar number. Here we set n=1mol. Equations (2.16), (2.17) and (2.18) give the Gibbs free energy change for an SOFC operating with oxygen and hydrogen:

$$\Delta G = RT \cdot \ln \frac{P_{O_2}^{anode}}{P_{O_2}^{cathode}} \quad (2.19)$$

For an ideal SOFC, the chemical reaction and its related physical processes are assumed to be reversible. Theoretically, the maximum energy (electrical work, $W_{e,ideal}$) attained in the operation is equal to the Gibbs free energy change, according to the first and second laws of thermodynamics.

$$\Delta G = W_{e,ideal} = -n_e \cdot F \cdot E_{ideal} \quad (2.20)$$

where n_e is the electron number transferred in the operation (unit: mol), for this case $n_e=4$ mol per molar reaction (2.13), F is Faraday constant (96485 Coul/mol) and E_{ideal} is the theoretical electrical potential or electromotive force (EMF) across an ideal SOFC. The combination of equations (2.19) and (2.20) gives the theoretical cell voltage at open circuit (V_{OC}):

$$V_{OC} = E_{ideal} = -\frac{RT}{n_e F} \cdot \ln \frac{P_{O_2}^{anode}}{P_{O_2}^{cathode}} = \frac{RT}{4F} \cdot \ln \frac{P_{O_2}^{cathode}}{P_{O_2}^{anode}} \quad (2.21)$$

The partial pressure of oxygen in cathode, $P_{O_2}^{cathode}$, is easy to determine, while the value for $P_{O_2}^{anode}$ in the anode reducing atmosphere is hard to test. Actually, partial pressure of oxygen in anode compartment can be calculated, assuming that equilibrium state is achieved:

$$\Delta G = \Delta G^0 + RT \cdot \ln \frac{P_{H_2O}^{anode}}{P_{H_2}^{anode} \cdot (P_{O_2}^{anode})^{1/2}} \quad (2.22)$$

Substituting the equation for $P_{O_2}^{anode}$ (2.22) into (2.21) yields Nernst potential, which is also known as Nernst Equation:

$$E_{Nernst} = E_{ideal} = E_{ideal}^0 + \frac{RT}{4F} \cdot \ln \frac{(P_{H_2O}^{anode})^2}{(P_{H_2}^{anode})^2 \cdot P_{O_2}^{anode}} \quad (2.23)$$

Here, $\Delta G^0 = W_{e,\text{ideal}}^0 = -n_e \cdot F \cdot E_{\text{ideal}}^0$ is the case of Eq. (2.20) for standard state.

2.4.3 SOFC Efficiency

One of the most attractive virtues for SOFC is the potential high efficiency, which also motivates the worldwide enthusiasm for SOFC development. Just like the heat engine, SOFC is an energy converter. An effective way to elucidate the efficiency of energy conversion devices is by the comparison of the theoretical maximum efficiency (η_{max}) [36]. The theoretical efficiency for a heat engine is limited by the high (T_{high}) and low temperatures (T_{low}) in Carnot Cycle in the following equation:

$$\eta_{\text{max}} = \frac{T_{\text{high}} - T_{\text{low}}}{T_{\text{high}}} \quad (2.24)$$

For a steam turbine accepting heat generated by boiler at high temperature $T_{\text{high}} = 673\text{K}$ (400°C), part of the heat energy is converted into mechanical work and the rest lost with the water exhaust through a condenser at 333K (60°C). The maximum efficiency for this steam turbine is $(673-333)/673=0.505=50.5\%$. This value is derived on the assumption of ideal conditions, that is, all the processes are reversible. However, in practice, heat engines can rarely achieve efficiency above 40% due to different losses. It is the same for SOFC, the theoretical maximum efficiency, based on the same assumption of Eq. (2.20), is given as:

$$\eta_{\text{max}} = \frac{\Delta G}{\Delta H} \quad (2.25)$$

ΔH and ΔG are the changes in enthalpy and Gibbs free energy of reaction (2.13). It is the change in Gibbs free energy that is converted into electrical energy [37]. Thus, SOFC can achieve much higher efficiency (e.g. 83% at STP for SOFC on H_2/O_2). In reality, SOFC also

experiences irreversible losses due to resistance and polarization losses. The efficiencies of fuel cell stacks alone rarely exceed 50-60% [13].

The overall efficiency (η) of a SOFC is defined by the ratio of electrical energy ($W_{\text{electrical}}$) extracted from the fuel to the total chemical energy (E_{fuel}) contained in the fuel fed to the cell:

$$\eta = \frac{W_{\text{electrical}}}{E_{\text{fuel}}} = \frac{Q \cdot V_{\text{terminal}}}{\Delta H} \quad (2.26)$$

Q is the total charge transferred through external circuit load; V_{terminal} is the terminal voltage output by a SOFC. The overall efficiency can also be expressed by the product of thermodynamic efficiency (η_T), fuel utilization efficiency (η_F), electrolyte efficiency (η_E) and voltage efficiency (η_V):

$$\eta = \eta_T \cdot \eta_F \cdot \eta_E \cdot \eta_V \quad (2.27)$$

2.4.3.1 Thermodynamic Efficiency

Thermodynamic efficiency (η_T) is the theoretical maximum efficiency (η_{max}) in Eq. (2.25). This value sets the ceiling of the achievable efficiency for a SOFC working at a certain condition.

2.4.3.2 Fuel Utilization Efficiency

Fuel utilization efficiency (η_F) reflects the ratio of actual electrons generated in the operation to the total available in the fuel after complete oxidation. For an actual fuel cell stack, there is always some fuel unreacted or partially oxidized in the effluent gas. Indeed, some SOFC systems adopt auxiliary burner to produce heat with the un-used fuels for combined heat and power (CHP) generation [38].

2.4.3.3 Electrolyte Efficiency

Electrolyte efficiency (η_E) is determined by the electrical properties of electrolyte materials. It is the ratio of output current through external circuit (I_{external}) to the internal current by oxygen ion flux through the electrolyte (I_{oxygen}):

$$\eta_E = \frac{I_{\text{external}}}{I_{\text{oxygen}}} \quad (2.28)$$

An ideal electrolyte should be an oxygen ionic conductor as well as an electronic insulator. That is, all electrons flow through external circuit only and internal current comes entirely from oxygen ions flux ($I_{\text{external}} = I_{\text{oxygen}}$), shown in Figure 2.4(a). Thus, the electrolyte efficiency is unity. However, for actual electrolyte materials, there is always some intrinsic electronic conductivity. During operation, the leaky electron flux through electrolyte causes a loss due to electronic shorting current (I_{electron}) as in Fig. 2.4(b).

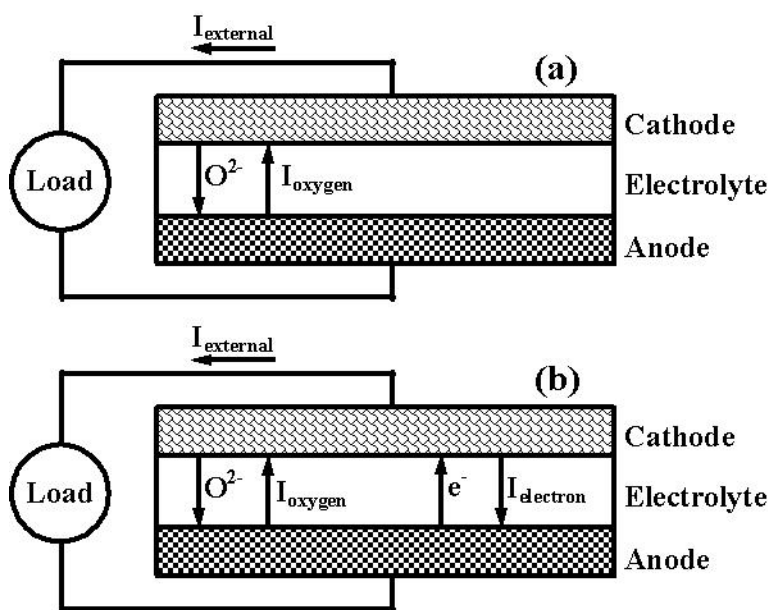


Figure 2.4 Current flows for a SOFC with (a) an ideal electrolyte and (b) an actual electrolyte.

From the conservation of charges in the cathode, it is easy to get:

$$I_{\text{external}} + I_{\text{electron}} = I_{\text{oxygen}} \quad (2.29)$$

Transport number (t), defined as “the current density due to ion B divided by the sum of current densities of all the ions in the electrolyte” [39], reflects the properties of ionic conductive materials. For SOFC electrolyte materials, there are transport numbers of electron and oxygen ion:

$$t_e = \frac{I_{\text{electron}}}{I_{\text{electron}} + I_{\text{oxygen}}} \quad (2.30)$$

$$t_o = \frac{I_{\text{oxygen}}}{I_{\text{electron}} + I_{\text{oxygen}}} \quad (2.31)$$

Notice that $t_e + t_o = 1$ and combine Eqs. (2.28)-(2.31). The electrolyte efficiency can be correlated with oxygen transport number and re-written as Equation (2.32):

$$\eta_E = 2 - \frac{1}{t_o} \quad (0.5 \leq t_o \leq 1 \text{ to ensure } I_{\text{external}} \geq 0) \quad (2.32)$$

The transport number depends on several factors such as temperature, oxygen partial pressure and materials composition. For traditional electrolyte materials, like yttria-stabilized zirconia (YSZ), the transport number is near unity in a wide range of oxygen partial pressure. The electrolyte efficiency for YSZ is that of the ideal case. In ceria-based electrolytes, the transport number is much lower in reducing atmospheres and at temperatures $>600^\circ\text{C}$. The electrolyte efficiency has a significant impact on the overall efficiency of a SOFC on doped-ceria electrolyte. The electrolyte materials and their properties will be discussed in details in section 2.5.

2.4.3.4 Voltage Efficiency

Voltage efficiency (η_V) is defined as the ratio of the cell output voltage (V_{output}) under load to the theoretical cell voltage at open circuit (V_{OC} in Eq. 2.21), and is given as:

$$\eta_V = \frac{V_{\text{output}}}{V_{\text{OC}}} \quad (2.33)$$

In the SOFC operation, the actual process is not ideal and irreversible. The cell voltage under current load is definitely less than the theoretical cell voltage due to various losses. The voltage loss is also known as polarization or overpotential, which is a function of current density. The total polarization can be broken down into three types, originating from various phenomena in the cell: charge transfer or activation polarization (ε_A), concentration or diffusion polarization (ε_D) and resistance or ohmic polarization (ε_R). The relationship between V_{output} , V_{OC} and polarizations can be written as follows:

$$V_{\text{output}} = V_{\text{OC}} - \varepsilon_A - \varepsilon_D - \varepsilon_R \quad (2.34)$$

Charge transfer or activation polarization (ε_A) reflects the energy barrier to overcome in the electrode reactions involving charge transfer. The energy barrier is also termed as activation energy. A quantitative relation between current density (i) and ε_A is given by a phenomenological theory, also known as the Butler-Volmer equation [40,41]:

$$i = i_0 \left\{ \exp\left[\frac{\beta \varepsilon_A n F}{RT}\right] - \exp\left[-\frac{(1-\beta) \varepsilon_A n F}{RT}\right] \right\} \quad (2.35)$$

where β is the transfer coefficient and i_0 is the exchange current density. n is the number of charge transferred in the reaction. The term β is a dimensionless, positive number, which gives the effect of polarization change in the reaction rate constant. i_0 reflects the forward and reverse

reaction rates at equilibrium. The higher the i_0 value is, the faster the electrode reaction is, which indicates better electrode performance. The drawback of Butler-Volmer equation is that no explicit relationship is given between i and ε_A . Limiting forms of Eq. (2.35) are given in the low and high current density regimes, which allow the simple expression of ε_A as a function of current density i .

In the low current density regime, $\left| \frac{\beta \varepsilon_A nF}{RT} \right| \ll 1$ and $\left| \frac{(1-\beta) \varepsilon_A nF}{RT} \right| \ll 1$. Eq.(2.35) can be simplified with a Taylor expansion as:

$$|\varepsilon_A| = \frac{RT}{nF i_0} i \quad (2.36)$$

In the high current density regime, $\left| \frac{\beta \varepsilon_A nF}{RT} \right| \gg 1$ or $\left| \frac{(1-\beta) \varepsilon_A nF}{RT} \right| \gg 1$. Eq.(2.35) can be approximated as:

$$\varepsilon_A \approx a + b \ln i \quad (2.37)$$

Eq.(2.37) is also referred to as the Tafel equation [40,41]. The constant a and b are related to temperature and electrode reactions. Improvement of electrodes catalytic activities is an effective way to reduce activation polarization, which can be achieved by employing highly active catalysts like Ru or Rh instead of Ni for anode [42-46], or reducing catalyst particle sizes via an impregnation method [47].

Concentration or diffusion polarization (ε_D) reflects the resistant effect to electrode reactions from mass transport. In a SOFC, the reacting species are in the gaseous phase. The mass transport of gaseous reactants and products, governed by diffusion, involves the feeding of reactants to and removing of products from electrodes. These processes must be consistent with

the net current flow through the cell. Or else, the maximum current density (i_m) achievable is limited by the diffusion polarization. Analytical expressions for maximum current density can be derived by Fick's law as follows:

$$i_m = \frac{nF \cdot p \cdot D_{\text{eff}}}{RT \cdot l} \quad (2.38)$$

where D_{eff} is the effective gaseous diffusivity of reactants; l is the electrode thickness and p is the partial pressure of reactants. Diffusion polarization can be given in terms of current density and maximum current density as:

$$\varepsilon_D = -\frac{RT}{nF} \ln\left(1 - \frac{i}{i_m}\right) \quad (2.39)$$

From Eqs. (2.38) and (2.39), it is easy to see that diffusion polarization is determined by temperature, pressure and diffusion behaviors. The diffusion is dominated not only by the gas species involved, but by the microstructure of electrode, like the porosity, pore size distribution and tortuosity. To lower this polarization, different methods like increasing electrode porosity or reducing electrode thickness have been adopted [48].

Resistance or ohmic polarization (ε_R) is the voltage loss from ohmic resistance to the motion of charge carriers (oxygen ions in electrolyte and electrons/holes in electrodes). This effect comes from ionic resistance in electrolyte and electronic resistance in electrodes and contact surfaces. The linear correlation of voltage drop and the current density can be described by Ohm's law as:

$$\varepsilon_R = (\rho_{\text{electrolyte}} l_{\text{electrolyte}} + \rho_{\text{anode}} l_{\text{anode}} + \rho_{\text{cathode}} l_{\text{cathode}} + R_{\text{contact}}) i = R_{\text{total}} \cdot i \quad (2.40)$$

where $\rho_{\text{electrolyte}}$, ρ_{anode} , ρ_{cathode} and $l_{\text{electrolyte}}$, l_{anode} , l_{cathode} are the resistivities and thickness for electrolyte, anode, cathode respectively. Their products are area specific resistances (ASRs) of

components (unit: $\Omega \cdot \text{cm}^2$), i is the current density (unit: A/cm^2) and R_{contact} is the total contact ASR. The ohmic polarization depends solely on the total resistance value (R_{total}). R_{total} is related to factors like the applied materials, working temperatures, components thicknesses. To minimize the total resistance, either new cell design (electrode-supported instead of electrolyte-supported), or new materials ($\text{La}_{0.9}\text{Sr}_{0.1}\text{Ga}_{0.8}\text{Mg}_{0.2}\text{O}$ instead of YSZ as the electrolyte) have been adopted to boost the cell performance and efficiency [49].

The schematic plot of voltage versus current density (I-V curve) demonstrating polarization effects is shown in Figure 2.5.

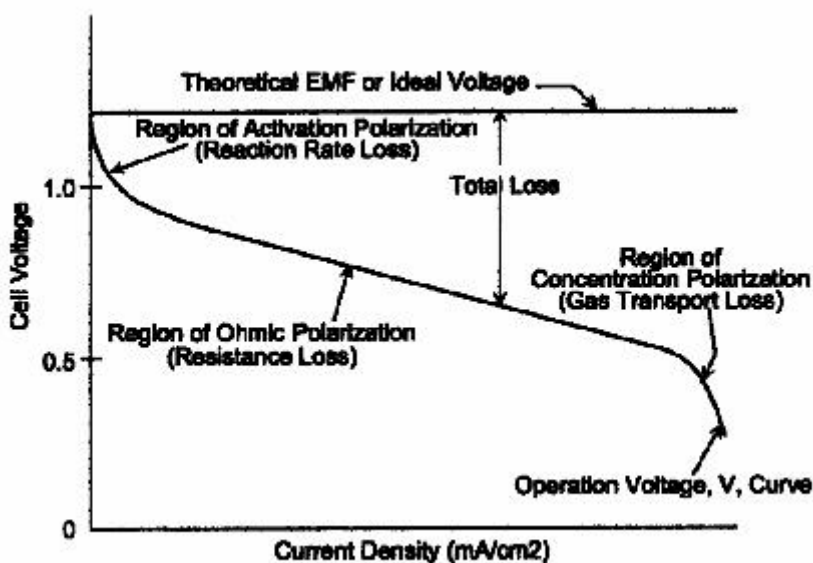


Figure 2.5 Schematic plot of I-V curve showing voltage loss due to different polarizations [50].

It is impossible to eliminate the polarizations. However, as discussed above, efficiency loss due to the voltage drop can be minimized by adopting novel materials and optimizing preparation techniques. In the next section, materials of SOFCs components and the related topics will be discussed.

2.5 Materials of SOFCs Components

SOFCs work at high temperature (600-1000°C) and face reducing and/or oxidizing atmospheres. The stability of cell components materials in such working environment is among top concerns for the satisfactory performance. To achieve high output efficiency, cell components should incur as little loss as possible. The electrical and electrochemical properties are of decisive factors in the materials selection and preparation. Moreover, each component has to function optimally by itself and in conjunction with others. Thus, there are stringent requirements of electrical, electrochemical, mechanical and chemical properties for each component material.

2.5.1 Electrolyte Materials

Electrolyte materials are solid impermeable proton or oxygen ionic conductors. For most SOFCs, oxygen anions pass from the cathode through the electrolyte to the anode. The electrolyte is critical for SOFCs to keep stable and high voltage. Electrolyte materials have to meet the following requirements for its desired function.

- High oxygen ionic conductivity and low electronic conductivity
- Thermal expansion coefficients matching with other cell components
- Stability (chemical, phase, morphological and dimensional) in reducing and oxidizing atmosphere (oxygen partial pressure P_{O_2} range: 1 to 10^{-21} atm)
- Chemical compatibility with cathode and anode materials
- Dense structure without gas leakage

Actually, only a few materials survive the screening as practical SOFC electrolytes. Among them, stabilized-zirconia (ZrO_2) and doped-ceria (CeO_2) of fluorite structure, doped lanthanum gallate (LaGaO_3) of perovskite structure are the most favored and under intensive study. The cubic fluorite structure (AO_2) and the perovskite structure (ABO_3) are shown in Figure 2.6:

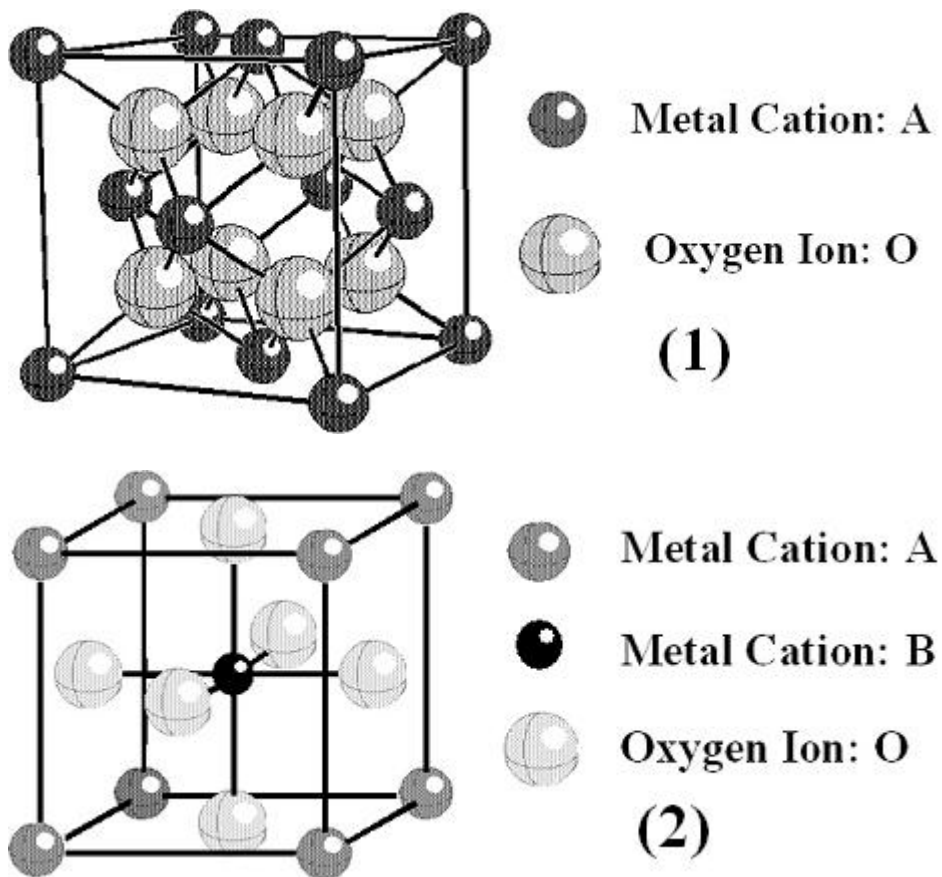
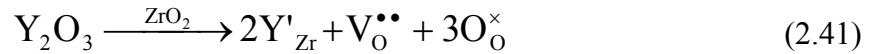


Figure 2.6 Crystal structures of electrolyte materials: (1) fluorite structure, Oxygen ions (eight large grey balls) occupy all the face-centered cubic positions and metal cations (small black balls, Zr^{4+} or Ce^{4+} in this case) fill up all of the eight tetrahedral sites. (2) perovskite structure, the six large light balls in the face center positions are oxygen ions, eight grey balls (A cation, La^{3+} for LaGaO_3) are located on cubic vertices, the central black ball is B cation (Ga^{3+}).

2.5.1.1 Stabilized-Zirconia Electrolyte Materials

Zirconia (ZrO_2) in pure phase exhibits three polymorphs at different temperature ranges: monoclinic structure from room temperature to $1170^\circ C$, tetragonal form between $1170^\circ C$ and $2370^\circ C$, cubic fluorite structure above $2370^\circ C$ to $2680^\circ C$ (melting point) [8]. Sintered ZrO_2 tends to crack due to the large volume change ($\sim 4\%$) from the phase transformation between tetragonal and monoclinic. The addition of divalent or trivalent (*i.e.* aliovalent) oxide dopants (like Y_2O_3 , Sc_2O_3 , CaO , Yb_2O_3 etc.) stabilizes the cubic fluorite structure from room temperature to melting point. At the same time, the presence of aliovalent ion introduces the oxygen vacancy by charge compensation, which enhances oxygen ionic conductivity. Take yttria-stabilized zirconia (YSZ) as an example, the incorporation reaction can be expressed in Kröger-Vink notation as follows:



The oxygen ionic conductivity is the most important property of an electrolyte material, which must be high enough to yield satisfactory performance and minimal voltage loss. Actually, as mentioned before, the conductivity value of electrolyte determines the fuel cell operation temperature and the efficiency, which can be explained by Eq. (2.42)

$$\sigma = q \cdot n \cdot \mu \quad (2.42)$$

Here q is the effective charge number for each charge carrier, for oxygen ion $q=2$; n is the charge carrier concentration, with oxygen ion concentration $n = [V_O^{\bullet\bullet}]$; μ is the mobility of charge carrier. For $[V_O^{\bullet\bullet}]$ and μ , they can be expressed as:

$$[V_O^{\bullet\bullet}] = \frac{A}{T} \exp\left(-\frac{E_a}{RT}\right) \quad (2.43)$$

$$\mu = \frac{B}{T} \exp\left(-\frac{E_m}{RT}\right) \quad (2.44)$$

where A and B are constants independent of temperature T. R is gas constant, E_a is the association binding energy to break up the union of Y_{Zr}' and $V_O^{\bullet\bullet}$ ($Y_{Zr}V_O$)' due to the Coulombic and elastic attractive forces, and E_m , termed as motion enthalpy, is the energy barrier to overcome before oxygen ions can hop into the nearest vacancy. Both E_a and E_m depends on the lattice structure of doped-ZrO₂. From Eq. (2.42)-(2.44), it is obvious that several factors like temperature, dopant species and concentration have direct influence on the conductivity of stabilized zirconia.

Temperature: The higher the operation temperature is, the higher the conductivity value will be. However, high temperature (900~1000°C) causes a lot of problems on the operation reliability of SOFC system. Actually, for SOFCs application, the current trend is to bring the operation temperature to intermediate range of 600°C-800°C. In this temperature window, the union pair or associate ($Y_{Zr}V_O$)' dissociates completely and the charge carrier concentration is independent on the temperature. Thus, the dopants are of a more feasible way to enhance the conductivity of ZrO₂. In the discussion below, conductivity of ZrO₂ with different dopants are compared at the same temperature.

Dopant Concentration: From (2.42), the conductivity is proportional to oxygen vacancy concentration. According to Eq.(2.41), with each Y₂O₃ “molecule” added, one oxygen vacancy is created, implying that the oxygen vacancy concentration changes linearly with the dopant amount. In fact, the conductivities of doped ZrO₂-M₂O₃ reach a maximum at a specific dopant quantity and then decrease with increasing dopant concentration, as shown in Figure 2.7.

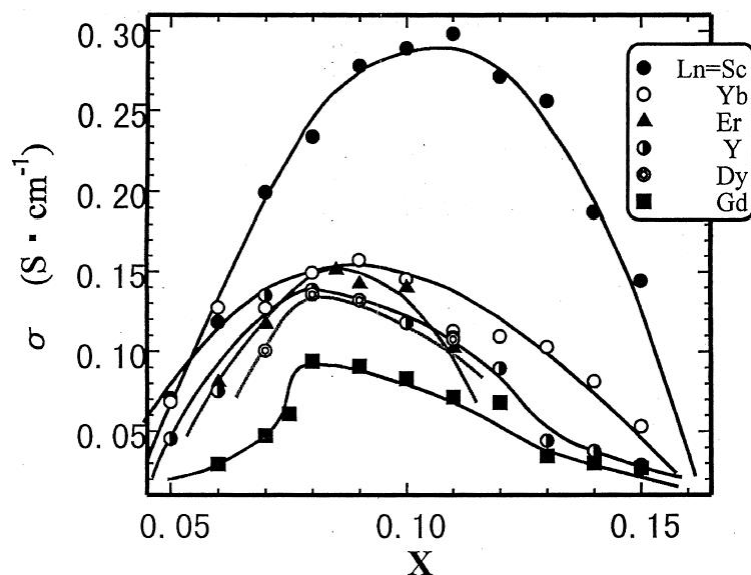


Figure 2.7 Composition dependence of the electrical conductivity at 1000°C for $(\text{ZrO}_2)_{1-x}(\text{Ln}_2\text{O}_3)_x$ ($\text{Ln}=\text{Sc}, \text{Yb}, \text{Er}, \text{Y}, \text{Dy}, \text{Gd}$) system [51].

This maximum value is obtained at or near the minimum dopant amount necessary for stabilization of cubic fluorite structure. This behavior has been attributed to vacancy clusters, structural defects or electrostatic interactions [52] and is also found to be associated with the dopant species.

Dopant Species: A group of oxides like Y_2O_3 , Sc_2O_3 , alkaline-earth oxides (CaO , MgO) and rare-earth oxides (Yb_2O_3 , Er_2O_3 , Dy_2O_3 , Gd_2O_3) can form stable solid solution ZrO_2 with acceptable ionic conductivity over wide range of composition and temperatures. Nevertheless, the ionic conductivities of ZrO_2 under the same doping level vary greatly. Moreover, the maximum achievable conductivity is determined by the dopant species. This strong correlation of ionic conductivity and dopant types can be explained by the elastic lattice strains introduced by the mismatch of host and dopant cation radius. The migration enthalpy (E_m) increases with increasing cation size difference. The larger the difference is, the more the ZrO_2 lattice is

distorted and the larger migration enthalpy is expected. Oxygen ions, with higher energy barrier to overcome, tend to show lower mobility (μ) and lower oxygen ionic conductivity (σ). Sc^{3+} has the closest ion radius to Zr^{4+} . Among all the stabilized ZrO_2 , the maximum achievable conductivity of Sc_2O_3 stabilized ZrO_2 (SSZ) is the highest achievable, as shown in Figure 2.8.

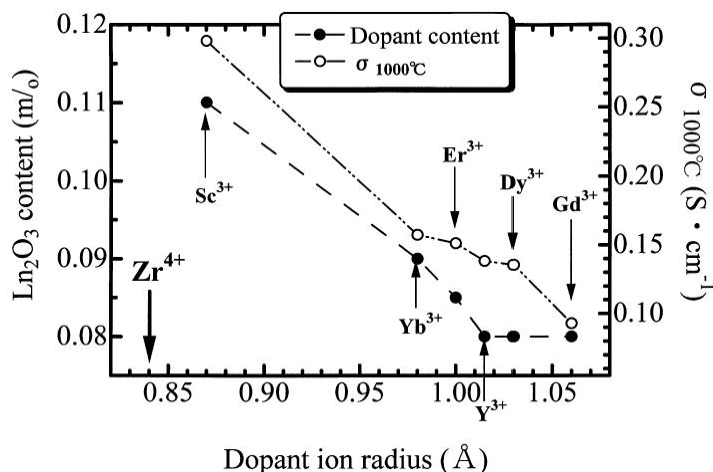


Figure 2.8 Dopant concentration with highest ionic conductivity at 1000°C versus dopant cation radius curve in Figure 2.7, for $\text{ZrO}_2\text{-Ln}_2\text{O}_3$ ($\text{Ln}=\text{Sc}, \text{Yb}, \text{Er}, \text{Y}, \text{Dy}, \text{Gd}$) system [51].

Although SSZ yields the highest conductivity, YSZ is the most common electrolyte materials and has been widely used due to its availability and lower cost. Moreover, cell preparation processes with YSZ have been well developed. In this study, YSZ is used for electrolyte material.

Mechanical properties like bending strength and fracture toughness have little room to improve due to the ionic conductivity requirement. Table 2.3 listed the thermal and mechanical properties of 8-YSZ ($\text{ZrO}_2\text{-8mol\%Y}_2\text{O}_3$). Additionally, electrolyte plays a minor role in the structural strength of SOFC stacks because electrode-supported structure is more favored over electrolyte support due to the lower operation temperature.

Table 2.3 Thermal and mechanical properties of 8-YSZ [8,38]

Materials	Bending Strength (MPa)	Thermal Expansion Coefficient (K ⁻¹)	Toughness (MPa·m ^{1/2})
ZrO ₂ -8mol%Y ₂ O ₃	230	10.5×10 ⁻⁶	2~3

2.5.1.2 Doped Ceria Electrolyte Materials

Analogous to ZrO₂, ceria (CeO₂) doped with Y₂O₃, rare-earth oxides (Gd₂O₃, Sm₂O₃) or alkaline earth oxides has fluorite structure. The dependence of ionic conductivity on dopant species and concentration is in similar manner as ZrO₂. Gd₂O₃ and Sm₂O₃ doped ceria (GDC and SDC) yield the highest ionic conductivity around doping level of 10-20mol%. The ionic conductivity of doped-ceria is around one order magnitude higher than that of YSZ. This can be attributed to the more open structure with larger ionic radius of Ce⁴⁺ than Zr⁴⁺, which makes migration enthalpy E_m in CeO₂ lower [53]. Despite the high ionic transport properties, electronic conductivity shows up at elevated temperatures in reducing atmosphere.



The lattice oxygen deficiency introduces n-type conductivity. The electronic conductivity results in low OCV and efficiency loss due to the internal short circuit. Another drawback of CeO₂ reduction is the degradation of mechanical integrity due to the lattice expansion, which causes internal stress and imposes potential problem on the stability of SOFC systems. Doped ceria as an electrolyte candidate is proposed for SOFCs working at low temperature (<600°C) [54]. At this temperature range, hydrocarbon reforming is too slow to meet SOFC operation demand. SOFCs based on ceria electrolyte are not included in this study.

2.5.1.3 Doped Lanthanum Gallate Electrolyte Materials

Doped lanthanum gallate (LaGaO_3), as a new electrolyte candidate with perovskite structure, was first reported by Ishihara et al. [55] and Goodenough et al. [56]. The perovskites represents a great number of compounds with the general formula of ABO_3 . The total charges on A and B cation site (+6) allows multiple combinations like 1+5, 2+4 and 3+3 [38]. This structure can be further modified with doping on A and/or B sites with great variety of cations and concentrations. Perovskites have found wide applications in dielectrics, superconductor, oxygen catalysts and SOFCs [57].

Strontium, magnesium doped lanthanum gallate ($\text{La}_{1-x}\text{Sr}_x\text{Ga}_{1-y}\text{Mg}_y\text{O}_{3-\delta}$, also as LSGM) belongs to a group of perovskites as electrolyte candidate materials. Besides La, the A site can be of Pr, Nd, Sm, Y, Yb or Gd. The A site can be doped with other alkaline earth cations like Ca, Sr or Ba. B site can be Al or Ga. The B site dopant is generally Mg plus transition metal cations like Cr, Fe, Co, Ni, Cu or Mn. Table 2.4 summarizes the perovskite oxygen ionic conductors is lists.

Table 2.4 Summary of the perovskite oxygen ionic conductors for electrolyte application

Site	A site	A site dopant	B site	B site dopant
Cations	Pr^{3+} , La^{3+} , Nd^{3+} , Sm^{3+} , Y^{3+} , Yb^{3+} , Gd^{3+}	Ca^{2+} , Sr^{2+} , Ba^{2+}	Al^{3+} , Ga^{3+} , Ti^{4+}	Mg^{2+} , Fe^{2+} , Co^{2+} , Ni^{2+} , Cr^{2+} , Cu^{2+} , Mn^{2+}

Before the discovery of Ga-based perovskites (AGaO_3), Takahashi and Iwahara investigated Al- and Ti-based (AAIO_3 , ATiO_3) perovskite oxides [58]. However, these oxides give lower

ionic conductivity than YSZ and sometimes exhibit hole conduction. For Ga-based perovskite oxides, the ionic size of A site cation is significant in determining the oxygen ionic conductivity [59]. The ionic conductivity increases with increasing ionic radii of A site cation, in the order of $\text{Pr} > \text{La} > \text{Nd} > \text{Sm}$ for the case of Ca-doped LnGaO_3 ($\text{Ln}=\text{La}, \text{Pr}, \text{Nd}, \text{Sm}$) [55]. Due to the cost and availability, La instead of Pr is applied in the electrolyte materials. The dopant species on the A site also have strong influence on conductivity of LaGaO_3 in the order of $\text{Sr} > \text{Ba} > \text{Ca}$. The amount of Sr directly influences the oxygen vacancy concentration. Without Mg dopant on the B site, the maximum solubility of Sr on La site is only 10mol%, or else secondary phase like SrGaO_3 or La_4SrO_7 will form. The introduction of Mg not only increases the solubility of Sr up to 20mol%, but also forms new oxygen vacancies. According to the literature, the highest ionic conductivity was achieved at composition of $\text{La}_{0.8}\text{Sr}_{0.2}\text{Ga}_{1-y}\text{Mg}_y\text{O}_{3-\delta}$ ($y=0.15-0.2$) [60-62]. It has been found that oxygen ionic conductivity increased with further doping on the B site with a small amount of Ni or Co in substitution of Mg [63,64]. The conductivity value of LSGM is comparable to or even higher than those of GDC and SDC. Unlike the electronic conduction of GDC and SDC at higher temperature ($>600^\circ\text{C}$) in reducing atmosphere, LSGM maintains pure ionic conductance over the whole oxygen partial pressure range of SOFC operation up to 1000°C . LSGM is an advantageous electrolyte material over SDC/GDC in intermediate-temperature range ($650-700^\circ\text{C}$) in terms of conductivity.

The major drawback of LSGM is its stability. LSGM is very reactive due to the La cation diffusion. LSGM can react with NiO in the anode to form the insulating phase of LaNiO_3 , which dramatically increases the resistance and voltage loss. With La cation depletion from or enrichment to LSGM, secondary phases like $\text{LaSrGa}_3\text{O}_7$ or LaSrGaO_4 with low conductivity was

observed [54]. La-doped ceria as reaction and diffusion barrier was incorporated between electrolyte and anode/cathode. The chemical stability of $\text{La}_{0.8}\text{Sr}_{0.2}\text{Ga}_{0.8}\text{Mg}_{0.2}\text{O}_{3-\delta}$ itself is not high and secondary phases were frequently detected in materials preparation and SOFC operation atmosphere [65]. $\text{La}_{0.9}\text{Sr}_{0.1}\text{Ga}_{0.8}\text{Mg}_{0.2}\text{O}_{3-\delta}$ is adopted as the more stable composition for SOFC electrolyte.

LSGM possesses similar mechanical strength to doped ceria, only slightly weaker than YSZ [66,67]. Nevertheless, addition of Al_2O_3 will greatly improve the mechanical strength [68].

With higher oxygen ionic conductivity, LSGM is selected as SOFC electrolyte materials for intermediate temperature operation in this work.

2.5.2 Cathode Materials

As discussed in Section 2.4.1, Cathode materials act as oxygen-reducing catalysts and electronic conductors in the oxygen reduction process. Cathode materials have to possess the following properties for its proper function.

- High catalytic activity to electrochemical reduction of oxygen
- High electronic conductivity
- Chemical compatibility with adjacent components (electrolyte and interconnect)
- Thermal expansion coefficients (TEC) matching with other cell components
- Stability (chemical, phase, morphological and dimensional) in different oxygen partial pressure
- Large surface area and porosity to accelerate the reduction and diffusion of oxygen

Due to the high operating temperature of SOFCs in oxidizing atmosphere, only noble metals or electronic conducting oxides can be used as cathode materials. At present, perovskite oxides, rather than noble metals like Pt, Pd and Ag, are commonly used as practical cathode materials because of the cost competitiveness [8,38]. As mentioned in the previous sections, perovskite materials show a large variety of composition and properties due to their extreme amenability to modification via doping on A and/or B sites. The same rule holds for perovskite cathode candidates. Table 2.5 lists perovskite oxides (with dopants) proposed or applied as potential cathode materials.

Table 2.5 List of the perovskite oxides for cathode application

Site	A site	A site dopant	B site	B site dopant
Cations	Pr ³⁺ , La ³⁺ , Nd ³⁺ , Sm ³⁺ , Dy ³⁺ , Yb ³⁺ , Gd ³⁺	Ca ²⁺ , Sr ²⁺	Co ³⁺ , Mn ³⁺ , Fe ³⁺ , Ni ³⁺	Mg ²⁺ , Fe ²⁺ , Co ³⁺ , Ni ²⁺ , Cr ²⁺ , Mn ²⁺

The majority of perovskite oxides used as cathodes in SOFC devices are based on LaMnO₃ or LaCO₃. Besides the electrical and catalytic performance, the major research interest in cathode materials are focused on thermal expansion mismatch and chemical reactivity with electrolyte. Thus, selections of cathode materials and dopants species are mainly determined by the electrolyte type and operation temperature ranges [38].

2.5.2.1 LaMnO₃ Based Cathode Materials

LaMnO₃-based materials are perovskite oxides with intrinsic p-type conductivity due to changes in the valence value of Mn. Doping LaMnO₃ with lower valence cations on A or B sites will enhance the electrical conductivity; such as Sr-doped LaMnO₃ (LSM):



For each La³⁺ substituted by Sr²⁺, a hole is formed on Mn³⁺ site to maintain electroneutrality. Compared with its electronic conductivity, LaMnO₃-based perovskites show very poor oxygen ionic conductivity and are general considered as pure electronic conductors [69].

The formation of insulating phases at the interface between cathode and electrolyte has been of great interest of numerous works [38,70]. The presence of an interfacial insulation phase is dependent on several factors like the electrolyte used, temperature and cathode composition [71]. As for doped-ceria electrolyte, there seems to be few reaction problems. This might be due to the fact that Ce⁴⁺ is too large to be incorporated into the SrBO₃ or LaBO₃ perovskite compounds [38]. LSGM has the same perovskite structure with most cathodes; the La cation diffusion problems mentioned earlier instead of detrimental reactions are the major concerns for LSGM. For YSZ electrolyte, pyrochlore phases (La₂Zr₂O₇) were observed during fabrication stage at temperature above 1200°C, below 1200°C, no significant reactions were detected. SrZrO₃ were reported to form with LaMnO₃ with containing high Sr dopant [72,73]. To avoid the system failure from the deleterious reactions, LaMnO₃ with lanthanum deficiency is proposed and proved to be effective [74-76].

Thermal expansion coefficient (TEC) of LSM-based cathodes is another concern. The TEC mismatch will introduce thermal stress during fabrication and operation, which might lead to

structural delamination or cracking. The TEC values of Sr-doped LSM cathodes are around 11.2~12.8 ($\times 10^{-6} \text{ K}^{-1}$), slightly higher than 8-YSZ ($10.5 \times 10^{-6} \text{ K}^{-1}$), in the temperature range of 25-1100°C [8]. This difference does not seem to be problematic considering that the actual cathode is porous and the operation temperature is not too high ($\leq 800^\circ\text{C}$). Moreover, a minimum TEC can be achieved with dopant concentration around 10-20%, reported by Mori et al. [77].

Further development of the manganite cathodes was carried out by replacing La^{3+} with other rare-earth cations (Nd, Sm, Pr, etc), changing the A-site dopant from Sr^{2+} to Ca^{2+} and/or B-site dopant with transition metal (Co). Improvements in chemical compatibility, thermal expansion properties and/or electrical conductivity were reported on Nd-, Pr-, Gd- and Sm- manganites (some doped with Ca/Co) [78-83]. LSM is more commonly employed as a cathode in the viewpoint of cost and availability for commercial application.

LSM was initially applied in the electrolyte-supported SOFC at high temperature (1000°C). Due to its stability with YSZ, LSM, in the mixture with YSZ as composite cathode, is still used for electrode-supported SOFCs working at intermediate temperature (700-800°C). The mixture improves the catalytic performance with additional triple phase boundaries (TPBs) beyond the interface between cathode and electrolyte. For lower temperature down to 700°C, new cathode materials based on LaCoO_3 have been developed.

2.5.2.2 LaCoO_3 Based Cathode Materials

LaCoO_3 possesses both high oxygen ionic conductivity and sufficient p-type electronic conductivity at elevated temperature. This makes LaCoO_3 a mixed-ionic electronic conductor (MIEC). Compared with YSZ- LaMnO_3 composite cathode, MIEC cathode materials extend

electrochemical active sites from one-dimensional TPBs to two-dimensional surfaces. By analogy to LaMnO_3 , the conductivity of LaCoO_3 can be improved by doping Sr on lanthanum site. Sr-doped LaCoO_3 (LSC) exhibits even higher electronic conductivity than LSM under the same condition. Although more attractive in conductivity, LaCoO_3 shows significant disadvantages on YSZ electrolyte compared with LaMnO_3 . First, the TEC values of LaCoO_3 was measured to be $23.8 \times 10^{-6} \text{ K}^{-1}$ over the range 25-1000°C [84]. Doping with Sr or Ca reduces TEC values to some extent, but still too high for YSZ. Second, LaCoO_3 reacts more readily with YSZ than LaMnO_3 at high temperatures. Indeed, the fabrication temperature of LaCoO_3 -based cathodes on YSZ was limited below 900°C to avoid formation of insulating phases like $\text{La}_2\text{Zr}_2\text{O}_7$ or SrZrO_3 [38]. Thus, LSC is more noted as the cathode material for ceria-based electrolyte due to its extraordinary catalytic activity at intermediate temperatures [71]. Even so, the TEC mismatch between LSC ($16\sim 22 \times 10^{-6} \text{ K}^{-1}$) and doped-ceria ($\sim 12 \times 10^{-6} \text{ K}^{-1}$) is still significant [38]. Further modification with Fe doping B-site on LSC identified the composition of $\text{La}_{0.6}\text{Sr}_{0.4}\text{Co}_{0.8}\text{Fe}_{0.2}\text{O}_3$ (LSCF) [85]. This material shows the same TEC value as GDC/SDC.

Other cobaltite perovskites ($\text{A}_{1-x}\text{A}'_x\text{BO}_3$, $\text{A}=\text{Pr, Gd, Sm, Dy, Nd, Ba}$; $\text{A}'=\text{Sr}$; $\text{B}=\text{Mn, Fe, Co, Ni, Ga, Mg}$) were investigated to exhibit high electrical conductivity comparable to LSC [71,86,87].

Due to the extreme complexity of perovskite compounds system, a great deal of research is still ongoing in hunting for the best composition as a cathode in terms of performance, stability, compatibility and cost.

In this study, LSCF-GDC and LSM-YSZ are used as cathode materials for YSZ-electrolyte SOFCs at lower temperature. LSCF-LSGM system was adopted as cathode for LSGM-electrolyte SOFCs.

2.5.3 Anode Materials

Anode materials are electrochemical oxidation catalyst of fuel and electronic conductor. During SOFCs operation, there are many physical and chemical processes going on in the anode, such as: charge transfer (electrons and ions), mass transport (delivery of fuel and removal of byproducts) and complex fuel reactions (e.g. hydrocarbon reforming and oxidation). Accordingly, the anode must meet the following requirements for satisfactory performance:

- High electronic conductivity
- Stability (chemical, phase, morphological and dimensional) in reducing environment
- Thermal expansion coefficients (TEC) matching with other cell components
- Chemical compatibility with adjacent components (electrolyte and interconnect)
- Large surface area and porosity to accelerate the reactions at electrode/electrolyte/gas TPB and diffusion of fuels and byproducts
- High catalytic activity to electrochemical oxidation of fuels
- High resistance to carbon coking and sulfur poisoning

To meet the above challenges, candidate anode materials are under intensive investigation. Until now, various materials systems have been attempted, which can be classified into two categories. One is ceramic and metal composite anode, also termed a cermet anode. The other is

known as ceramic anode, either entire ceramic or sometimes with a trace amount of metal as catalyst.

2.5.3.1 Cermet Anode

Conventional Ni-YSZ cermet anodes have been well studied and commonly used [8]. As a metal, Ni functions as an excellent catalyst for reforming and electrochemical oxidation reactions. It also provides electrical conductivity for anode. The ceramic phase in cermet anode is generally the same as the electrolyte materials. For traditional YSZ SOFCs, YSZ is added to the anode to alleviate the TEC mismatch between Ni anode ($13.3 \times 10^{-6} \text{ K}^{-1}$) and YSZ electrolyte ($10.5 \times 10^{-6} \text{ K}^{-1}$) [88]. In addition, YSZ constitutes a framework to maintain the porous structure of the anode by inhibiting the coarsening of nickel particles at high temperatures. More important, YSZ disperses Ni particles and extends the triple phase boundaries (TPBs) for the electrochemical reaction sites into the anode, so that the anode reactions occur more easily and the loss from the anode activation polarization becomes lower.

The electrical conductivity of a Ni-YSZ cermet is strongly dependent on the Ni content since YSZ is electronically insulating. A minimum Ni proportion in the cermet is necessary to form a continuous conducting pathway in the anode [89,90]. This limit is commonly known as the percolation threshold. For Ni-YSZ cermet, the threshold is ~30vol% Ni. To balance the thermal expansion match and sufficient conductivity, Ni concentration between 40-60 vol% was proposed in anode fabrication [88]. Other than the Ni content, the conductivity is also influenced by the dispersion/continuity of Ni phase, which is associated with the YSZ framework morphology, such as porosity, pore size, size distribution [91,92].

The optimization of Ni-YSZ microstructure and composition has attracted wide attention to minimize the anode polarization [93-96]. It has been found that the 40-45vol% Ni will minimize the anode polarization, presumably corresponding to the enlargement of TPBs [97,98]. Also, the comparison studies of anodes by Lee et al. [99] revealed that particle packing, porosity, connectivity of pores and conductive phases have a dramatic influence on the cell performance. In order to achieve low anode polarization, optimization of the processing parameters is essential to prepare an anode with high electronic conductivity, stable microstructure, and sufficient porosity.

Stability is a necessity for long-term operation of SOFC anode at high temperatures. Sintering of Ni particle has long been a major concern for Ni-YSZ cermet, because Ni has low melting temperature and is liable to aggregate and coarsen at high operation temperatures. Performance degradation was observed for prolonged period of operation, which is associated with the loss of active surface area and a drop in electrical conductivity from the grain growth of Ni [100]. It has been well established that the major mechanism of anode performance degradation is either Ni coarsening or agglomeration [88]. To address this challenge, additives besides YSZ such as TiO_2 , Cr_2O_3 , MgO and Mn_3O_4 , have been introduced to the anode to enhance the interfacial wettability between Ni and YSZ, which leads to extended durability [101].

A conventional Ni-YSZ cermet anode has been well developed for hydrogen SOFCs with high performance (peak power density 1.8~1.9 W/cm^2 [102,103] at 800°C). This is due to the fact that Ni is an excellent catalyst for electrochemical oxidation of hydrogen. As mentioned in section 2.2.2 and 2.2.3, Ni also shows highly catalytic activity for hydrocarbon reforming. This catalytic property is exploited in internal reforming that enable SOFCs to operate directly on hydrocarbon.

Unfortunately, the carbon formation in the presence of Ni is unavoidable due to the catalysis of nickel to crack hydrocarbons, resulting in possible carbon deposition and cell failure. Actually, poor carbon resistance is the major drawback for Ni-YSZ anode under hydrocarbon operation. In order to alleviate this concern, one approach is to augment the catalytic activity of the Ni-YSZ anode by the addition of Mo or Au [104]. The addition of Mo could increase methane conversion and reduce the carbon deposition. Au in the anode could inhibit the formation of carbon and improve the methane conversion. Another way is to employ metals (e.g. Co, Pt, Pd, Rh and Ru) instead of Ni as substitute anode catalysts [42-44,105-107]. Co has similar catalytic activity as Ni and high sulfur tolerance. Ru and Rh offer the advantages of lower sintering tendency, higher carbon coking resistance and even higher reforming activity. Pt and Pd are active metals for water gas shift, steam reforming and dry reforming of methane. [108,109]. However, all these metals are not feasible for commercialization because of their exorbitant prices.

It is desirable to find an alternative cermet with lower susceptibility to hydrocarbon cracking as well as low cost for mass production. Cu-CeO₂-based cermet was proposed by a research group at the University of Pennsylvania [31]. As an inert catalyst to carbon formation, Cu instead of Ni is employed as a mere current conductor in the anode. Undoped-ceria is a well-known oxidation catalyst and possesses electrocatalytic activity to oxidize hydrocarbons [28,88,110]. This makes CeO₂ attractive as an anode component for direct-hydrocarbon SOFCs. However, mechanical degradation of CeO₂ in reducing atmosphere requires extra caution. It has been found that 40~50 mol% dopants (e.g. Gd, Sm, Y) concentration is promising for dimensional stability and carbon deposition suppression [88]. Compared with CeO₂, doped-ceria has a lower activity for methane oxidation, which further increases the activation polarization of Cu-CeO₂ anode. Although the

Cu-CeO₂ cermet has a better carbon-coking resistance and higher sulfur tolerance than the Ni-YSZ counterpart, its poor catalytic activity leads to poor performance and remains an obstacle to application [110].

Despite the inherent drawbacks, Ni-YSZ cermet is still the most preferred anode material for SOFC due to its acceptable performance and low cost. Ni-YSZ and Ni-doped-CeO₂ cermets are selected as the anode materials for this study.

2.5.3.1 Ceramic Anode

A ceramic anode as an alternative aimed at overcoming the limitation of Ni-based anode has attracted intensive development efforts recently. Compared to Ni-based cermet anodes, ceramic anodes do not get sintered as the anode after long operation of SOFCs, resulting an improvement in the stability of the cell performance. Also, they show much better capability of withstanding sulfur contamination and carbon deposition. Moreover, ceramics exhibit better dimensional stability while undergoing repeated reduction-oxidation (redox) cycling than Ni. However, the study of ceramic anodes is still in its preliminary stage to find materials with properties suitable for one or more of the anode requirements [110]. According to the materials structures, several groups of materials have been investigated for their potential as anode candidates, such as: fluorite oxides[111-113], perovskite oxides[114-120], tetragonal tungsten bronze structure oxides [121,122] and rutile oxides[123].

Fluorite oxides: CeO₂ and ZrO₂ based materials are of fluorite oxides and have been doped to yield high conductivity for anode applications. Sm or Gd doped CeO₂ [111,112] (GDC or SDC) and undoped CeO₂ are renowned for their mixed ionic and electronic conductivity (MIEC) in reducing atmospheres, but the mechanical degradation under reducing conditions poses a great

concern for their application [88]. ZrO_2 doped with Y_2O_3 , Sc_2O_3 and TiO_2 to form solid solution of $Zr(Ti, Y, Sc)O_{2-x}$ has shown promising MIEC properties to be applied as anodes [113].

Perovskite oxides: Perovskite materials have been widely investigated as potential SOFC anode materials [124]. Co and Ni based perovskites are not suitable for anode application due to their chemical instability in reducing atmosphere [88,110]. The current emphasis is on Cr-, Ti-, Nb-, Fe- and Mn-based perovskites. Table 2.6 lists perovskite oxides (with dopants) proposed or applied as potential anode materials.

Table 2.6 List of the perovskite oxides for cathode application [114-118,120]

Site	A site	A site dopant	B site	B site dopant
Cations	La^{3+} , Ba^{2+} , Sr^{2+} , Ca^{2+} ,	La^{3+} , Sr^{2+}	Cr^{3+} , Ti^{4+} , Nb^{4+} , Fe^{3+} , Mn^{4+}	V^{5+} , Ru^{3+} , Ti^{4+} , Mg^{2+} , Ni^{2+} , Mo^{5+}

Among the reported perovskite systems, chromites and titanates are the most promising candidates [118,125]. Until now, each material can only match some of the stringent requirements for SOFC anodes. Double perovskite [119] or complex perovskite [114] materials have been proposed and shown to exhibit good electrochemical activity, redox stability and electrical conductivity. The idea is to meet the anode property requirements by the combination of complimentary functionality from appropriate cations [124].

Tetragonal tungsten bronze structure oxides: Tungsten bronze structure was first studied by Magneli [126] in the phase K_xWO_3 . This structure is similar to perovskites and can be written as $A_{0.6}BO_{3-\delta}$. Tao et al. [121,122] tested materials with composition of $A_{0.6}B_{1-x}B'_xO_{3-\delta}$ (A=Ba, Sr, Ca, La; B= Nb; B'= Mg, Ni, Mn, Cr, Fe, In, Sn). Among these oxides, $Sr_{0.2}Ba_{0.4}Ti_{0.2}Nb_{0.8}O_3$

offers the highest electronic conductivity in reducing atmosphere (10S/m , $P_{\text{O}_2}=10^{-20}\text{atm}$, 930°C). However, the conductivity in air is rather low and polarization is still higher than mixed conducting oxide such as TiO_2 -doped YSZ [127].

Rutile oxides: NbO_2 or Nb_2TiO_6 have rutile structures and very high electronic conductivity in fuel conditions [123]. Unfortunately, their TECs are too low ($2.3\times 10^{-6}\text{K}^{-1}$, $25\sim 600^\circ\text{C}$) to be compatible with electrolyte materials ($10\sim 12\times 10^{-6}\text{K}^{-1}$). Nb_2TiO_6 possesses very low ionic conductivity, which further makes it unsuitable as an anode.

Most of the work in ceramic anodes materials has focused on electronic and ionic conductivities rather than their catalytic properties. Although stable operation on hydrocarbons, mainly methane, has been achieved in SOFCs with many of these ceramics as anodes, it is likely that their catalytic properties are not optimal. Instead, people add small amounts of Ni into the anode materials [29,128] or introduce Ru or V via surface exsolution from perovskites to improve catalytic activity and lower the activation polarization [129]. The use of composite ceramic anodes has been proposed as one approach for optimizing both the conductive (ionic/electronic) and catalytic properties of anode [110].

2.6 Summary

Since the very first fuel cell was demonstrated nearly two centuries ago, fuel cell research has made tremendous progress in the past twenty years. Different types of fuel cells have been built and some have been applied in different aspects of life. SOFC is most favored as the next generation fuel cell due to its fuel flexibility and high operation temperature. Hydrocarbon rather than hydrogen is more competitive and realistic for commercialization of SOFCs. However,

carbon deposition from hydrocarbons imposes great challenges on SOFC operation. Different fuel processing technologies have been developed and employed to avoid the direct contact of hydrocarbon with SOFC stacks. Direct hydrocarbon operation is more attractive due to the simplified system design and improved system efficiency. Materials are playing the key role in the realization of the direct hydrocarbon operation without carbon coking.

Among all hydrocarbons, methane is abundant as major component in natural gas and poses less challenge in direct operation. In this study, various strategies have been adopted to achieve direct methane operation of SOFCs without coking. The related applications of direct methane SOFCs was discussed, such as electrochemical partial oxidation (EPOx) reactor for (co-)generation of synthesis gas (and electricity).

CHAPTER THREE

Direct Operation of Solid Oxide Fuel Cells with Methane Fuel

Chapter 3: Direct Operation of Solid Oxide Fuel Cells with Methane Fuel

3.1 Introduction

There has been considerable recent interest in the operation of solid oxide fuel cells (SOFCs) directly on hydrocarbon or alcohol fuels [65]. This is distinct from internal reforming [130] because the hydrocarbon fuel is introduced without a substantial amount of H₂O, CO₂, or O₂. Advantages of direct-hydrocarbon operation compared to steam reforming include simplification of the balance of plant, e.g. elimination of exhaust-gas recirculation, and a higher open-circuit voltage. The advantage compared to partial-oxidation reforming is a potentially higher efficiency and no nitrogen dilution of the fuel. Finally, an efficient direct-hydrocarbon SOFC could be used for electrochemical partial oxidation of hydrocarbons, co-producing un-diluted syngas/hydrogen and electricity [131]. The main drawback is that the cells are susceptible to coking of the Ni-based anodes during hydrocarbon operation. There are three strategies now adopted for developing SOFCs that can operate directly on hydrocarbons [124]. The first strategy replaces Ni with Cu in anode cermet [31,132]. Cu is an inert catalyst to carbon-forming reactions on Ni. Stable operation has been achieved with higher hydrocarbons like toluene, butane and butane [31]. The second strategy is to develop new anodes from electronically conductive ceramics. As stated in section 2.5.3.1, various oxides have been attempted to substitute Ni-based anodes. The third one is different from the previous two, in which no changes are made to the conventional Ni-cermet anode but the operating conditions of the fuel cells are modified to avoid coking or remove the deposited carbon species. While there has been considerable progress in the development of SOFCs with non-Ni-based anodes [65], the poor performance, especially the

low power densities and high anode polarizations, has prevented the application of such SOFCs in practical applications. It is desirable if the established SOFC technology can be utilized. In particular, Ni-YSZ anode supported SOFC are being heavily developed and can achieve very high power densities.

Direct-methane SOFCs have been the focus of considerable attention, both because natural gas is a widely available fuel and it poses lesser challenges than heavier hydrocarbons. It has been shown that SOFCs with Ni-based anodes can be operated stably with methane at temperatures $<700^{\circ}\text{C}$, or at higher temperatures if a substantial cell current density is maintained [2,4,5,29,133]. In a recent report, direct-methane operation of anode-supported SOFCs resulted in power densities of 0.85 W/cm^2 at 800°C [2]. The coke-free stable operation has been explained by the relatively low rate of methane cracking at temperatures $<700^{\circ}\text{C}$, and by the effects of cell reaction products at higher temperature and current density [2,65]. However, a number of questions remain about direct-methane SOFC operation, including the nature of the hydrocarbon reactions and the rate-limiting electrochemical steps at the anode, why coking does not occur, the exact operating parameters in which stable coke-free operation can be maintained, and what are the main failure mechanisms when coking does occur.

In this chapter, we attempt to answer these questions with a more complete study of the direct-methane operation of Ni-YSZ anode-supported SOFCs, including cell tests, open circuit voltage analysis, electrochemical impedance spectroscopy, mass spectrometric studies of anode exhaust gas, lifetime studies designed to determine useful direct-methane operating conditions, and an examination of coking failure mechanisms. The results have been interpreted considering thermodynamic analysis and mass transport arguments.

SOFC tests were carried out in a single cell test setup similar to that used by many groups [135]. Figure 3.1 shows a schematic view of the setup. Silver ink was used for sealing the cell to the alumina tube. It provides a simple, convenient seal that has been shown to allow cell testing for > 100h. The tests were done from 600 to 800°C with the cathode exposed to ambient air and the anode to humidified (3% H_2O) hydrogen or methane. The flow rate was 30sccm for both fuels, corresponding to maximum fuel utilizations of 37% for H_2 (3.360A/cm²) and 12% for CH_4 (4.232A/cm²). The anodes were reduced in humidified hydrogen at 700°C for several hours prior to cell testing. The current-voltage curves and electrochemical impedance spectra (EIS) were obtained using an Electrochemical Workstation (IM6, ZAHNER). The frequency range for the impedance measurement was 0.1Hz to 100kHz. While the asymmetry of anode-supported SOFCs leaves some issues regarding the exact interpretation of the EIS data [136], many authors have reported EIS data using a relatively simple EIS interpretation [33]. Anode exhaust gas was sampled during cell operation using a differentially-pumped mass spectrometer.

A commercial software package (THALE, ZAHNER) was used to simulate and fit the EIS data using equivalent circuits. A computer code, which minimized the total Gibbs free energy of the anode gas with constraints using Taylor's expansion and Lagrange's method of undetermined multipliers, was used to calculate equilibrium fuel gas compositions and resulting open circuit voltages. A similar calculation based on diluted dry methane feed gave similar results [137].

3.3 Experimental Results

3.3.1 Current-Voltage Measurements

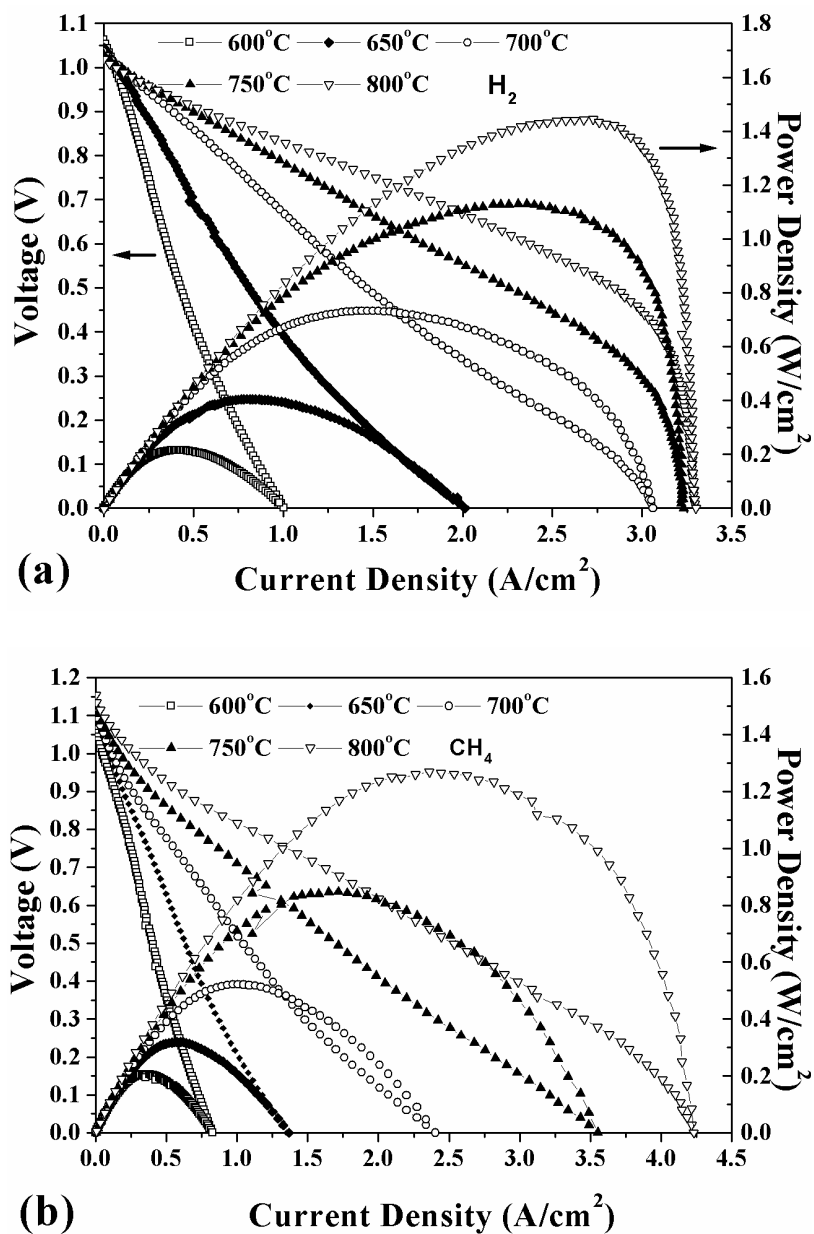


Figure 3.2 Voltage and power density vs. current density of a SOFC operated on humidified hydrogen (a) and methane (b).

Figure 3.2 shows typical voltage V and power density P vs. current density J of a SOFC operated on humidified hydrogen (a) and methane (b). The maximum power densities at 800°C were 1.44 W/cm² for hydrogen and 1.27W/cm² for methane. The power density with methane is substantially higher than in prior reports [2,4], due to the better overall performance of the SOFC. Note that operation in methane was not stable at high temperature T and low J ; thus, for $T \geq 700^\circ\text{C}$, large J was maintained for most of the time with a short interruption ($\approx 5\text{s}$) of the current flow during each J - V measurement. The stability region of SOFC operation is discussed in detail in section 3.2.2 below. The J - V curves were non-linear, showing apparent activation polarization at low J and concentration polarization at high J . At low J , the resistance was higher for methane than for hydrogen, suggesting that the electrochemical oxidation step was slower for methane, in agreement with prior reports [2]. The high- J limiting current, seen for both fuels at 800°C, was actually larger for methane suggesting lower concentration polarization. The former effect was explored in more detail using electrochemical impedance spectroscopy (see section 3.3.3 below).

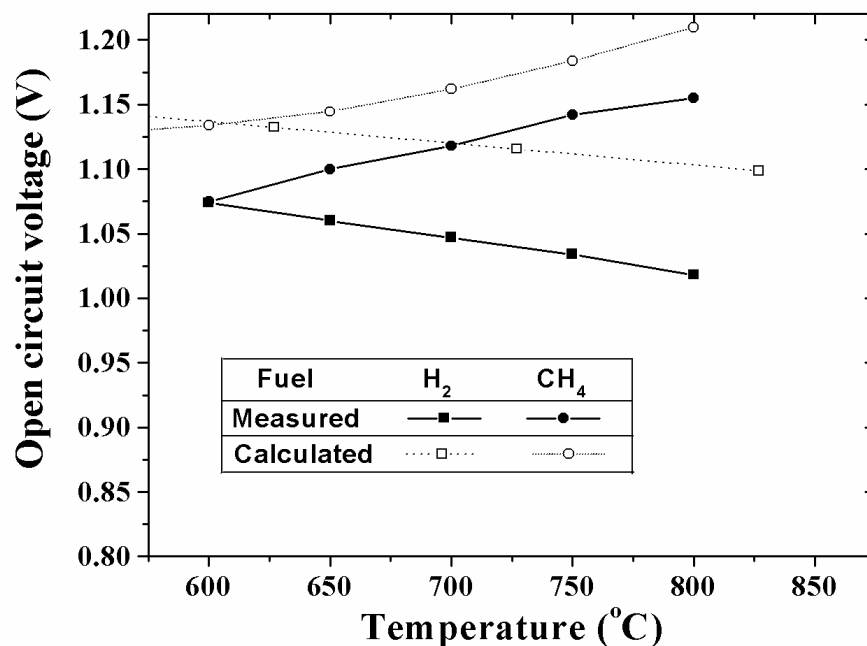


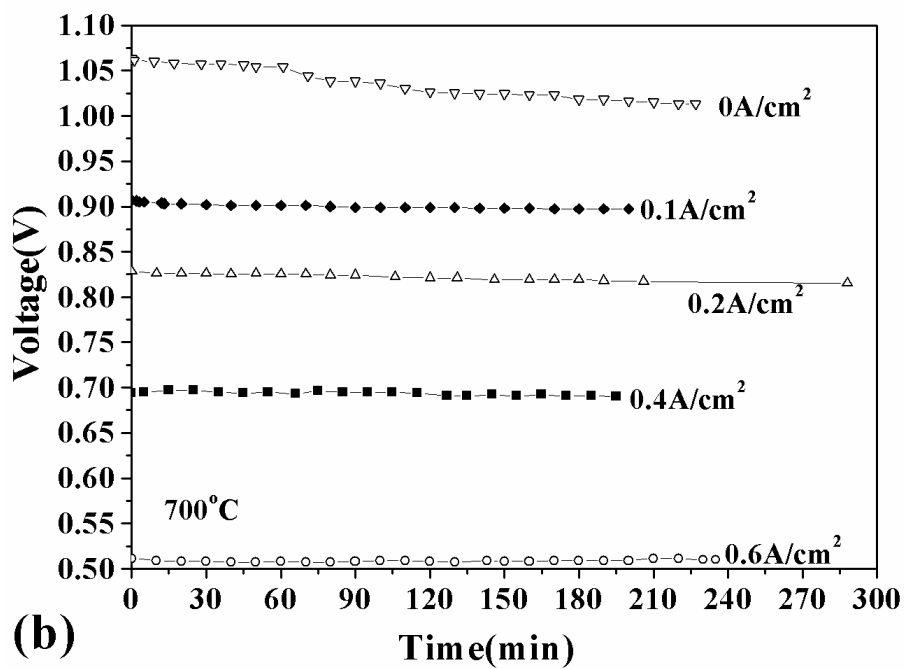
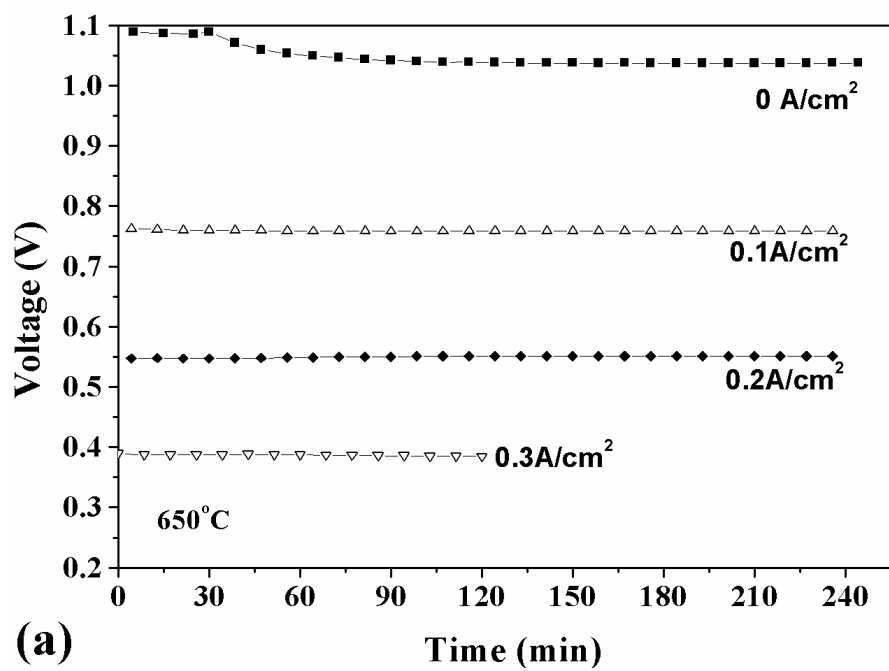
Figure 3.3 Open circuit voltage values versus T for both hydrogen and methane. Also shown are the values predicted by assuming that the humidified methane reaches an equilibrium composition.

Measured open circuit voltage (OCV) values are plotted versus T for both hydrogen and methane in Figure 3.3. The OCV in methane increased with increasing T , opposite of the trend shown for hydrogen. The high OCV values at high T are in agreement with prior results [2,138]. Also shown in Figure 3.3 are predicted OCV values, assuming that the humidified methane reaches equilibrium. The experimental and predicted OCV values are in good agreement, although the experimental values are $\approx 40\text{mV}$ lower. Experimental OCV values are typically slightly less than theoretical, presumably indicating slight gas leaks in the single cell test. The agreement between the measured and predicted OCV suggests that the humidified methane fuel reached equilibrium at the anode under the cell test conditions.

3.3.2 Cell Stability Tests

A key observation in the above measurements was the instability under some conditions, particularly high T and low J . The following protocol was used to quantitatively determine the stability region. First, the cell was operated in hydrogen for more than 24h to reduce the anode and fully stabilize the cell performance. Second, the fuel was switched to methane with the cell maintained near the maximum power point. After the switch to methane, the V value at constant J dropped by $\approx 20\%$ to a new steady state value. The drop was expected based on the I - V curves in Figure 3.2. The transition occurred over 30-45 min, corresponding to the time required to purge the gas-flow lines and bubbler of remnant hydrogen. Third, J was maintained constant near the maximum power point for >3 h, long enough to observe whether V was stable. Fourth, J was reduced and maintained constant for >3 h. This latter step was repeated until V became unstable.

Figure 3.4 shows results taken in this way at 650, 700, 750, and 800°C. As shown in Figures 3.4a (650°C) and 3.4b (700°C), stability in methane was excellent as long as a minimum cell current density $J \sim 0.1 \text{ A/cm}^2$ was maintained. It was only at $J = 0$ that V decreased gradually over several hours. Thus, the critical current density J_c was $0 < J_c < 0.1 \text{ A/cm}^2$ at these temperatures. The results were similar at 750 (Fig. 3.4c) and 800°C (Fig. 3.4d), but much larger critical current values, *i.e.* $0.8 \text{ A/cm}^2 < J_c^{750} < 1.2 \text{ A/cm}^2$ and $1.4 < J_c^{800} < 1.8 \text{ A/cm}^2$, were needed to maintain stable operation. These results imply that the SOFC oxygen ion current was at least partially responsible for preventing coking and thereby maintaining stable operation. We believe that J_c increased with increasing T because of the increasing rate of methane cracking above $\approx 700^\circ\text{C}$ [139].



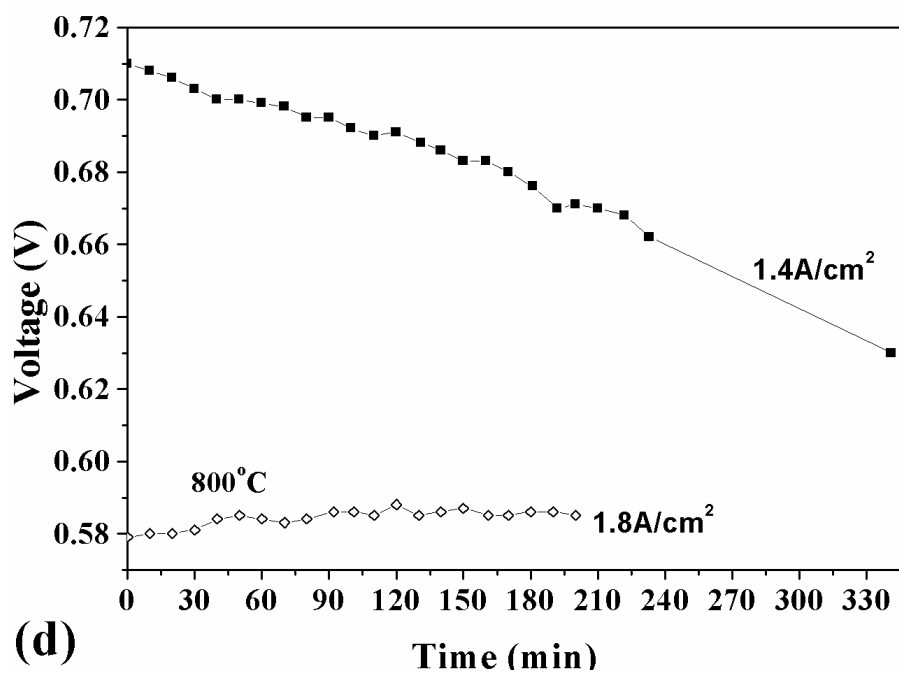
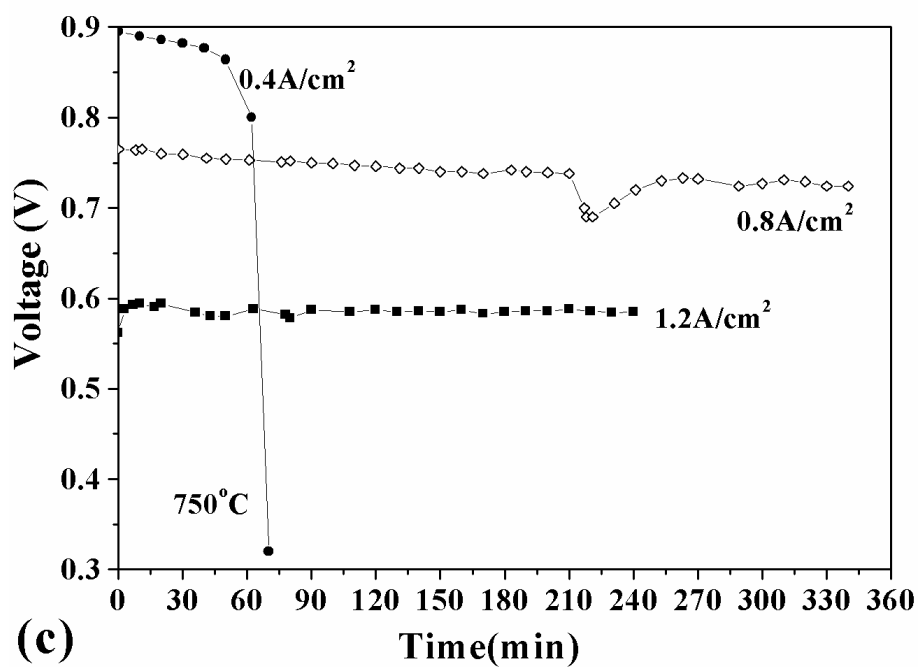


Figure 3.4 Cell voltage versus time at constant current J for SOFCs operated in humidified methane at 650 (a), 700 (b), 750 (c), and 800°C (d). The cells were operated at different J values for 3-6 h in each step, starting at high J and reducing J in steps.

A few tests were carried out for longer times to help assure that instability did not develop beyond the 3-4h time frames shown in Figure 3.4. As shown in Figure 3.5, a cell operated in methane at 700°C, $V = 0.6V$, and $J = 0.8A/cm^2$ was stable during a 168 h test.

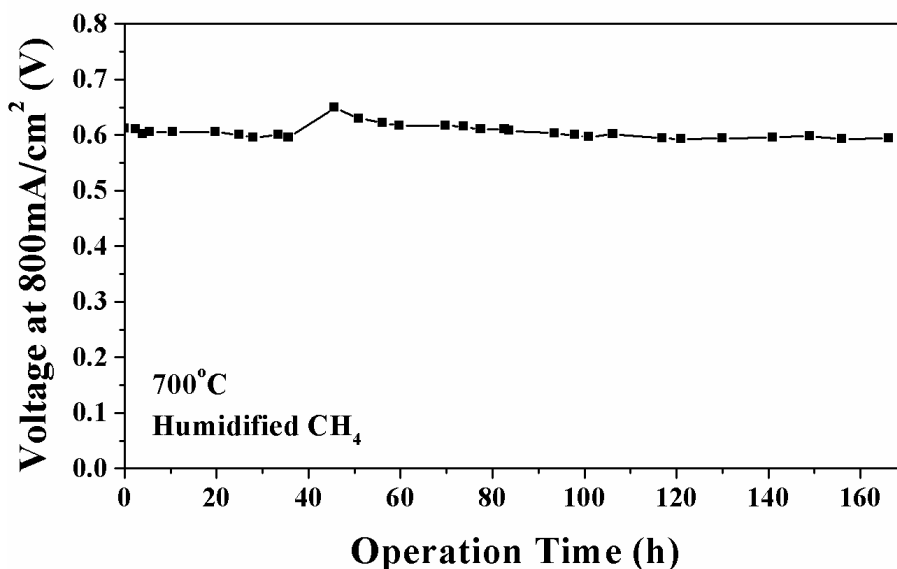


Figure 3.5 Results of an extended SOFC test at 800mA/cm² in humidified methane at 700°C.

Visual observation and SEM measurements after cell tests showed no evidence of coke on the anodes in cases where cell performance was stable. Figure 3.6 shows SEM images and EDX spectra of anodes after stable operation near maximum power in humidified hydrogen (a) and methane (b) at 750°C. The SEM images show very similar porous microstructures as expected for Ni-YSZ. The EDX spectra are also very similar, showing the expected Ni, Zr, and Y peaks. Very weak O and C peaks are also present. There is little difference between the C peaks for hydrogen and methane operation, suggesting that the C may have been from contamination in the SEM chamber. These results show no measurable coking effect of operation in methane at relatively high J .

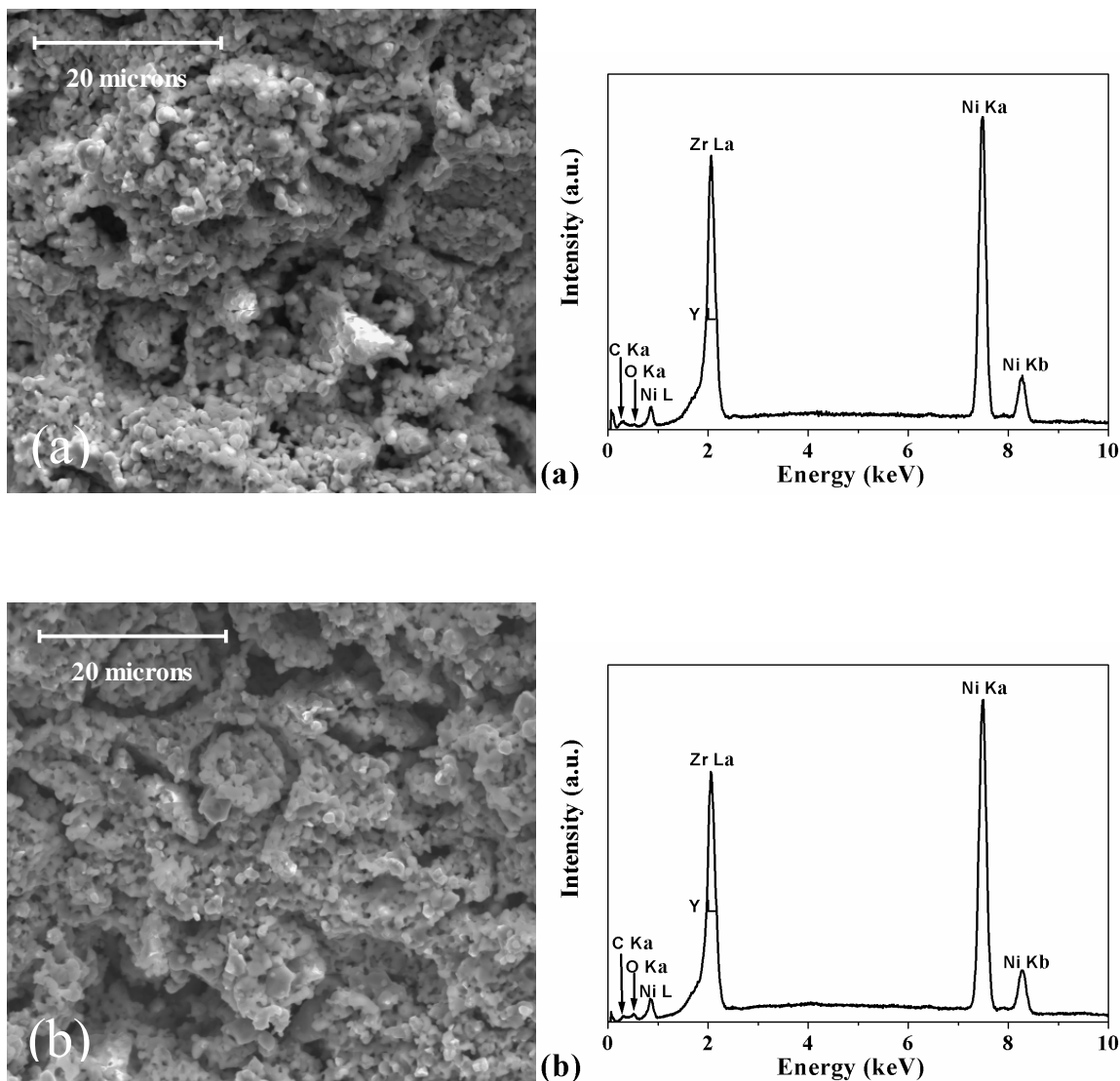


Figure 3.6 Fracture cross-sectional SEM micrographs and EDX spectra taken from anodes after stable SOFC operation in (a) humidified hydrogen and (b) humidified methane at 750°C, and $J = 1.2\text{A}/\text{cm}^2$ (near maximum power). Image contrast and EXD spectra did not vary with position in the anode.

Figure 3.7 shows cross-sectional images and EDX spectra taken from two different regions of an anode of a cell that was operated at 700°C and $J \approx 1\text{mA}/\text{cm}^2$; during the test the voltage degraded gradually for several hours and then the anode cracked. Figure 3.7(a), taken from a region near the anode free surface, shows clear evidence of carbon: the EDX spectrum shows a

strong carbon peak and the image shows white contrast that is not present in the SEM image for hydrogen (Figure 3.6(a)). These results suggest that coke builds up within the anode; this may cause performance degradation shown in Figure 3.4 by one or more mechanisms. For example, carbon may block anode pores, degrading cell performance. Alternatively, the coke buildup may lead to volume expansion and consequent micro-cracking, presumably leading to an interruption of anode current collection pathways. While Figure 3.7(a) does not show any evidence of micro-cracking, cell failure by cracking was often observed after long-term cell operation under coking conditions. Regardless of the exact mechanism, these results clearly link the degradation to coking. In general, the SEM-EDX results showed that the carbon EDX peak height and the white SEM contrast decreased from the free surface (Figure 3.7a) towards the electrolyte. The anode microstructure and C peak height measured near the electrolyte, as shown in Figure 3.7(b), appeared identical to that of a SOFC operated in hydrogen (Figure 3.6a). The suppression of coking may result from a high concentration of cell reaction products at the anode/electrolyte interface, as discussed in more detail in section 3.3.

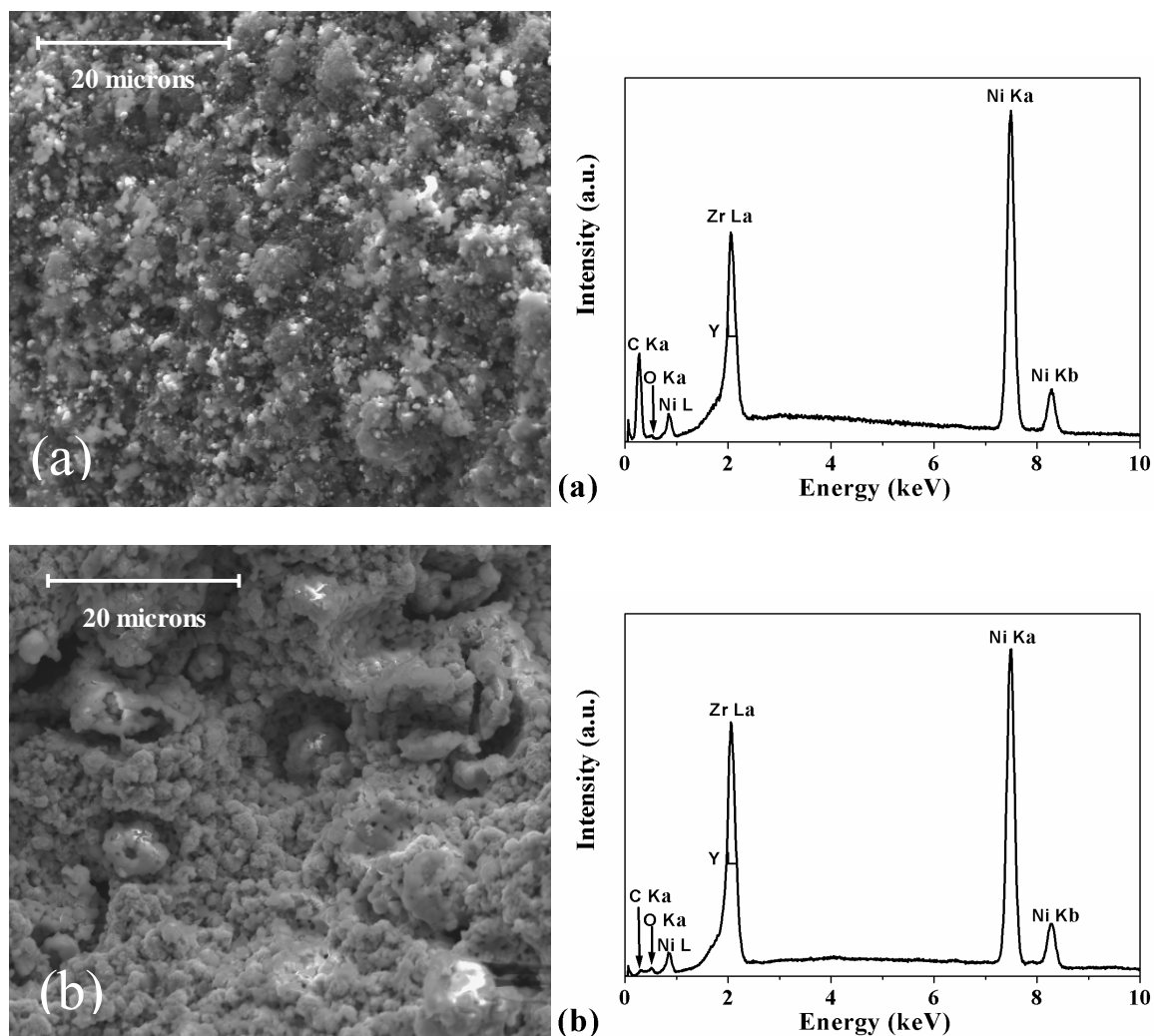


Figure 3.7 Cross-sectional SEM micrographs and EDX spectra from an anode after cell operation under conditions leading to performance degradation. Part (a) shows a region near the anode free surface, and part (b) shows a region near the electrolyte.

3.3.3 Electrochemical Impedance Spectroscopy (EIS)

EIS measurements were done at relatively low temperatures and with non-zero current densities, as cell degradation at high T and low J , discussed in the above section, led to artifacts in the EIS data. Figure 3.8 shows a comparison of typical EIS results, from cells operated with hydrogen and methane, for $J = 400\text{mA}/\text{cm}^2$ and temperatures of 600 (3.8a) and 700°C (3.8b).

The first real-axis intercepts, at $0.26\Omega\text{cm}^2$ (600°C) and $0.10\Omega\text{cm}^2$ (700°C), agreed well with the expected ohmic resistance of the 10-20 μm thick YSZ electrolyte.

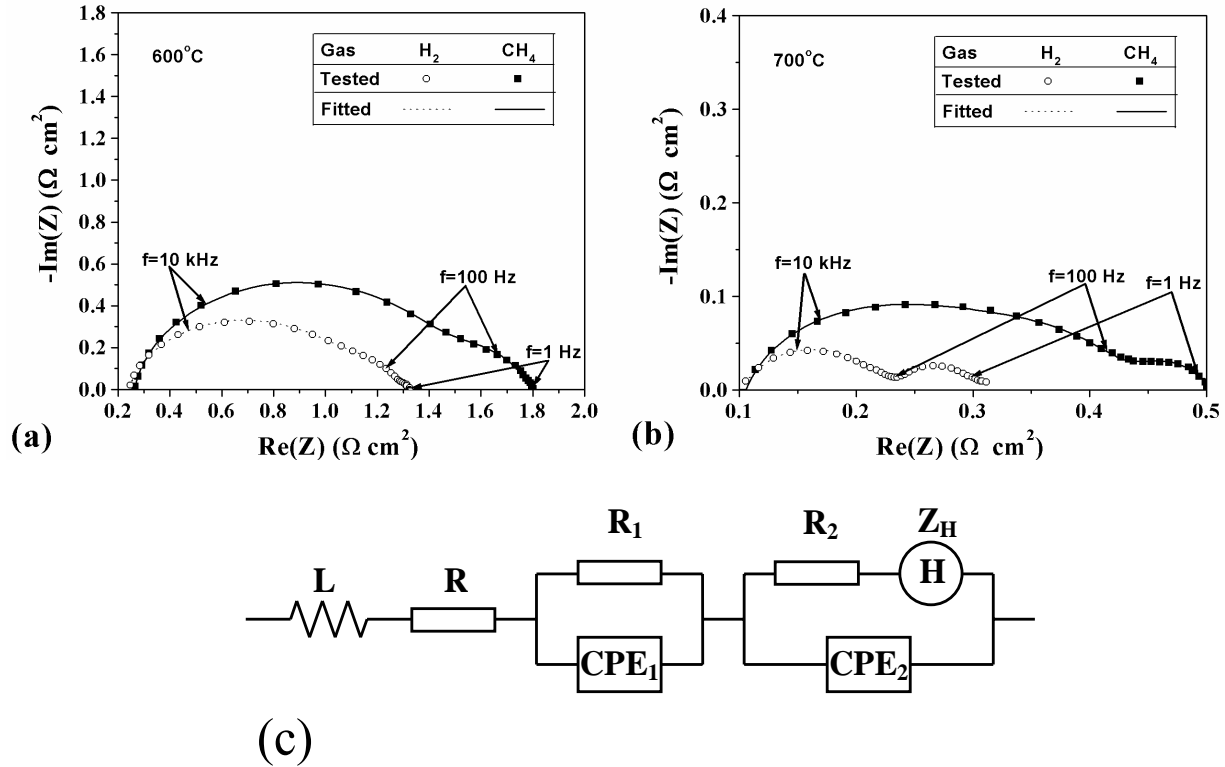


Figure 3.8 Electrochemical impedance spectra measured at $J = 400\text{mA}/\text{cm}^2$ and 600°C (a) and 700°C (b), for hydrogen and methane. The fitted curves were obtained using the circuit model shown in (c) with the parameters shown in Table 3.1.

Figure 3.8 also shows fits to the arcs obtained using the equivalent circuit model shown in the figure. The lower-frequency arc was fit with a Gerischer-type response given by

$$Z_H = R_{\text{chem}} \sqrt{\frac{1}{1 + j\omega t_{\text{chem}}}} \quad (3.1)$$

where t_{chem} is the relaxation time and R_{chem} the characteristic resistance describing the chemical contributions to the cathode impedance. R_{chem} corresponded to the “H” element in Figure 3.8(c).

This circuit element is predicted by the ALS model [140], where the rate-determining steps are

surface exchange and solid-state diffusion. It should be applicable to the present mixed-conducting LSCF-based cathodes. The higher-frequency arc was fit by a simple resistance with a constant phase element (CPE). The fits (Figure 3.8) obtained with this equivalent circuit model were in good agreement with the experimental EIS data, and the resistance values obtained are listed in Table 1. The pure resistance R varied only with temperature, as expected for an electrolyte resistance. Note that the R values from the fits (Table 1) are more accurate than the real-axis intercept values in Figure 8, because the latter are affected by wire inductances. R_{chem} , R_1 , and R_2 all changed with fuel, suggesting an effect of fuel composition on both the low and high frequency arcs. This is probably an artifact due to the asymmetric geometry of these anode-supported cells, which complicates the interpretation of the impedance results [136].

Table 3.1 Resistance values obtained for fits to the impedance spectra in Figure 3.8.

Temperature	Gas	R	R_1	R_2	R_{chem}
600 °C	H ₂	0.209	0.900	0.180	0.037
	CH ₄	0.242	1.24	0.275	0.036
700 °C	H ₂	0.074	0.149	0.050	0.037
	CH ₄	0.079	0.250	0.096	0.065

(Units: Ωcm^2)

3.3.4 Mass Spectrometer Measurements

Mass-spectrometer measurements of the anode exhaust gas were carried out to determine the nature of the anode reaction products. Figures 3.9a and 3.9b show the real-time changes in the exhaust CO₂ (mass 44) and H₂O (mass 18) signals, respectively, as J was varied in steps during SOFC operation in humidified methane at 800°C. The lag times for the measured partial pressures to stabilize were related to the time required for the anode gases to reach the mass spectrometer through the sampling tube and differential pumping system. The lag time for H₂O was longer, presumably due to the tendency of H₂O to adsorb on surfaces. For the H₂O data, steady state concentrations were estimated by extrapolating the data to longer times.

Figure 3.10 summarizes the product gas concentration results derived from the mass spectrometer data. Each of the species H₂, CO, CO₂, and H₂O increased with increasing J , but the increases in H₂ and CO were substantially larger. Note that an artifact in the mass spectrometer data, the so-called “zero blast” effect [141], caused the mass spectrometer to under-estimate the size of low-mass peaks such as hydrogen. Thus, we believe that the hydrogen concentration should actually be larger than CO in Figure 3.10.

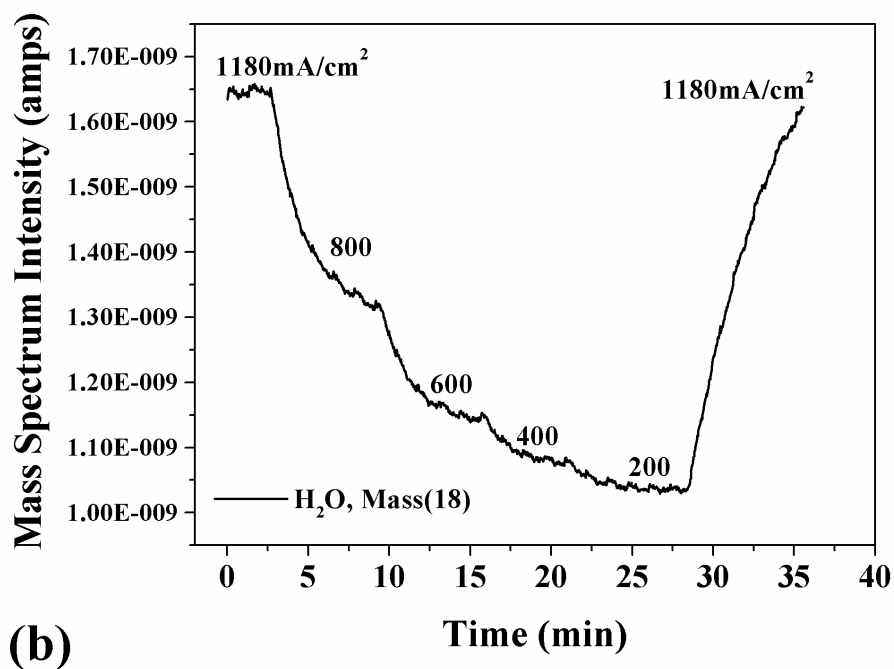
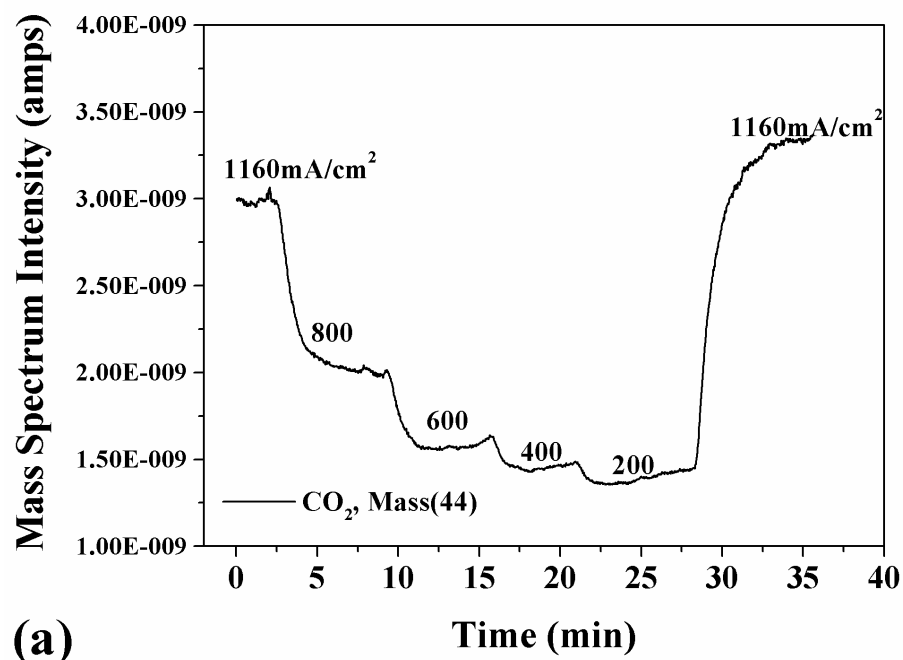


Figure 3.9 Real-time changes in the exhaust gas composition for different cell current densities J during SOFC operation in humidified methane at 800°C , observed via the mass 44 (CO_2) signal (a) and mass 18 (H_2O) signal (b).

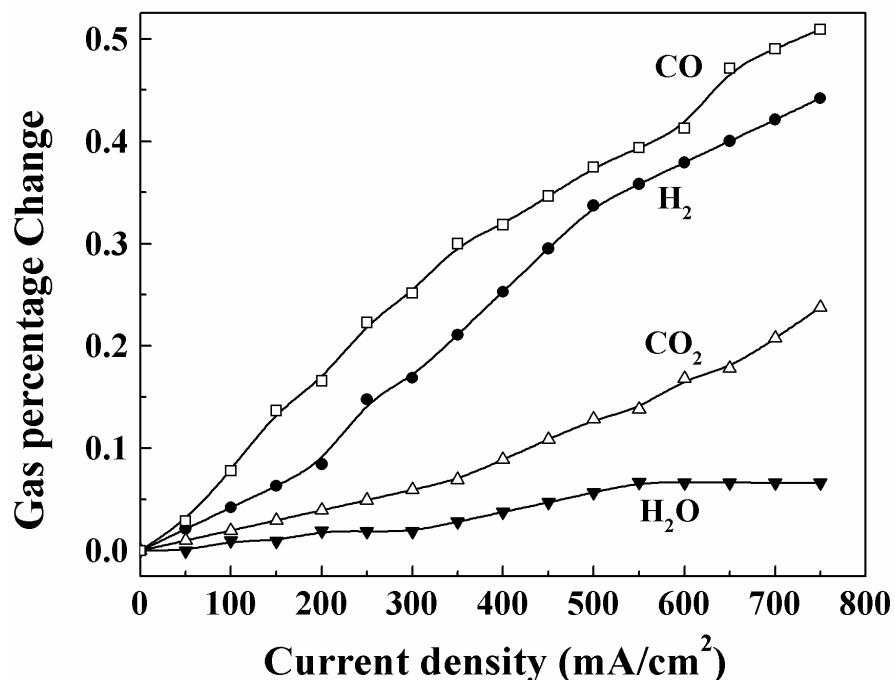


Figure 3.10 Changes in the concentrations of various species versus SOFC current density during operation in humidified methane at 800°C, derived from the mass spectrometer data.

3.4 Discussion

The above results have shown that Ni-YSZ anode-supported SOFCs can provide high power densities when operating directly with methane. The cells were stable without coking at high current density and low temperature, whereas substantial coking occurred at low current density and high temperature. CO and H₂ were the primary gaseous reaction products.

In order to help understand these results, we present results of a thermodynamic calculation of the equilibrium reaction products for an input fuel composed of humidified (~3% H₂O) CH₄, and including the addition of oxygen via fuel cell operation. Figure 3.11 shows the results obtained for 700 and 800°C.

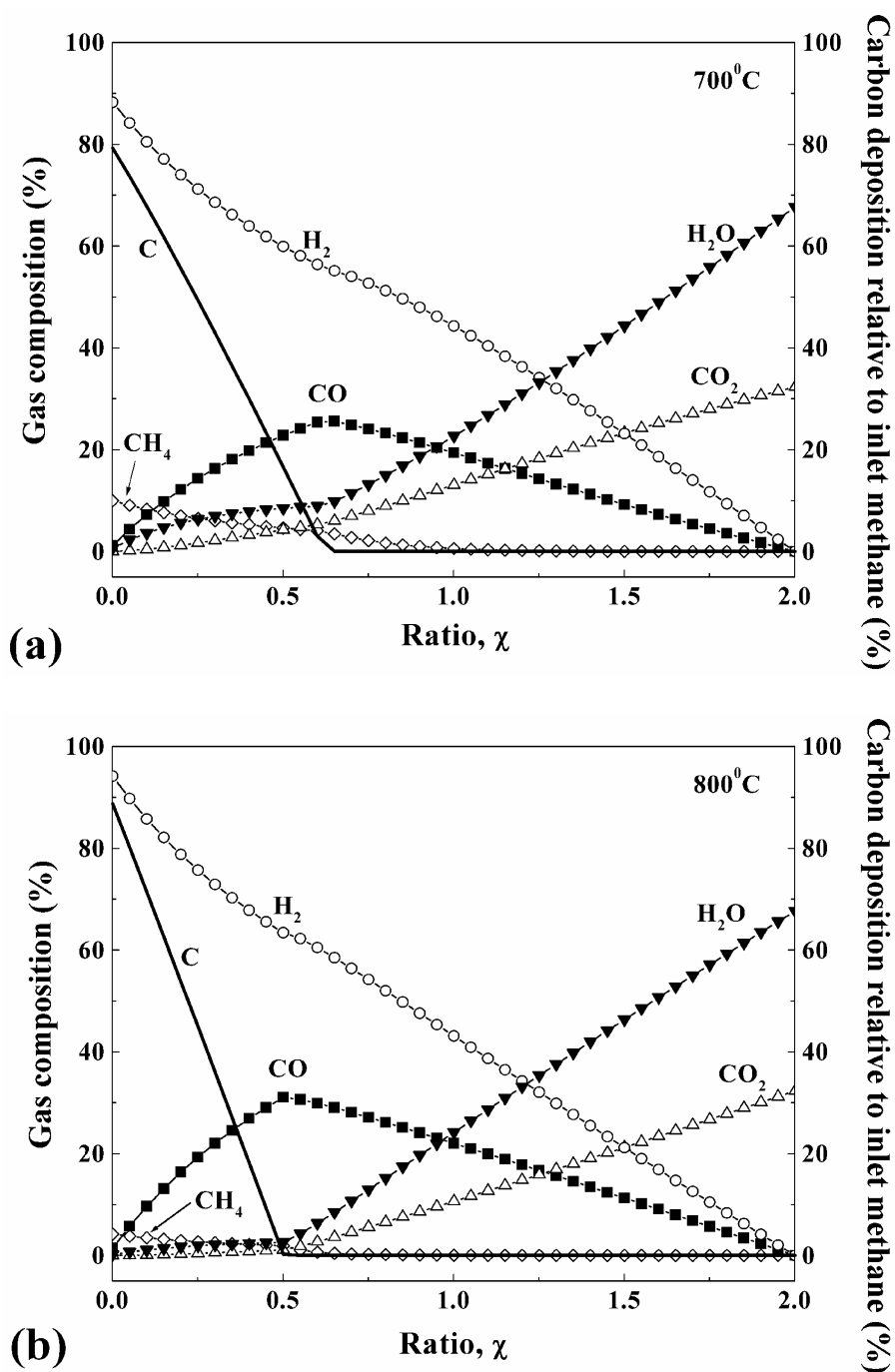


Figure 3.11 Thermodynamic prediction of the equilibrium anode gas composition and fraction of CH₄ cracking to form C, assuming an input fuel composition of humidified (~3% H₂O) CH₄, versus the oxygen-to-methane ratio, at 700 (a) and 800°C (b).

At low current density J , and hence low O₂-to-CH₄ ratio χ , the reaction products – primarily solid carbon and hydrogen – indicate methane cracking, *i.e.*



As χ increases up to 0.5, the main change is that solid carbon is replaced by CO. That is, the overall result of SOFC operation at $\chi \approx 0.5$ is approximately electrochemical partial oxidation,



Increasing χ to ≥ 0.5 eliminates coking. This general trend has been reported previously [142]. Finally, as χ increases above 0.5, H₂ and CO are increasingly replaced by H₂O and CO₂, until the reaction become complete oxidation,



at $\chi=2$. Comparing the results at 700 and 800°C, the main difference is that the amounts of H₂O and CO₂ are generally larger at the lower temperature.

Figure 3.11 can be compared directly with the mass spectrometer results shown in Figures 3.9 and 3.10. Note that for a fixed methane flow rate, χ is proportional to the current density J . The rapid increase in CO content and slight increases in CO₂ and H₂O in Figure 3.10 agree well with Figure 3.11. It is not surprising that the experimental results agreed reasonably well with thermodynamic predictions: even if the actual electrochemical reaction products are non-equilibrium, the product gas has ample opportunity to equilibrate as it passes through the thick Ni-YSZ anode. However, there are two major discrepancies between Figure 3.11 and the experimental results. First, the trend in Figure 3.11 is that the H₂ content decreased with χ , whereas in Figure 3.10, it increased with J . Second, while Figure 3.11 predicts that coking is suppressed at high enough J , a quantitative comparison shows that in these low-fuel-utilization

single-cell tests, the overall χ values were well within the predicted coking range. For example, for typical values of methane flow rate, 30sccm, and J , 0.8 A/cm² at 700°C, $\chi = 0.046$ ($\chi \approx 0.08$ including steam already present in the fuel). This value is too low to explain the lack of coking based on Figure 3.11.

Both of these discrepancies can be explained by kinetic suppression of methane cracking (Eq. 3.2), such that at low J the production of both solid C and H₂ were less than that predicted at equilibrium. Instead, it appears that H₂ was produced primarily via reaction with electrochemically pumped oxygen, with the overall final reaction being methane partial oxidation (Eq. 3.3) where CO and H₂ increase together as in Figure 3.10. While slow methane cracking reaction kinetics can explain most of the results, it is difficult to rationalize the good long-term cell stability (Figure 3.5). That is, why did a slow coke buildup not eventually lead to cell failure? A possible explanation is illustrated in Figure 3.12, which shows schematically a simple model for the gas composition versus distance from the electrolyte during direct-methane SOFC operation.

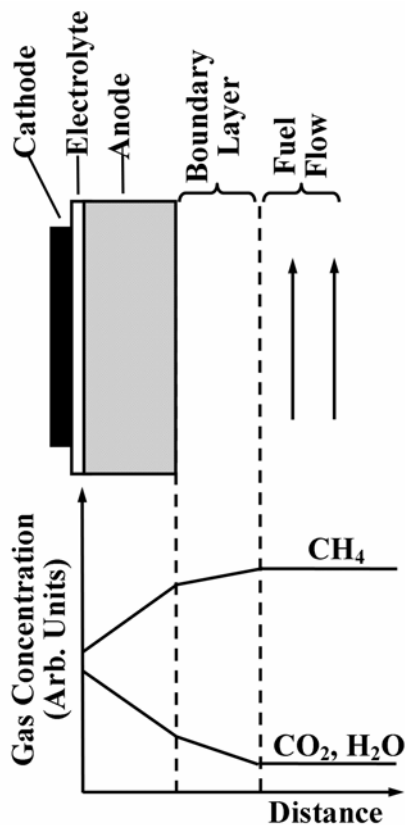


Figure 3.12 Simplified schematic illustration of how reactant and product gas concentrations are expected to vary with position during SOFC stack operation.

It is well known that mass transport through the anode produces substantial partial pressure gradients, especially at high current densities [143]. Thus, the methane partial pressure decreases from the fuel gas stream to the anode free surface to the anode/electrolyte interface, while the product partial pressures follow the reverse trend. This decrease in methane and increase in cell reaction products makes coking less likely, particularly nearest the electrolyte. This picture readily explains the position-dependent coking in the anode shown in Figure 3.7.

The above explanation is more plausible if the anode electrochemical reactions produce primarily H₂O and/or CO₂ as products with substantially less CO and H₂ than expected at equilibrium, such that subsequent reactions



and



will tend to remove solid C. Electrochemical reactions yielding H₂O and CO₂ as products include complete oxidation of methane (Eq. 3.4),

oxidation of solid C and CO,



and oxidation of H₂,



There are several reports [144-146] showing that Eq. 3.9 is the main process on Ni-YSZ anodes in a CH₄-H₂O system when the steam-to-carbon ratio is higher than unity. Thus, a possible scenario is that the main electrochemical reaction is Eq. 3.9, and that the resulting H₂O removes coke via Eq. 3.6, yielding the observed main products H₂ and CO. Another perspective on the above arguments comes from recent studies of carbon growth on Ni particles, which indicate that C growth rates are strongly dependent on the nature of the gas phase species [147]. In the present case, the reaction products present within the anode may alter the kinetics of C growth.

3.5 Summary and Conclusions

Operation of Ni-YSZ anode supported SOFCs directly on methane was studied, and the results are beginning to provide a clearer picture of how these cells operate. The following are the main conclusions:

Power densities as high as 0.52 W/cm^2 at 700°C and 1.27 W/cm^2 at 800°C have been achieved. High open circuit voltages and large limiting currents are key reasons for the good performance in methane.

The SOFCs were stable without coking at $T \leq 700^\circ\text{C}$, except for very low current densities. Direct methane SOFCs will thus be most practical in this temperature range. At higher temperatures, increasingly large currents were required to avoid coking and cell failure.

The high-frequency impedance arc, probably associated with the anode, was substantially larger for methane than for hydrogen.

Mass spectrometer measurements showed that H_2 and CO were the main reaction products, with H_2O and CO_2 minor products – all the products increased with increasing cell current density. While these results were in general agreement with thermodynamic predictions, the lack of coking during direct methane operation was not.

The results suggest that coke-free SOFC operation was achieved due to kinetic limitations on the methane cracking reaction, particularly at low temperature. It is suggested that oxidation of hydrogen, produced by methane reforming by reaction products within the anode, is an important electrochemical reaction; the resulting steam helps remove solid C, thereby suppressing coking at high current densities. More work, particularly detailed modeling of diffusion and reaction processes within the anode, is needed.

CHAPTER FOUR

Improving the Stability of Direct-Methane Solid Oxide Fuel Cells Using Anode Barrier Layers

Chapter 4: Improving the Stability of Direct-Methane Solid Oxide Fuel Cells Using Anode Barrier Layers

4.1 Introductions

Direct-methane solid oxide fuel cells (SOFCs) are of interest as a potentially simple means of electrical generation from natural gas [65], and also for syngas and electricity co-generation by electrochemical partial oxidation [131,148]. There have been numerous reports of stable direct-methane SOFC operation, many of which utilized Ni-based anodes [2,133,149,150]. This is despite the well-known tendency of Ni to coke when exposed to hydrocarbons [147]. Recent studies suggest two main explanations for this apparent discrepancy. First, for SOFCs working at temperatures $<700^{\circ}\text{C}$, the methane pyrolysis kinetics on Ni are relatively slow [139]. Second, SOFC reaction products help suppress coking [151]. This latter point was based on the observation that stable coke-free operation was achieved for SOFC current density above a critical value. The mechanism proposed is that H_2O and CO_2 electrochemical products help remove solid carbon and/or reduce the methane partial pressure (and hence reduce coking) via reforming. However, the rate of reaction product formation at critical current, relative to the methane flow rate, was much too small to explain the non-coking results. The results were thus explained by concentration of reaction products and dilution of methane within the anode due to mass transport limitations.

Figure 4.1a shows schematically the expected methane and reaction product concentrations in the near-anode region during direct-methane SOFC operation [151]. A gas diffusion limitation within the thick Ni-based anode support is assumed [143], giving rise to a decrease in methane

content, and an increase in the product content, going from the free anode surface to the electrolyte. That is, coking should be less favorable near the electrolyte than near the free surface. This proposed mechanism was supported by SEM-EDX measurements showing no coking near the electrolyte even when it was observed near the free surface [151]. Indeed, examination of Fig. 4.1a suggest that gas diffusion gradients will have little effect on coking conditions near the anode free surface, since the diffusivity across the stagnant layer at the anode surface is relatively high.

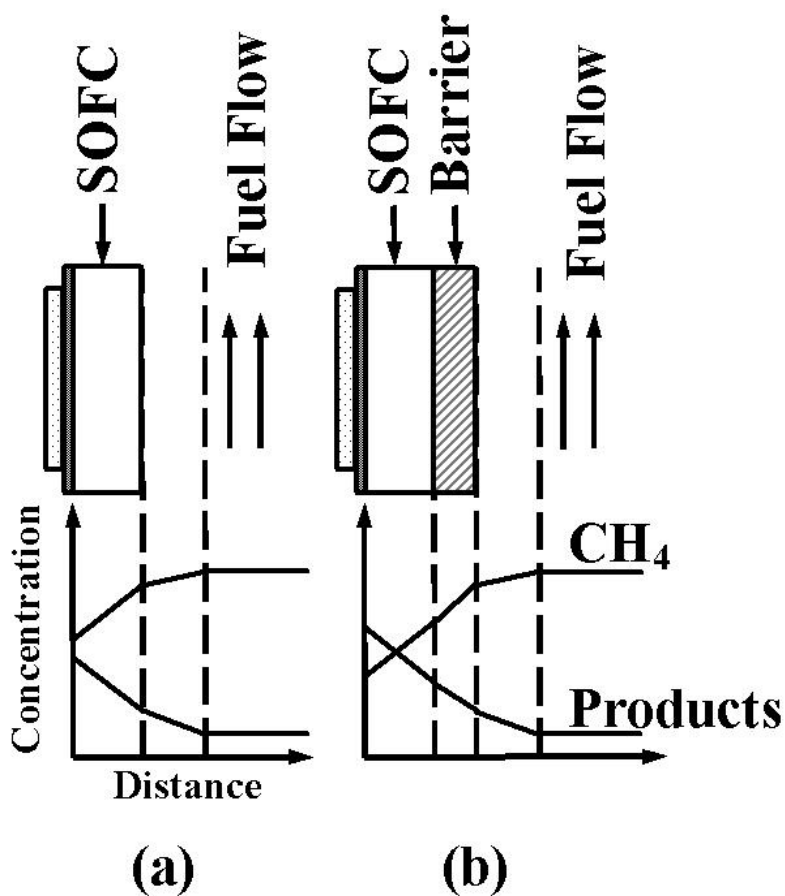


Figure 4.1 Simplified schematic illustration of how reactant and product gas concentrations are expected to vary with position during SOFC operation without (left) and with (right) barrier layers.

In this chapter, we have tested the above theory by adding an inert, non-coking porous layer, *i.e.* a diffusion barrier, to the anode. As illustrated in Figure 4.1b, this should reduce coking via a decrease in methane and increase in product concentrations throughout the anode. Life tests were used to observe cell stability under different operating conditions, and post-test observations were used to observe any carbon deposition.

4.2 Experimental Procedure

The Ni-YSZ anode-supported fuel cells were prepared as follows. Ni-YSZ anode supports were made by mixing NiO (Baker) and 8-YSZ (Tosoh), in a weight ratio of 1:1, and ball milling in ethanol for about 24 hours. Starch of 10wt% was then added to the mixture and the ball milling was continued for another two hours. The milled powder mixture was dried at 75°C, screened with 120-mesh sieve and pressed into pellets with diameter of 19 mm and thickness of about 0.7 mm under pressure of 11000 psi.. The pellets were bisque fired at 1100°C for 4 hours. A NiO–YSZ anode active layer and a thin YSZ-electrolyte layer were then colloiddally deposited on the NiO–YSZ support. The colloidal solutions were prepared by ball-milling the solid powder (YSZ electrolyte or NiO–YSZ anode) in ethanol containing 1% polyethyleneimine as a dispersant and 3% poly(vinyl butyral)–1% ethyl cellulose as a binder. The thickness of the deposited layer was controlled by the volume of the colloidal solution applied. After co-sintering of the anode/electrolyte at 1400 °C for 4 h, Cathodes consisting of a layer of 70wt% $\text{La}_{0.6}\text{Sr}_{0.4}\text{Fe}_{0.2}\text{Co}_{0.8}\text{O}_3$ (LSCF, Praxair) and 30wt% Gd-doped Ceria (GDC, NexTech), followed by pure LSCF layer, were applied by screen printing on the YSZ electrolyte and fired at 900°C for 4 hours.

Barrier layer pellets were composed of partially stabilized zirconia (PSZ) and CeO_2 with the weight ratio of 1:1. Zirconia and CeO_2 are both resistant to coking [34,152]. Pure PSZ layers were also used with similar results. The powders were mixed with 20wt% starch filler in ethanol for 24hrs. Dried mixture powder were pressed into pellets $\approx 0.4\text{mm}$ thick and fired at 1400°C for 4hrs. The porosity as measured by the Archimedes method was 47%-49%.

SOFCs tests were carried out using a standard testing geometry as shown in Chapter 3, both with and without barrier layers that were placed directly against the SOFC anodes. The anodes were reduced in humidified hydrogen at 700°C for several hours and the cell operated in hydrogen for more than 24h, at which time stable cell characteristics were realized. Current-voltage curves were then taken from 600 to 800°C using an Electrochemical Workstation (IM6, ZAHNER), with the cathode exposed to ambient air and the anode to humidified (3% H_2O) hydrogen. Current-voltage curves were then recorded with methane as the fuel, taking care to limit the measurement times at low currents and high temperatures, as these conditions yielded coking that degraded the cells [151]. Life tests were done with a methane flow rate of 30sccm. The SOFC stability region was determined by the same protocol as described in Section 3.2.2.

4.3 Results and Discussion

Figure 4.2 shows results obtained as described in Section 4.2 at 800°C . As shown in Figure 4.2a (no barrier), the cell was fully stable in methane only at relatively large current densities, *i.e.* 1.8 A cm^{-2} at 800°C . For smaller J , V decreased continuously with time. Subsequent observation of the anodes after degradation showed clear coking, as reported in Chapter 3.

With a barrier layer (Fig. 4.2b), V remained stable at current densities down to at least ≈ 0.6 Acm^{-2} . Similar results were observed for a number of similar cells, and slight degradation was typically observed during cell operation at $J < 0.6 \text{A cm}^{-2}$.

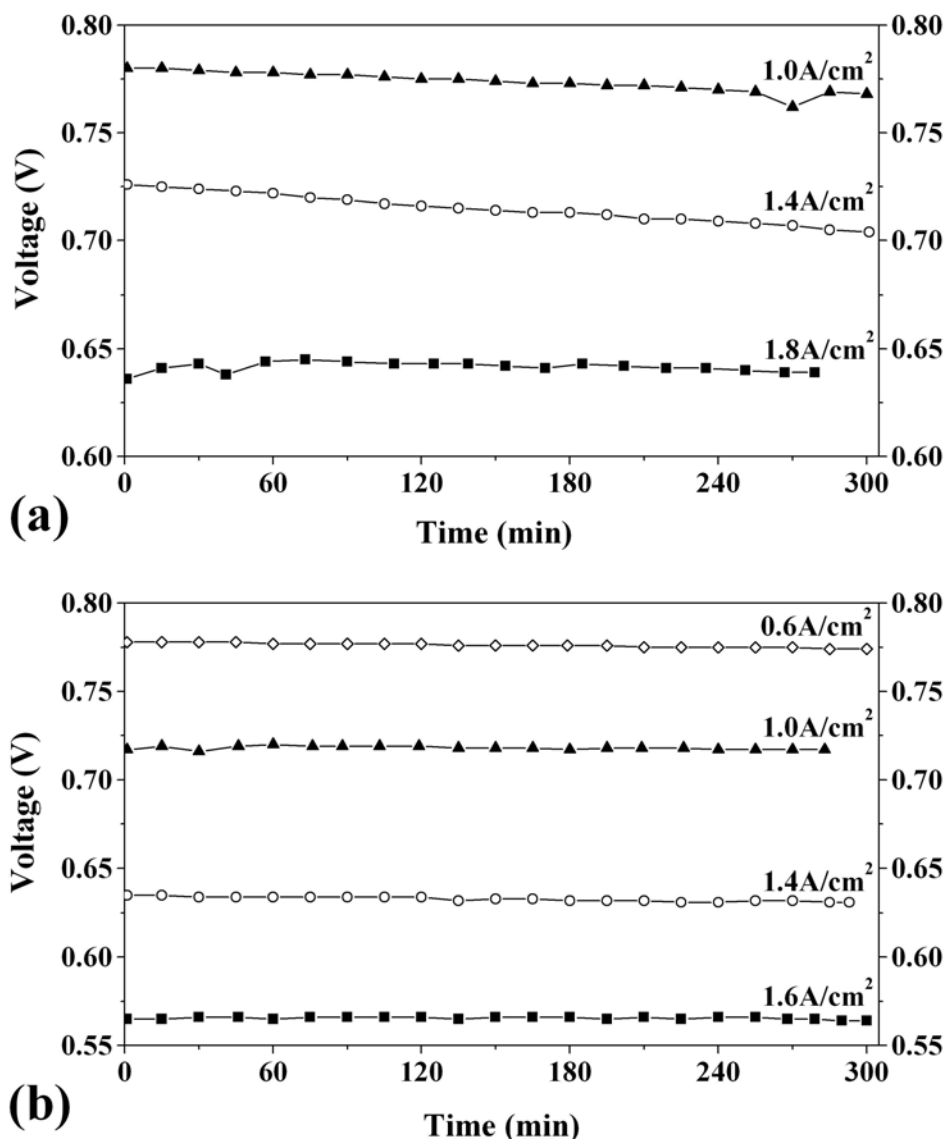


Figure 4.2 Cell voltage versus time at constant current J for SOFCs operated in humidified methane at 800°C without (a) and with (b) barrier layer. The cells were operated at different J values for 6 h in each step, starting at high J and reducing J in steps.

The test shown in Figure 4.2b was stopped at 0.6 A cm^{-2} , however, in order to allow evaluation of the anode after stable operation. Longer-term life testing of a cell with barrier layer operated at $J = 0.6 \text{ A cm}^{-2}$ and 750°C for $\sim 155 \text{ hr}$ is shown in Figure 4.3. Visual observation and SEM-EDX evaluation after this cell test showed no evidence of coke or anode structure degradation, on either the barrier layer or anode. This suggests that the barrier layer prevented coking rather than just slowing the process. Overall, these results showed an expanded stable and non-coking cell operation range with the barrier layer.

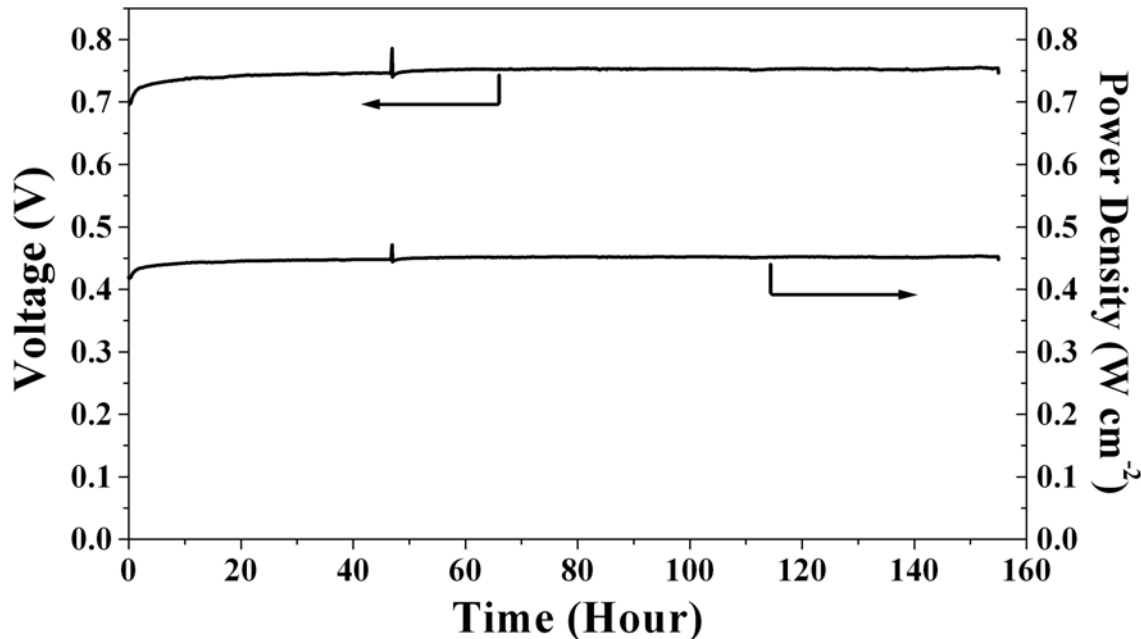


Figure 4.3 Voltage and power density versus time for a SOFC operated in humidified methane at 750°C and 0.6 A/cm^2 with barrier for $\sim 155 \text{ hr}$.

Figure 4.4 provides a direct comparison of SOFC stability with and without barriers at 750 and 800°C , all at $J = 1 \text{ A cm}^{-2}$. Again, the voltage was stable with the barriers, but decreased continuously without the barriers. The initial voltage was $\approx 10\%$ lower with the barrier, presumably a result of the increased gas diffusion polarization. The barriers were also tested at

700°C, but the critical current densities were already $< 0.2 \text{ A cm}^{-2}$ at this temperature [151], making it difficult to discern the barrier layer effect.

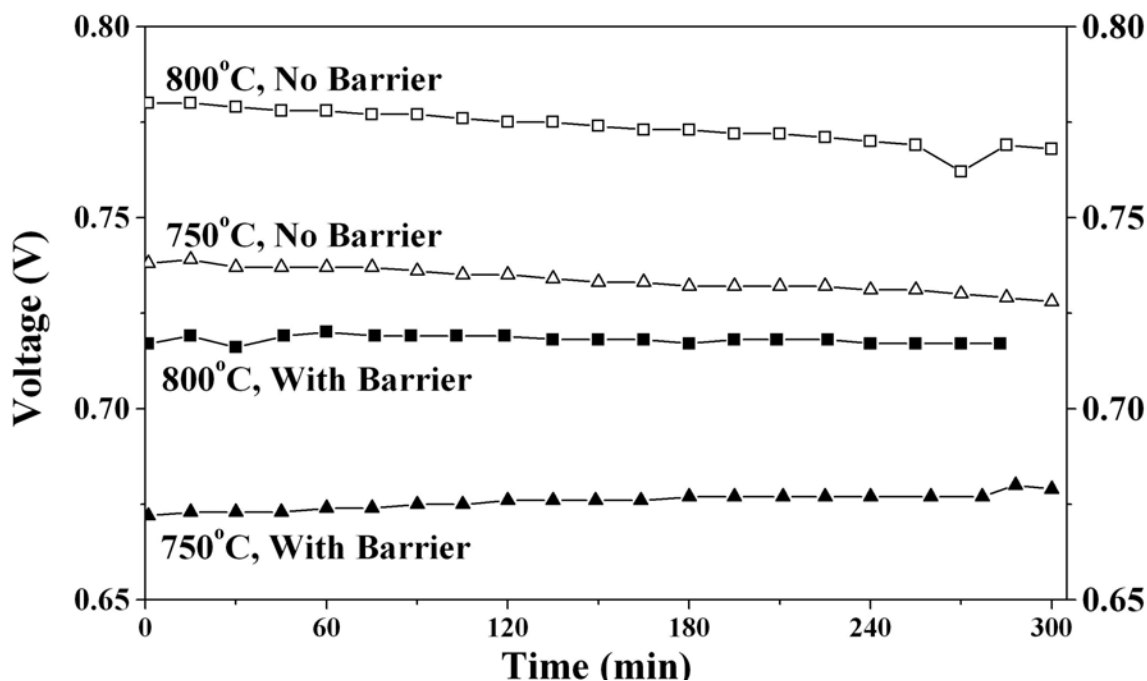


Figure 4.4 Cell voltage versus time at a constant current density $J = 1 \text{ A cm}^{-2}$ for SOFCs operated in humidified methane at 750 and 800°C with (solid dots) and without (open dots) barrier.

Figure 4.5 shows typical voltage V vs. current density J of SOFCs with and without barrier layer operated on 30 sccm humidified methane. Open circuit voltages were lower with the barrier layers, but it should be noted that these were measured during $\sim 3\text{s}$ current interruptions (in order to avoid coking), and a steady state value was not achieved. Limiting current behavior was observed in all cases, but with lower limiting currents with a barrier layer. This is another indication of an increased gas diffusion limitation caused by the barrier, as suggested in Figure 4.1b. The power densities at 0.7V at 800°C were 1.0 W/cm^2 without a barrier layer and 0.8 W/cm^2 with a barrier layer. For these barrier layers, there was thus an $\approx 20\%$ power density penalty at a practical SOFC operating point, due to increased concentration polarization.

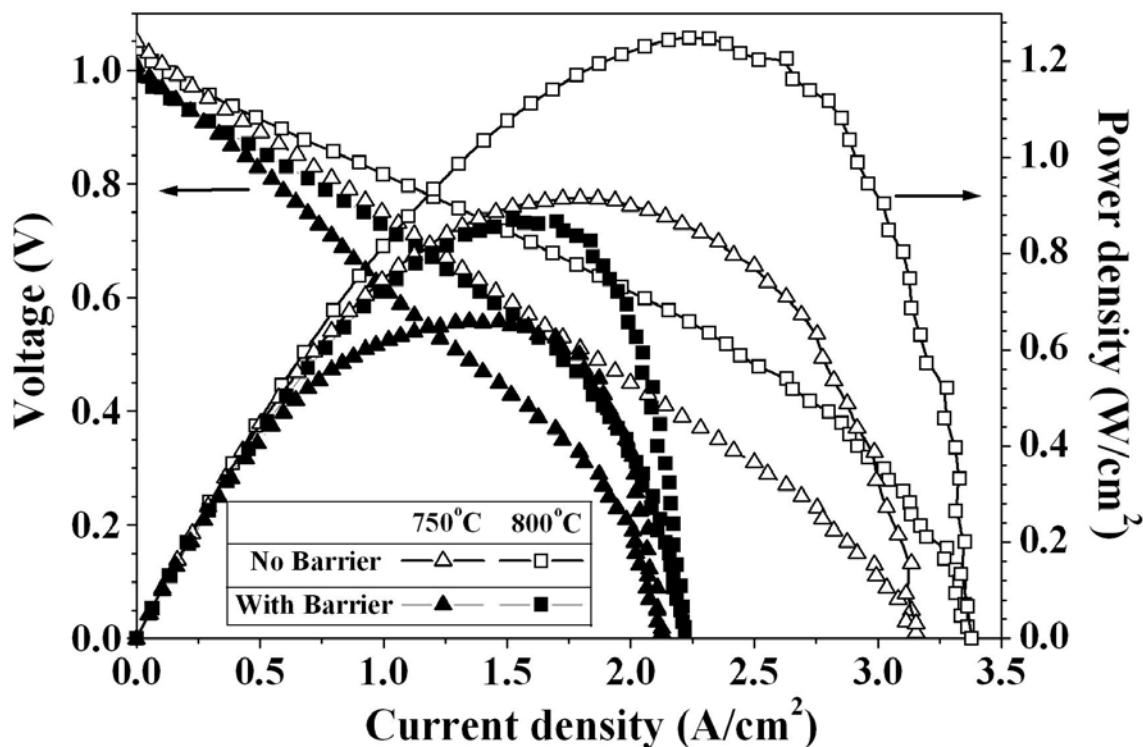


Figure 4.5 Voltage vs. current density of SOFCs with (solid dots) and without (open dots) barrier layer operated on 30sccm humidified methane at 750°C and 800°C.

Barrier layers could be considered as a practical means for making direct methane SOFC stacks more stable against coking. Overall, the present barriers appear to be a reasonable compromise, providing a substantial stability improvement with a small power density penalty. Thinner or more porous barriers could be used to reduce the power density penalty, but this will reduce the effectiveness for suppressing coke formation. It may be useful to vary the barrier layer diffusion resistance versus position in a stack, e.g. using a thicker or less porous barrier near the fuel inlet where coking is most likely, and then reducing and eventually eliminating the barrier downstream where coking is unlikely (*i.e.* the methane content is reduced and product concentrations is large).

We do not believe that the specific material chosen for the diffusion barrier was important – rather, it acted as an inert diffusion-limiting layer. The methane steam reforming catalytic activity of zirconia-ceria diffusion barriers was tested with a micro-channel reactor at different gas composition at 750°C and 800°C. Table 1 shows the experimental conditions and results. There was little or no activity for CeO₂ or doped CeO₂ based materials at such high temperatures, consistent with prior reports [139,147]. However, barrier layers containing a non-coking reforming catalyst, e.g. Ru [153] or Ru-containing perovskites [154], may be useful to further improve anode stability by reforming methane with product molecules before reaching the Ni-based anode. This approach was recently used successfully for iso-octane internal reforming SOFCs [153].

Table 4.1 Steam reforming activity of barrier layer materials.

Catalytic Activity (Methane Conversion Rate %)		
Temperature	Testing Series I ^a	Testing Series II ^b
750°C	0.64	0.71
800°C	0.99	1.6

^a Gas hourly space velocity (GHSV) = 136.06k (hr⁻¹), Gas composition of traditional steam reforming reaction with steam to methane to hydrogen ratio: S/C/H=3/1/1.

^b Gas hourly space velocity (GHSV) = 68.56k (hr⁻¹), Gas compositions simulate that of a fuel cell working at 2.12A cm⁻² with 30sccm humidified methane (3% steam). Equivalent steam to methane to hydrogen ratio is: S/C/H=1/3.62/0.

4.4 Summary and Conclusions

In summary, the present results demonstrate that diffusion barrier layers increase the stable operating parameter range of Ni-YSZ anode-supported SOFCs operating directly with methane. At 800°C, for example, the current density needed for coke-free operation was reduced by a factor of 3. These results are consistent with the simple model wherein the diffusion barrier concentrated reaction products and reduced the methane concentration within the anode (Figure 4.1).

CHAPTER FIVE

High-Rate Electrochemical Partial Oxidation of Methane in Solid Oxide Fuel Cells

Chapter 5: High-Rate Electrochemical Partial Oxidation of Methane in Solid Oxide Fuel Cells

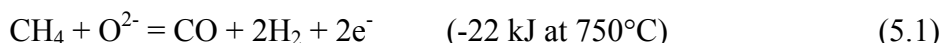
5.1 Introductions

There have been a number of reports of the use of ceramic membrane reactors [155-158] and solid oxide fuel cells (SOFCs) [131,148,159-162] for methane partial oxidation (POx). Both these approaches seek to combine the POx catalytic reaction with electrochemically-produced pure oxygen (*i.e.* electrochemical partial oxidation, or EPOx), thereby yielding syngas without nitrogen dilution. Syngas is an important precursor to synthetic liquid chemicals/fuels including methanol and various hydrocarbons[163-165]. The relative advantages and disadvantages of different methods for converting methane to syngas and other chemicals have been discussed in detail [163]. Key advantages of membrane or fuel cell reactors, compared to POx reactors that utilize cryogenically-produced oxygen, include the reduced cost of the combined reactor and the elimination of explosive methane-oxygen mixtures. Furthermore, it may be possible to avoid thermal gradients arising from the two-step catalytic reaction process [163] – complete oxidation followed by methane reforming – as there have been indications of direct partial oxidation in SOFC reactors [148,160].

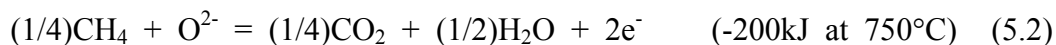
EPOx reactors may also have advantages relative to methane steam reforming reactors, which require excess pressurized steam, have problems with Ni catalyst coking, require relatively large amount of excess heat, and generally produce syngas that is too hydrogen-rich for production of hydrocarbons [163]. Note that steam reforming can be used to convert methane to syngas internal to SOFCs. The syngas is then oxidized to H₂O and CO₂ by the SOFC as it produces

electricity. Thus, such internal reforming SOFCs cannot produce both electricity and syngas. EPOx is distinct from this in that electricity is produced during the reforming process, rather than after reforming, such that syngas can be output as a useful chemical product.

In this chapter we focus on the SOFC reactor approach. Since the desired overall reaction is partial oxidation,



The total SOFC currents and methane flow rates are adjusted to yield an $\text{O}^{2-}/\text{CH}_4$ ratio ≈ 1 . This is quite different than direct-methane SOFCs, where the aim is to produce electricity by completely oxidizing methane,



Comparison of reactions 5.1 and 5.2 shows that for a given sized SOFC (*i.e.* that transports a given amount of O^{2-}), the same amount of electricity (2e^-) is produced, while the methane feed rate and the products are different. This SOFC EPOx approach has two potential advantages over other syngas-production methods. First, two useful products, syngas and electricity, are produced; in contrast, conventional SOFCs produce only electricity and ceramic membranes produce only syngas. Thus, there is the potential for improved economics relative to these methods. In this regard, it is necessary that the methane SOFCs provide competitive power densities to state-of-the-art electricity-only SOFCs, and similar syngas production rates as membrane reactors. However, in many prior results [131,148,160], SOFC power densities and syngas production rates were quite low. A second advantage is that EPOx can potentially build on an increasingly well-developed SOFC technology. However, this latter point is an advantage only if the SOFCs being developed for electricity generation can be adapted with

minor changes to use methane instead of hydrogen. Unfortunately, prior demonstrations of EPOx involved SOFCs quite different than those being actively developed as electrical power sources. For example, the most successful demonstrations have been made with (La,Sr)(Ga,Mg)O₃ electrolyte SOFCs [159,162] rather than the more standard YSZ electrolytes, and methane conversion was relatively low. Other issues with prior EPOx SOFC reports are that methane diluted with, e.g., N₂ or He was used rather than pure methane, and life tests were limited to ~ 10h. This latter point is especially important given the possible problem with coking in direct-methane SOFCs [139].

Here we present experimental results on EPOx carried out in planar Ni-YSZ anode-supported SOFCs operated with pure methane that provide high power densities, high syngas production rates, and high methane conversion. The SOFCs were similar to those being widely developed for electrical-generation applications, with the primary modification being the addition of a barrier layer at the SOFC anode. Stable operation without coking was demonstrated for a few hundred hours. Thermodynamic calculations of expected products are presented and used to estimate the thermal balance in EPOx SOFCs, and used as a guide for SOFC operating conditions.

5.2 Experimental Procedures

5.2.1 Equilibrium Calculations

A thermodynamic calculation described previously [166], similar to that reported by Koh [137], was used to predict the expected equilibrium products versus O²/CH₄ ratio and temperature. The calculation minimizes the total Gibbs free energy of all species with the conservation of all

elements in the system, starting with handbook values of the standard free energies [167]. A program based upon the Taylor expansion and Lagrange method of undetermined multipliers was coded to solve the problem of minimization with constraints. In order to better match the present experimental results and prior work showing no carbon in direct-methane SOFCs [2,4,133,138,151,168], solid C was not allowed.

5.2.2 Fuel Cell and Barrier Layer Preparation

The SOFCs used in this study were fabricated as reported previously [153], consisting of Ni-YSZ anode supports (YSZ=8 mol% Y_2O_3 -stabilized ZrO_2), thin YSZ electrolytes, and LSM-YSZ cathodes (LSM= $\text{La}_{0.8}\text{Sr}_{0.2}\text{MnO}_3$). The anode substrates were pressed from NiO and YSZ (50/50wt) powders with 10% starch filler, and then bisque fired at 1100°C. A NiO-YSZ anode active layer and a thin dense YSZ electrolyte layer were deposited on the NiO-YSZ supports using a colloidal deposition technique similar to that described previously [169]. The anode/electrolyte bi-layers were fired at 1400°C for 6h. LSM-YSZ cathode layers were applied and fired at 1250°C for 1 h. Then a second layer of pure LSM slurry was applied and fired at 1250°C for 1 h. The final fuel cells were ~ 2.5 cm in diameter, with anode thickness of ~ 0.6 mm, electrolyte thickness of ~ 10 μm , and cathode thickness of 20–30 μm . Estimated anode porosity was $\approx 40\%$, and cathode porosity was $\approx 30\%$. The cathode area, which defined the cell active area, was ~ 2.4 cm^2 .

In some cases as noted below, a barrier or catalyst layer was placed adjacent to the SOFC anode. These were thin porous discs $\approx 0.3\text{mm}$ thick consisting of partially stabilized zirconia. When a catalyst was used, it was a $\approx 15\ \mu\text{m}$ thick Ru(10%)- CeO_2 layer screen printed on both

sides. The addition of a barrier, or barrier with catalyst, helped to reduce the parameter range under which coking could occur [170,171].

5.2.3 Fuel Cell Testing and Mass Spectrometer Measurement

Methane was used here as a well-controlled surrogate for natural gas. Methane is the primary constituent of natural gas, which also contains varying amounts (typically a few percent) of higher hydrocarbons and a small amount (a few ppm) of sulfur compounds. We have previously shown that the higher hydrocarbons in natural gas do not significantly alter SOFC operation compared with pure methane [2]. Sulfur impurities present in natural gas are typically removed prior to use in fuel cells [36]. Thus, differences between the present methane results and those for natural gas are expected to be minor.

Single cells were tested in a tube furnace using a standard testing geometry as illustrated in Figure 5.1. A slightly modified test setup, where an alumina ceramic disc was attached to the end of the gas feed tube, was used in some of the tests. Ambient air was maintained on the cathode side. After reducing the anode NiO to Ni and initial electrical testing in humidified hydrogen, electrical measurements were done in pure methane. The fuel exhaust gas was sampled via a capillary tube with inlet placed near the anode, and was analyzed using a Transpector 2® Gas Analysis System (Inficon L100, electron impact ionization using 40 eV electrons) that was differentially pumped to a measurement pressure of $\approx 5 \cdot 10^{-5}$ Torr using a turbomolecular pump. Note that H₂O was removed from the products using a dessicant in order to avoid poisoning of the mass spectrometer.

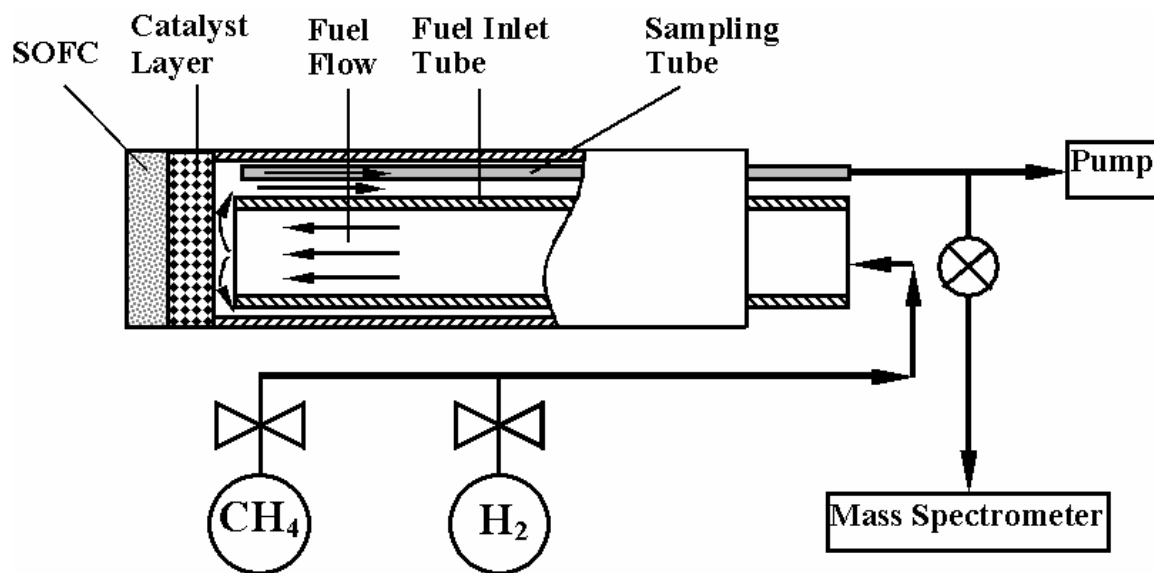


Figure 5.1 Schematic of fuel cell testing setup

5.3 Results and Discussion

5.3.1 Equilibrium Calculations

Predicted equilibrium products versus the O^2/CH_4 ratio at a typical SOFC operating temperature of 750°C are shown in Fig. 5.2. H_2 and CO increase with increasing O^2/CH_4 to a maximum at $O^2/CH_4 \approx 1$, while CH_4 decreases and H_2O and CO_2 remain relatively low. For $O^2/CH_4 \approx 1$, the products agree reasonably well with Eq. (5.1). When the O^2/CH_4 ratio is increased above ≈ 1 , H_2 and CO decrease while H_2O and CO_2 increase, eventually reaching the composition given by Eq. (5.2) at $O^2/CH_4 = 4$.

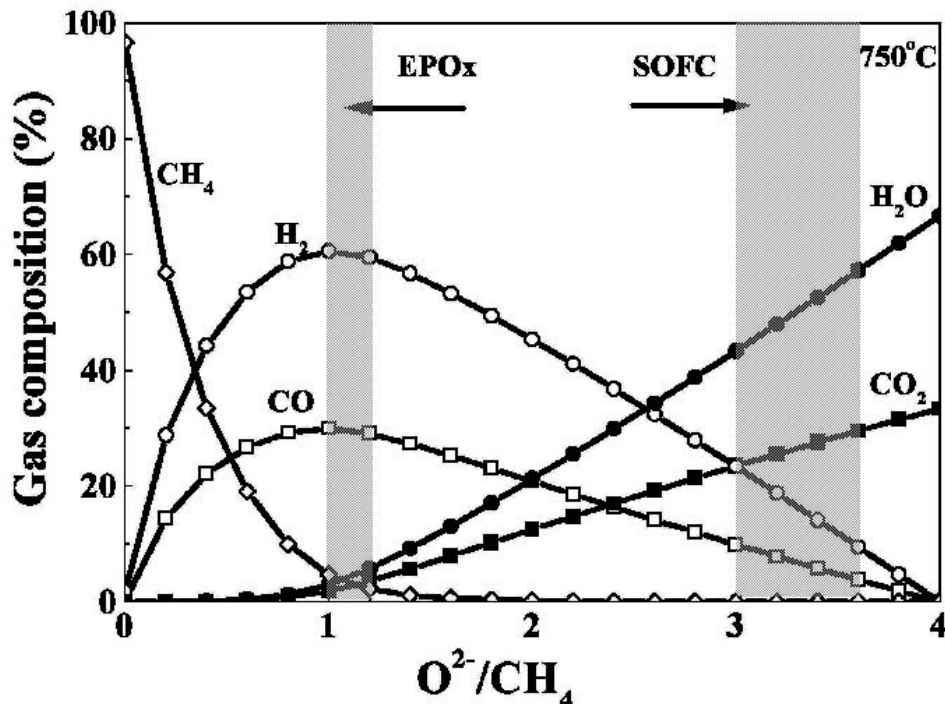


Figure 5.2 Predicted equilibrium fuel gas composition versus O^{2-}/CH_4 ratio at $T = 750^\circ C$, with the assumption that solid carbon does not form.

Equilibrium calculations were also used to estimate conditions where the EPOx SOFC reactor can be thermally self-sustaining. A minimum condition for this is that the net reaction enthalpy change $-\Delta H$ should equal the energy extracted as electricity (E_{FC}):

$$-\Delta H = E_{FC}. \quad (5.3)$$

Note that the exothermic enthalpy change in partial oxidation, $-\Delta H_{PO} = 22 \text{ kJ/mol } CH_4$ at $750^\circ C$, is small relative to the expected electrical output $E_{FC} = nFV = 135 \text{ kJ/mol } CH_4$ assuming a typical SOFC operating voltage $V = 0.7V$ (here $n=2$ is the number of electrons in Eq. (5.1) and F is Faraday's constant). This situation can be improved by reducing the operating voltage, such that less electrical energy is extracted per mole of methane. Another measure that can be used to produce more heat is to increase O^{2-}/CH_4 above 1, which increases the amount of H_2O

and CO_2 produced with substantial additional heat release (see Eq. (5.2)). Fig. 5.3 shows a plot of the $\text{O}^{2-}/\text{CH}_4$ and cell operating voltage values that satisfy Eq. (5.3) at 750°C , where ΔH was calculated using the predicted equilibrium product composition. The results are approximate because heat losses, *e.g.* due to imperfect heat exchangers and a non-adiabatic reactor, were not included in Eq. (5.3). Figure 5.3 shows that a lower V allows operation at lower $\text{O}^{2-}/\text{CH}_4$ values, *e.g.* 1.22 at 0.4 V versus 1.89 at 0.7 V at 750°C . Fig. 5.3 also shows that decreasing V and $\text{O}^{2-}/\text{CH}_4$ increases the predicted syngas content of the products, *e.g.* from 70% at $V=0.7\text{V}$ to 88% at $V=0.4\text{V}$, mainly due to a decrease in H_2O and CO_2 , although the amount of un-reacted methane increases slightly. Calculations done at different temperatures, assuming thermo-neutral conditions (*i.e.* satisfying Eq. (5.3)) and $V=0.4\text{V}$, predicted high syngas productivity and methane conversion with relatively low H_2O and CO_2 content for temperatures $>700^\circ\text{C}$.

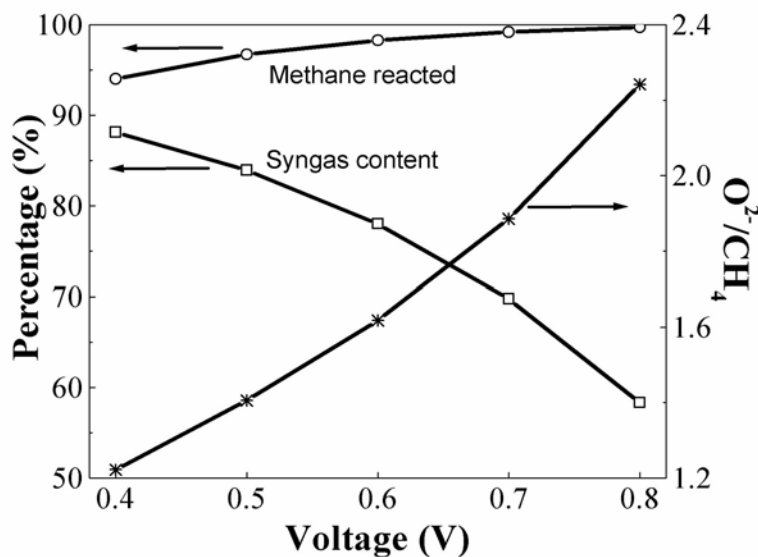


Figure 5.3 $\text{O}^{2-}/\text{CH}_4$ ratio predicted to yield thermo-neutral SOFC operation versus cell operating voltage at 750°C . Also shown are the percentage of methane reacted and the syngas content of the product for the thermo-neutral condition.

The operation of a SOFC at $V=0.4V$ would normally be expected to yield low fuel efficiency. The EPOx mode of operation is quite different, however, because the net fuel cell reaction is essentially partial oxidation, with a relatively low value of ΔH (see eqs. 1 and 2) compared to the essentially complete oxidation in a normal fuel cell. Thus, the net fuel cell efficiency, defined as $E_{FC}/\Delta H = nFV/\Delta H$, can be relatively high even for unusually low voltage. Another way of arguing this is the following: while the electrical energy output per mole of methane is relatively small, there is considerable energy value in the syngas produced that should also be considered in calculating efficiency.

5.3.2 SOFC Electrical Test Results

Fig. 5.4 illustrates typical SOFC results for voltage V and power density P versus current density J , measured at $750^{\circ}C$. Note that the O^{2-}/CH_4 ratio, also shown, was proportional to J since the CH_4 flow rate was fixed at 30 sccm. The cell performance was not measured at lower current density due to the risk of coking under these conditions [151]. V decreased with increasing J , while P increased to a maximum of 0.75 W/cm^2 at $J \approx 1.6 \text{ A/cm}^2$ before decreasing at higher J . Fig. 5.4 shows that V values as low as $0.4V$, beneficial from the thermal balance viewpoint as shown in Fig. 5.3, can be used without compromising SOFC power density. Fig. 5.4 also illustrates another advantage of lower V : decreasing from a typical SOFC voltage $V = 0.7$ to $0.4V$ approximately doubles the oxygen ion current density J and the syngas production rate (the latter from Eq. (5.1)).

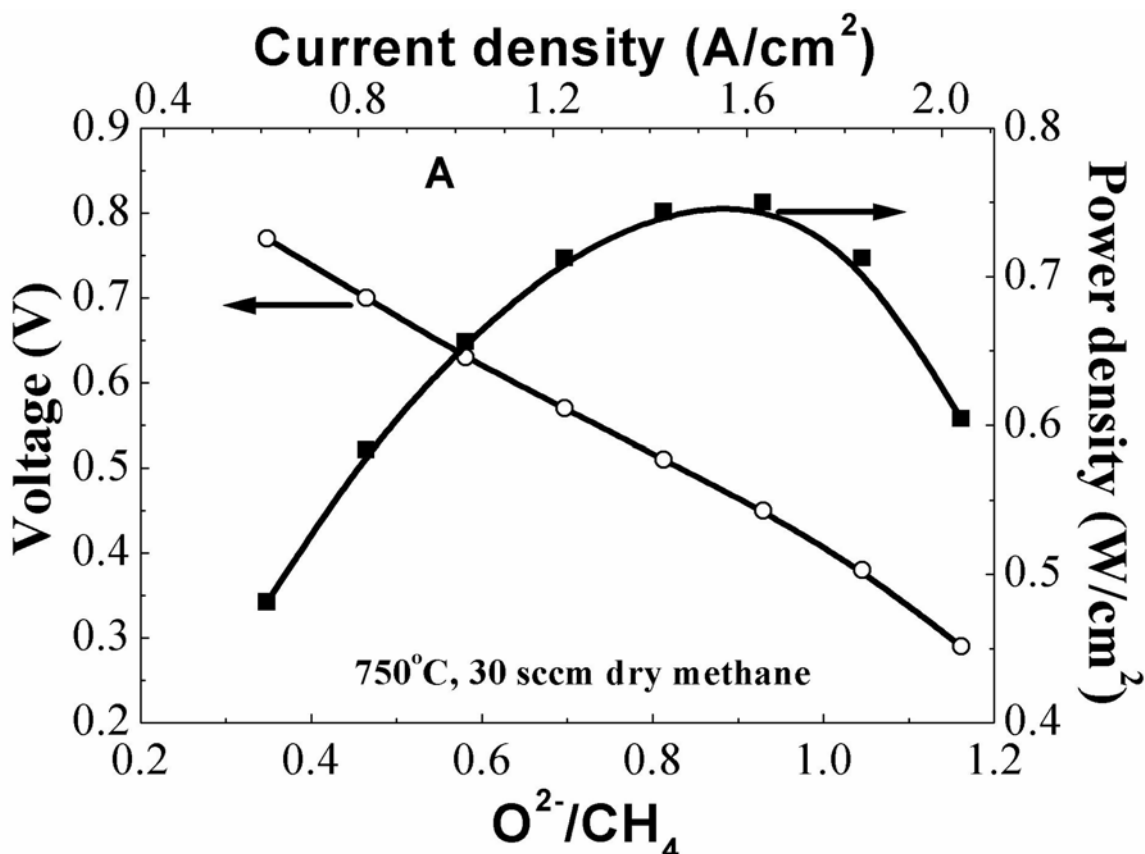


Figure 5.4 Voltage and power density versus current density (and $\text{O}^{2-}/\text{CH}_4$ ratio) for the SOFC NiO-YSZ|YSZ|YSZ-LSM, LSM, tested in 30 sccm dry methane in the anode and ambient air in the cathode at 750°C.

The present way of operating a SOFC, with pure methane fuel, low V , and high J , is unusual, so it is important to demonstrate that the cells can operate stably. Endurance tests carried out on a number of cells showed stable operation. Fig. 5.5 shows an example of a >300h SOFC life test. The test was carried out with an anode catalyst layer using dry methane at 30 sccm, $\text{O}^{2-}/\text{CH}_4 = 0.82$, $V \approx 0.4$ V, and 750°C. The SOFC showed a slight performance decrease during the first 150h, followed by stable operation for the final 200h at ≈ 0.6 W/cm^2 . The initial performance decrease may have resulted from the relatively high current density, as a prior direct-methane life test at lower current and 700°C showed no initial degradation [151]. Fig.

5.6 shows scanning electron microscope (SEM) images and energy-dispersive x-ray (EDX) analysis of the SOFC anode. The anode microstructure showed no evidence of any changes relative to a cell tested under conventional SOFC conditions in H₂ fuel, and the EDX spectra showed only a small carbon peak that was near the background level and similar to that for a cell tested with H₂ fuel. That is, no carbon was detected on the anode within the sensitivity of the measurement. Further life testing over longer time frames is needed to fully demonstrate stable SOFC operation under EPOx conditions.

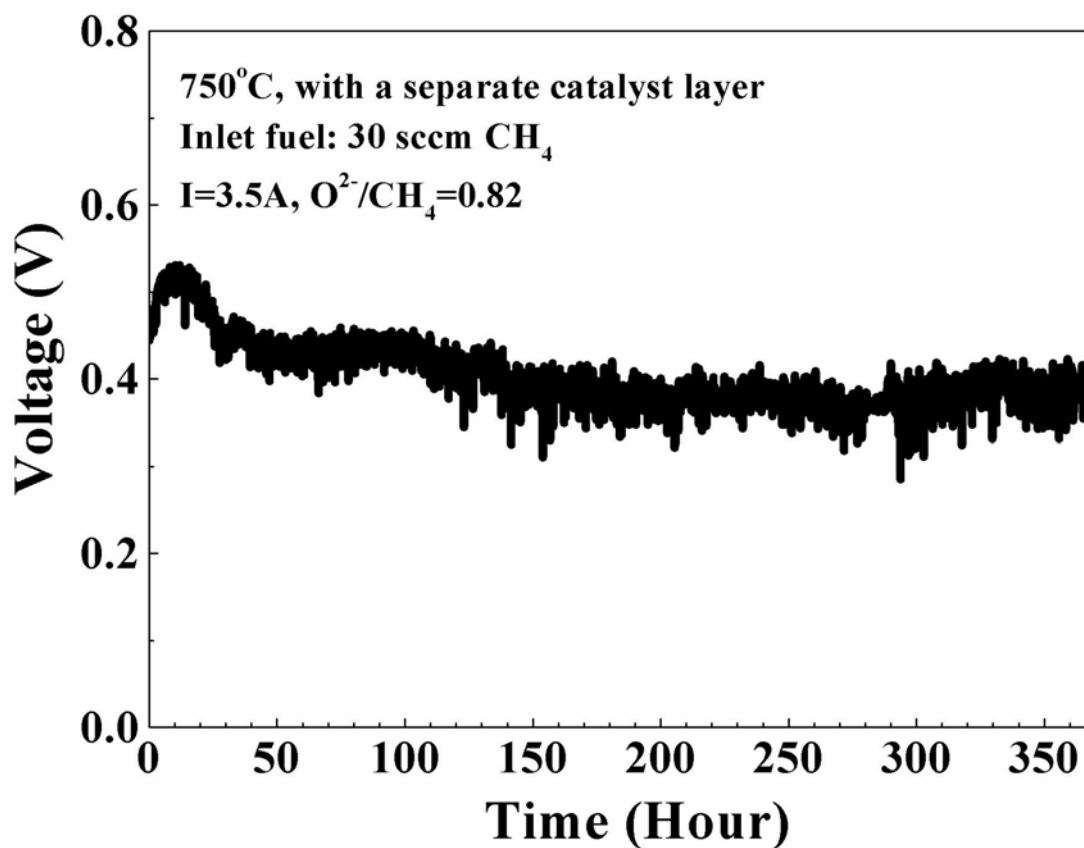


Figure 5.5 Voltage versus time for the SOFC, Ni-YSZ|YSZ|LSM-YSZ,LSM, with a catalyst layer, Ru-CeO₂|PSZ|Ru-CeO₂, and 3.5 A (O²⁻/CH₄=0.82).

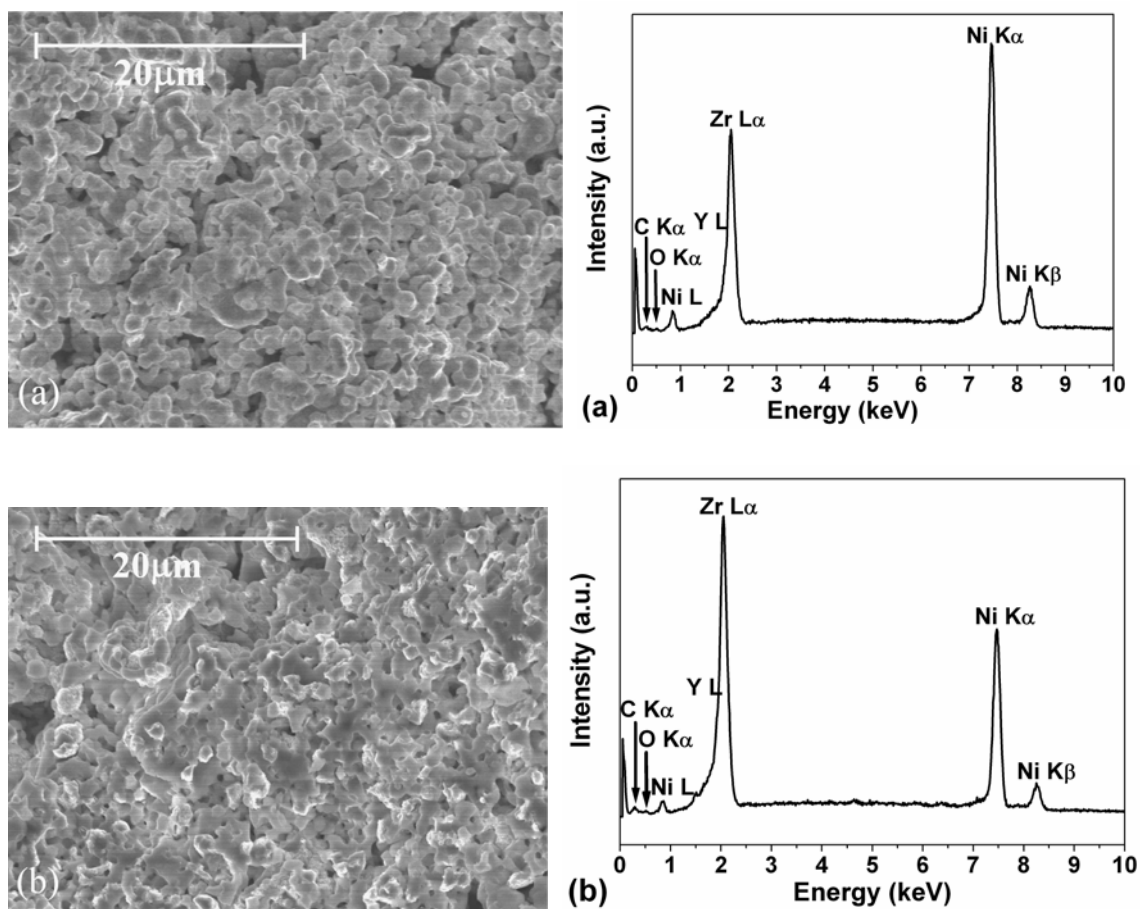


Figure 5.6 Fracture cross-sectional SEM micrographs and EDX spectra taken from anodes after stable SOFC operation in (a) humidified hydrogen and (b) dry methane at 750°C and $J = 1.46\text{A}/\text{cm}^2$.

5.3.3 Product Gas Composition

Fig. 5.7 shows typical mass spectra of the anode reaction products for SOFCs operated on methane at 750°C and three different current densities. The spectrum at open circuit (Fig. 5.7a) shows main peaks at mass 2 (H_2^+), 15 (CH_3^+), and 16 (CH_4^+), reasonably corresponding to the input gas composition. The small H_2^+ peak was presumably due to methane cracking, indicating that solid C was depositing; this low J condition was generally avoided to prevent the deleterious

C deposition [151]. Slight gas leakage in the fuel cell seals may explain small peaks at mass 28 (N_2^+ and CO^+) and 44 (CO_2^+). Overall, there was no apparent partial oxidation reaction at open circuit ($\text{O}^{2-}/\text{CH}_4=0$). At non-zero J values, peaks at mass 2 (H_2^+), 28 (CO^+), and 44 (CO_2^+) increased substantially while the CH_3^+ and CH_4^+ peaks decreased relative to Fig. 5.7a, as shown for $\text{O}^{2-}/\text{CH}_4=0.7$ (Fig. 5.7b) and $\text{O}^{2-}/\text{CH}_4=1.16$ (Fig. 5.7c).

Fig. 5.8 summarizes results as shown in Figure 5.7. H_2 and CO increased to maximum values at $\text{O}^{2-}/\text{CH}_4 \approx 0.7$ before decreasing with further increases in $\text{O}^{2-}/\text{CH}_4$. The CH_4 content decreased with increasing $\text{O}^{2-}/\text{CH}_4$. The CO_2 content remained low at low $\text{O}^{2-}/\text{CH}_4$ but then increased more rapidly when $\text{O}^{2-}/\text{CH}_4$ increased above 0.7. These trends agree with the equilibrium prediction given in Fig. 5.1, except that CH_4 does not decrease to zero at large $\text{O}^{2-}/\text{CH}_4$, and the peak H_2 and CO content appears well below the predicted value $\text{O}^{2-}/\text{CH}_4 = 1$. Both these differences can be explained if a fraction of inlet CH_4 flow does not react, possibly due to the flow geometry of our SOFC test (Fig. 5.1).

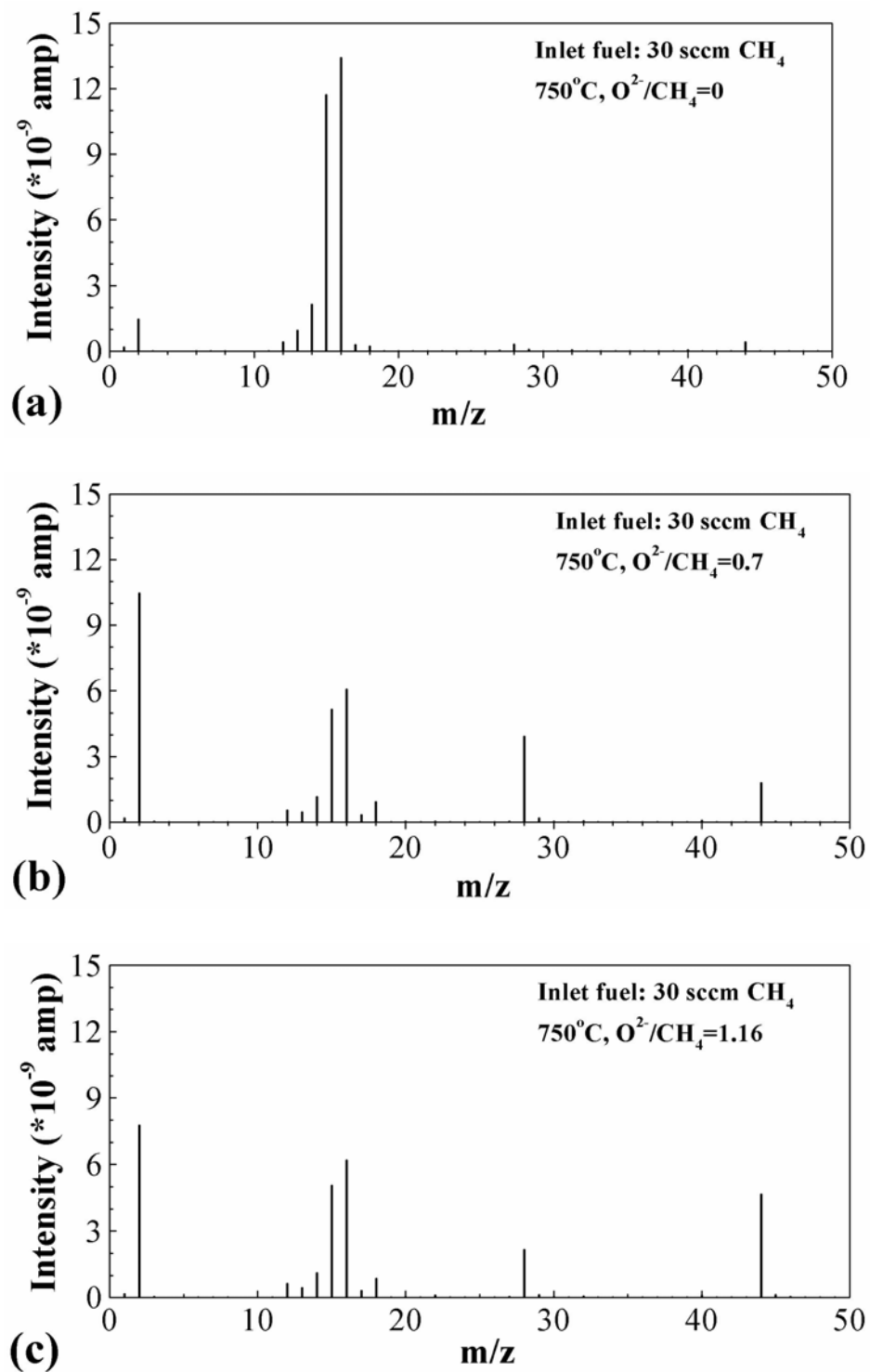


Figure 5.7 Typical mass spectra of SOFC reaction products at 750°C for 30 sccm dry methane at O^2/CH_4 values of (a) 0, (b) 0.7 and (c) 1.16.

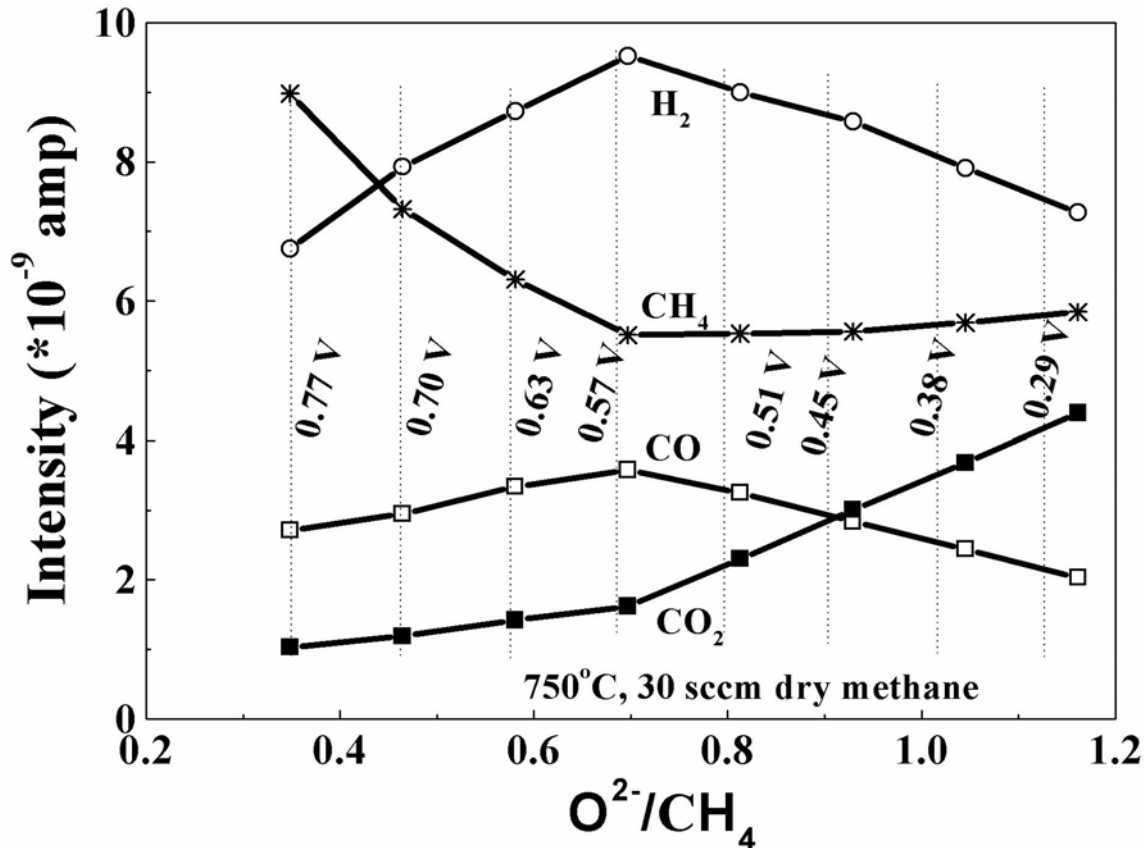


Figure 5.8 The product gas peak intensity versus O^{2-}/CH_4 ratio measured during the test shown in Figure 5.4.

In order to test the above explanation, we did additional experiments with an altered geometry where all CH_4 flowed over the full radius (~ 1 cm) of the anode. Figure 5.9 shows schematically the original and modified geometries, and plots the methane utilization versus O^{2-}/CH_4 for both cases. In the new geometry, an annulus was used with a small hole at the center and a diameter nearly equal to the inside diameter of the test chamber. The new geometry also featured a reduced distance (≈ 1 mm versus ≈ 10 mm in the old setup) between the fuel inlet and the SOFC. These changes were made to force the fuel to flow radially across the surface of the anode, a geometry similar to radial-flow SOFC stack geometries. While fuel channel geometry in a stack will be constrained by other considerations (*e.g.* system issues such as desired fuel

pressure gradient), our methane conversion results were not strongly dependent on channel width; thus, it should be possible to achieve high methane conversion for reasonable stack fuel channel geometries. Figure 5.9 shows that the methane utilization saturated at $\approx 70\%$ for the original geometry, but for the altered geometry increased continuously to $\approx 90\%$ for O^2-/CH_4 increased to 1. In the new geometry, the H_2 and CO mass spectrometer peaks increased continuously with increasing O^2-/CH_4 in this range, in better agreement with the thermodynamic prediction than in Figure 5.8. The maximum measured syngas production rate estimated based on mass spectrometer sensitivities was ~ 20 sccm cm^{-2} .

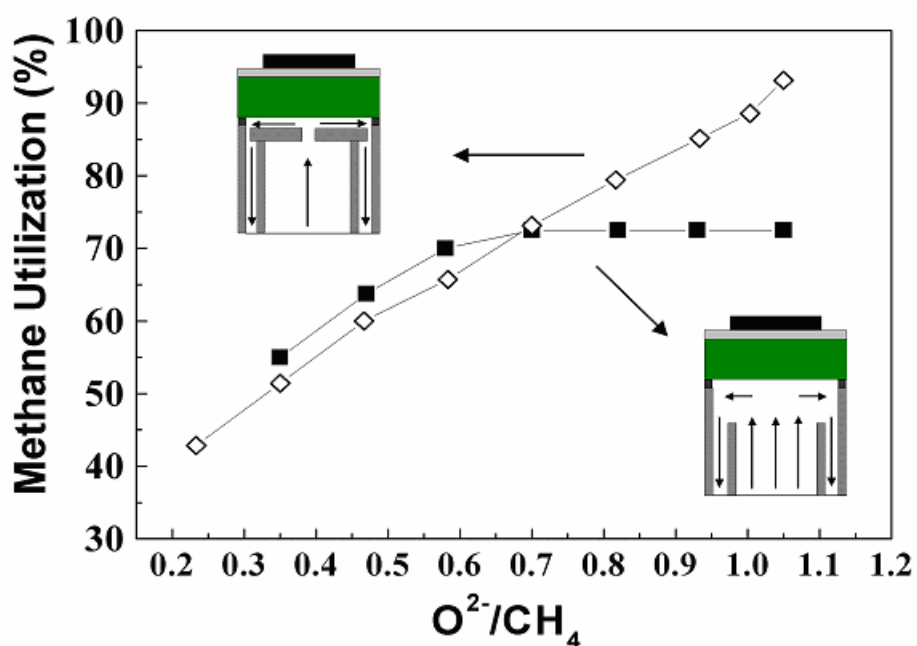


Figure 5.9 Methane utilization versus O^2-/CH_4 ratio for SOFCs operated on 30 sccm dry methane at $750^\circ C$. Results are compared for identical SOFCs with the standard (■) and modified (◇) gas-flow geometries indicated schematically in the insets (the arrows illustrate the fuel flow path).

While the products in Fig. 5.8 indicate partial oxidation of methane, it is not clear that the POx reaction occurred via a simple one-step process. Catalytic methane POx typically occurs by a two-step process, complete oxidation followed by reforming [163]. On the other hand, some SOFC EPOx results suggest a single-step POx reaction [148,160]. Visual observations of the cells during operation did not show evidence of substantial temperature gradients, as might be expected for a two-step process [163]. However, even in the case of a two-step process, the oxidation and reforming reactions may occur in close proximity yielding no substantial temperature gradients. The present results thus do not provide a definitive answer regarding reaction mechanism.

5.4 Summary and Conclusions

We have demonstrated that Ni-YSZ anode-supported SOFCs operated with pure methane fuel can produce both syngas and electricity without coking. The results show that SOFCs operated at $T \approx 750^\circ\text{C}$, $V \approx 0.4\text{V}$, and $\text{O}^2/\text{CH}_4 \approx 1.2$ yield stable high electrical power output ($\sim 0.7\text{W}/\text{cm}^2$) and high syngas production rates ($\sim 20\text{ sccm}/\text{cm}^2$). Equilibrium calculations suggest that the SOFC reactor should be thermally self-sustaining under these conditions.

CHAPTER SIX

Co-Firing of Anode-Supported Solid Oxide Fuel Cells with Thin $\text{La}_{0.9}\text{Sr}_{0.1}\text{Ga}_{0.8}\text{Mg}_{0.2}\text{O}_{3-\delta}$ Electrolytes

Chapter 6: Co-Firing of Anode-Supported Solid Oxide Fuel Cells with Thin $\text{La}_{0.9}\text{Sr}_{0.1}\text{Ga}_{0.8}\text{Mg}_{0.2}\text{O}_{3-\delta}$ Electrolytes

6.1 Introduction

Yttria-stabilized zirconia (YSZ) has been studied extensively since Baur and Preis first used it as electrolyte in fuel cell application in 1937. Initial YSZ SOFCs were constructed on electrolyte support and operated at 950-1000°C to acquire high ionic conductivity. With successful preparation of YSZ thin films (*ca.* 10 μm) on electrode substrates, YSZ SOFCs have achieved power densities as high as 1.4-1.9 W/cm² at 800°C [102,143,151]. However, YSZ shows poor oxide ionic conductivity below 700°C, which inevitably limited its application in intermediate temperature range. Currently, the major development trend of SOFCs is to decrease the operating temperature while maintaining high power density. Lower operation temperature will alleviate the challenges in choices of interconnect and sealing materials. For direct methane SOFCs, the carbon deposition rate is significantly reduced at low temperatures. However, with the decrease of the operating temperature, the oxide ionic conductivity of the electrolyte decreased exponentially, which leads to higher ohmic loss and lower power density. Hence, the selection of electrolyte materials and fabrication technology play crucial roles in meeting the challenges. Electrolyte materials with high oxide ionic conductivity and various thin film technologies have been adopted to reduce the IR loss of SOFC operating at intermediate temperature (500°C < T < 800°C).

Strontium and magnesium doped lanthanum gallate (LSGM) was first reported as a fast oxide ion conductor by Ishihara *et al* in 1994 [55]. LSGM exhibits several times higher oxide ionic

conductivity than YSZ with negligible electronic conductivity and good chemical stability over a wide oxygen partial pressure range ($P_{O_2}10^{-22}$ to 1atm). Therefore, LSGM is receiving attention as a substitute for yttria-stabilized zirconia electrolytes in solid oxide fuel cells (SOFCs). Thin LSGM electrolyte SOFCs could potentially operate at temperatures lower than YSZ-electrolyte SOFCs. For example, the expected area-specific resistance of a $\approx 10 \mu\text{m}$ thick LSGM electrolyte at 600°C is $\approx 0.05 \Omega\text{cm}^2$ [172]. This is low enough that, when combined with electrode polarization resistances, a target cell resistance of $0.3\Omega\text{cm}^2$ (yielding $\approx 1\text{W}/\text{cm}^2$ power density) can be achieved. For comparison, the resistance of a $10 \mu\text{m}$ thick YSZ layer is $\approx 0.4 \Omega\text{cm}^2$ at 600°C [172], too high to reach $1\text{W}/\text{cm}^2$.

Electrolyte-supported and thick film LSGM SOFCs have been fabricated and have shown excellent performance at 800°C [173-175]. However, fabrication of thin electrode-supported LSGM layers [176,177] has proven challenging because of chemical reactions or ionic migration during high-temperature co-firing with electrodes. Indeed, the most successful thin-LSGM SOFCs were fabricated using a low temperature process, physical vapor deposition, to produce very thin Sm-doped Ceria (SDC) barrier layers between the LSGM and electrodes. In co-fired LSGM cells, however, a $(\text{Ce}_{0.6}\text{La}_{0.4})\text{O}_x$ (LDC) must be used to minimize reactions and interdiffusion between LSGM and the NiO-containing anode and the cathode. The 40% La content helps to maintain a constant La chemical potential in the electrolyte and barrier layers, thereby avoiding La out-diffusion from the LSGM layer [54,178,179]. Nonetheless, fabrication of thin-LSGM electrolyte SOFCs by co-firing has remained problematic.

In this chapter, we explored the use of co-firing to prepare anode-supported thin-LSGM electrolyte SOFCs with LDC interlayers. Dense thin LDC/LSGM/LDC layers on NiO-LDC

anode substrates by co-sintering were demonstrated, with no evidence of deleterious reactions. SOFC testing yielded relatively high power densities but open-circuit voltages were lower than expected, apparently due to Ni in the LSGM. Issues with this approach to thin-LSGM SOFCs are discussed.

6.2 Experimental Procedure

6.2.1 Powder Preparation

$\text{La}_{0.9}\text{Sr}_{0.1}\text{Ga}_{0.8}\text{Mg}_{0.2}\text{O}_{3-\delta}$ (LSGM) powder was prepared via solid-state reaction. Stoichiometric amounts of La_2O_3 , SrCO_3 , Ga_2O_3 and MgO were mixed in ethanol alcohol for 24 hrs. The slurry was dried and fired at 1250°C for 12hrs. $\text{La}_{0.4}\text{Ce}_{0.6}\text{O}_{2-\delta}$ (LDC) powder was also produced by solid-state reaction of La_2O_3 and CeO_2 after firing at 1250°C for 12hrs. After grinding and sieving with 200# mesh screen, the powders were studied with X-ray diffraction (XRD) in a diffractometer with Cu K_α radiation. The XRD patterns (Figure 6.1) were analyzed and determined with Jade 6.5 software. The results showed good agreement with expected peaks for LSGM and LDC [54,175], with no indication of second phases.

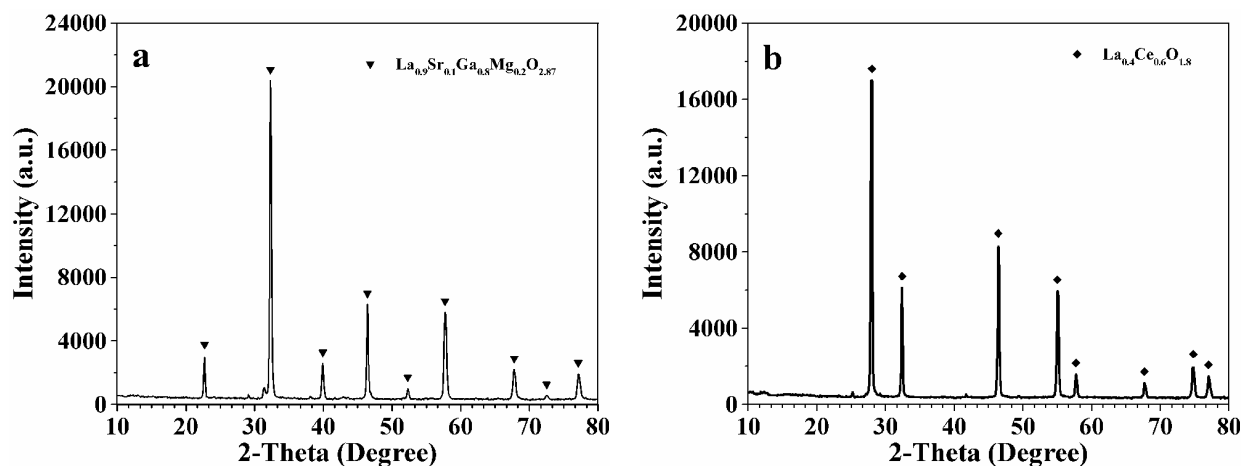


Figure 6.1 XRD patterns of (a) LSGM powder and (b) LDC powder prepared by solid-state reaction at 1250°C for 12hrs.

6.2.2 Cell Fabrication

The Ni-LDC anode-supported fuel cells were prepared as follows. Commercial NiO (Alfa) and the above-described LDC powder with weight ratio 3:2 were ball milled together for 24hrs in ethanol with 10wt% starch as pore former and 0.5wt% polyvinyl butyral (PVB) as binder. The milled powder mixture was dried and pressed into pellets with diameter of 19 mm and thickness of about 0.6 mm. The pellets were bisque fired at 1100°C for 4 hours. LDC and LSGM colloidal suspensions were prepared by mixing the powder with binder and dispersant in ethanol. Layers of LDC, LSGM, and LDC were colloiddally deposited sequentially on the anode support and the resulting green assembly was co-sintered at 1400°C for 4 hours. LDC and LSGM film thicknesses were controlled by the amount of colloidal solution applied onto the porous anode substrate. Cathodes consisting of a layer of 50wt% $\text{La}_{0.6}\text{Sr}_{0.4}\text{Fe}_{0.2}\text{Co}_{0.8}\text{O}_3$ (LSCF, Praxair) and 50wt% LSGM, followed by a pure LSCF layer, were applied on the electrolyte and fired at 1100°C for 1 hour.

6.2.3 Cell Testing

The gas tightness of the LDC-LSGM-LDC composite layer was characterized with a vacuum measurement apparatus as previously described [180]. A smooth dense plate was used as a gas-tight reference sample.

SOFC single-cell tests were carried out using a standard geometry [151]. The anodes were reduced in humidified hydrogen at 600°C for 12 hrs. Current-voltage curves were then taken from 550 to 750°C using an Electrochemical Workstation (IM6, ZAHNER), with the cathode exposed to ambient air and the anode to humidified (3% H₂O) hydrogen at a flow rate of 100 mL/min. The frequency range for the impedance measurement was 0.1Hz to 1MHz. The cell structure was observed after testing using scanning electron microscopy (SEM) in a Hitachi 3500 microscope.

6.3 Results and Discussion

Gas tightness measurements were carried out on the as-fired samples before application of the cathodes. Leakage was measured via the ultimate pressure achieved in a mechanically-pumped vacuum system with the SOFC sealed via a Viton o-ring. The SOFCs typically showed nearly the same ultimate steady pressure of the electrolyte membrane (50-100 mTorr) as that of the dense standard (50 mTorr). Previous measurements with YSZ thin electrolytes, that subsequently yielded near-ideal open circuit voltages during cell test, yielded similar results [180]. These results indicate that dense composite electrolyte layers were obtained with this method.

Figure 6.2 shows an example of a cross-sectional SEM image of the LDC/LSGM/LDC tri-layer along with the surrounding anode and cathode materials. The LDC and LSGM layers were uniform in thickness without cross-membrane pinholes or cracks and appeared to have only a small amount of porosity. There was good intimate contact between the LSGM and LDC layers and the surrounding electrodes, showing that the materials sintered well together. The LSGM layer was $\approx 9\mu\text{m}$ thick and the LDC layers were $\approx 7\text{-}10\mu\text{m}$ thick.

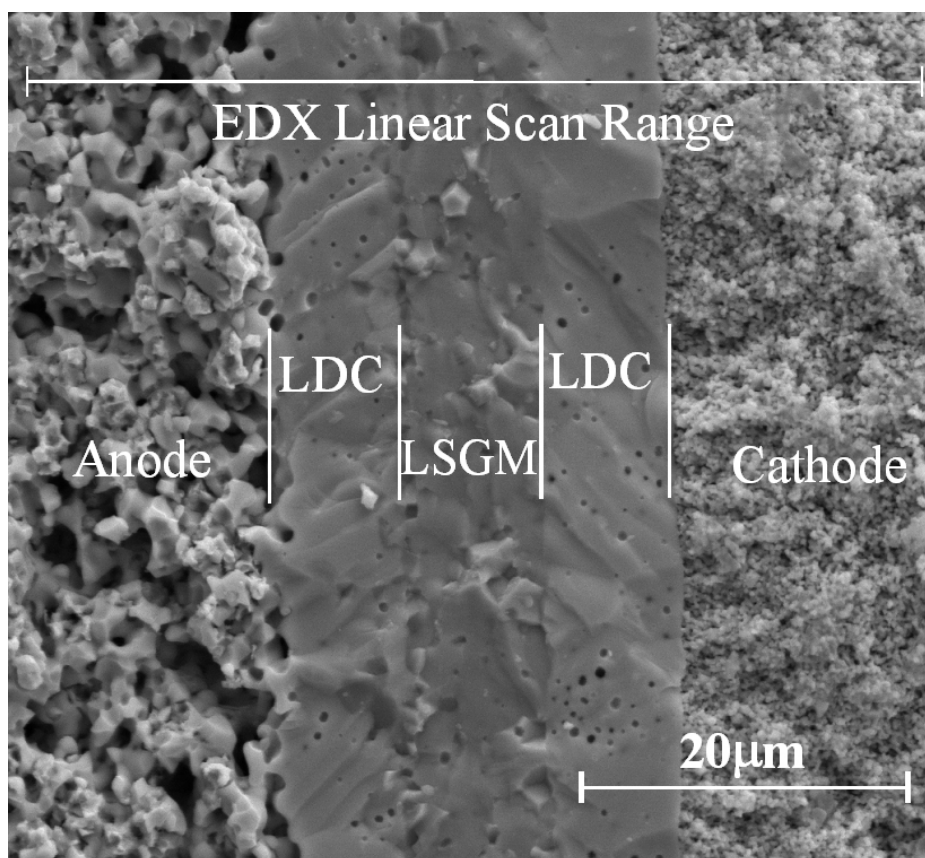


Figure 6.2 Cross-sectional SEM image of a typical LDC/LSGM/LDC electrolyte tri-layer and also showing portions of the Ni-LDC anode support and LSGM-LSCF/LSCF cathode.

Figure 6.3 illustrates typical cell performance. The peak power densities were 1.12, 0.91, 0.60, 0.33 and 0.17 W/cm^2 , at 750, 700, 650, 600 and 550 $^{\circ}\text{C}$, respectively. These power densities

are comparable to the best previously reported values for thick-film or electrolyte-supported LSGM SOFCs (e.g. 0.4-0.6 W/cm² at 700°C) [54,173-175]. In one case where much higher LSGM power densities were reported [176,177], LSGM and Sm-doped Ceria interlayers were deposited at relatively low temperature using pulsed laser deposition (avoiding possible reaction/diffusion problems), and the testing was done with pure oxygen at the cathode. The open circuit voltage (OCV) was 0.98V at 650°C, lower than that of a thick LSGM film single cell (above 1.1V) on H₂ and air [54]. This was presumably not due to gas leakage across the electrolyte, based on the relatively dense appearance of the layers (Figure 6.2), low measured gas leakage rates, and the observation that the OCV did not fluctuate with changes in gas flow rates. The low OCV can alternatively be explained by the diffusion of transition metal cations (e.g. Co, Fe, Ni) from electrodes into LSGM layer during sintering. Although low concentrations of transition metal cations in LSGM improves the oxide ion conductivity without the significantly decreasing the oxide-ion transference number [63,181], larger concentrations cause significant hole conduction and reduce OCV [182-184].

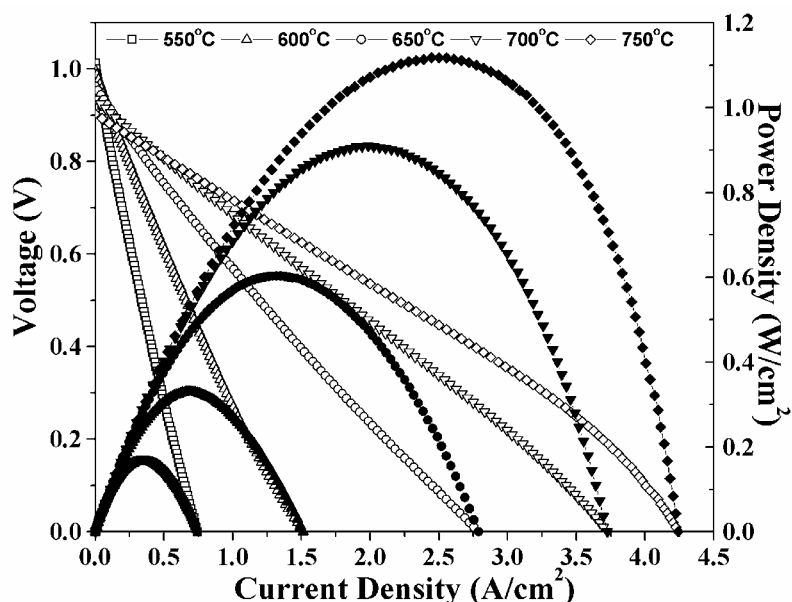


Figure 6.3 Voltage and power density vs. current density of a thin-LSGM SOFC operated on air and humidified hydrogen with a flow rate of 100 mL/min.

Figure 6.4 shows the results of EDX linear scans for transition elements (Co, Fe, Ni) across the cross sectional area shown in Fig. 6.2. It was observed that the LDC buffer layer between cathode and electrolyte successfully blocked the diffusion of Fe and Co cations from the cathode into the LSGM film, probably because of the relatively low cathode firing temperature. However, obvious Ni peaks were seen in the LSGM film, presumably due to diffusion during the prolonged high temperature co-firing. These results strongly suggest that the Ni-induced hole conduction resulted in the low OCV.

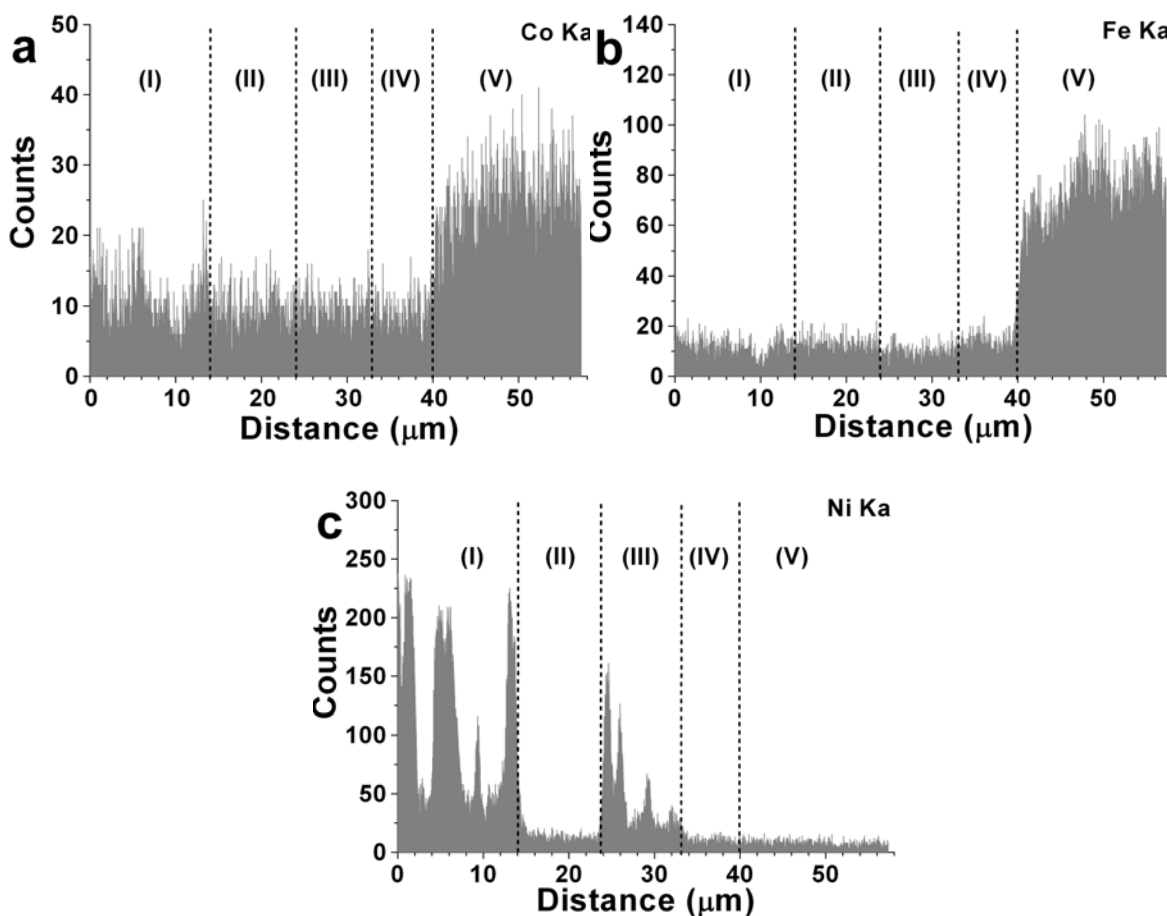


Figure 6.4 EDX linear scans of (a) Co, (b) Fe and (c) Ni peak intensities across the (I) Ni-LDC anode, (II) LDC buffer layer, (III) LSGM electrolyte, (IV) LDC buffer layer, and (V) LSCF-LSGM cathode.

Electrochemical impedance spectra from the cell in Figure 6.3 are shown in Figure 6.5. Figure 6.5 indicates that the ohmic electrolyte resistance contribution was comparable to that of the electrodes. The relatively low total resistance and good cell performance show that the LDC buffer layers successfully prohibited the formation of high resistance phases, e.g. $\text{LaSrGa}_3\text{O}_7$ due to La-depletion, or reaction products between LSGM and the electrodes, e.g. LaNiO_3 [54]. The high-frequency real-axis intercepts on Nyquist impedance plots give the total cell ohmic resistance R , which arises primarily from the electrolyte and interlayers (previous experience with this single cell test apparatus suggests that electrodes, contacts, and connecting wires were a relatively small contribution).

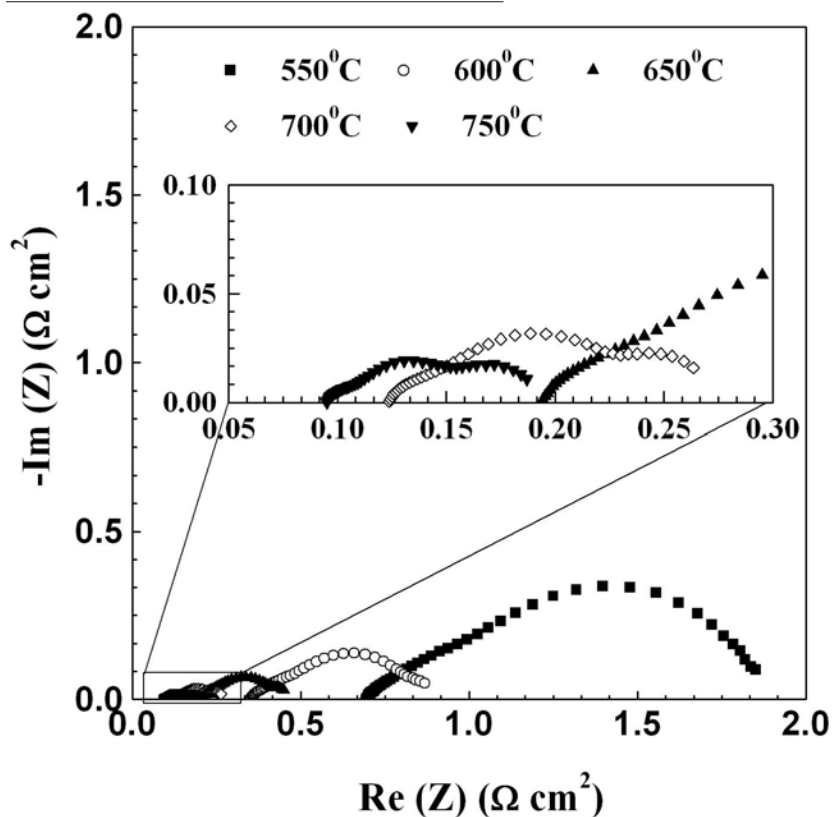


Figure 6.5 Electrochemical impedance spectra from a thin-LSGM SOFC measured at open-circuit potential in air and humidified hydrogen.

The total ohmic resistance values acquired from the impedance spectra are plotted versus temperature T in Figure 6.6, along with expected ohmic resistances for 10- μm -thick YSZ and LSGM calculated using reported conductivity values [172]. The measured electrolyte resistance was lower than expected for YSZ, but higher than expected for LSGM. The difference from the calculated LSGM electrolyte was clearly due to the LDC interlayers. Based on the difference between the measured composite electrolyte resistance and that of LSGM, we conclude that the resistivity of LDC was $\sim 63 \text{ } \Omega\text{cm}$ at 700°C . Resistivity values for such heavily doped LDC have not been reported to our knowledge. However, the ionic resistivity value of $\text{La}_{0.2}\text{Ce}_{0.8}\text{O}_{1.9}$ at 700°C was reported to be $\sim 24 \text{ } \Omega\text{cm}$ [185]. While this is lower than the present value for

$\text{La}_{0.4}\text{Ce}_{0.6}\text{O}_{1.8}$, the conductivity of doped ceria generally decreases with increasing dopant concentration over 20atm% (see Ref [186] for typical results for Sm-doped Ceria). The present value is thus consistent with prior conductivity data. Another conclusion from Figure 6.6 is that the good cell performance, compared to thin-YSZ electrolyte cells, was due to low polarization resistance rather than low electrolyte resistance. This may be attributed to a low polarization resistance for electrodes in contact with LDC versus YSZ [7].

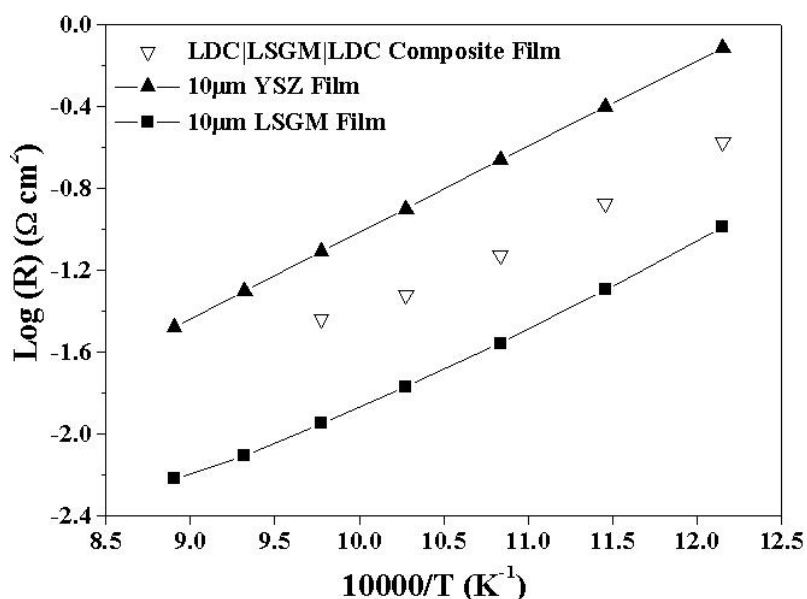


Figure 6.6 Total ohmic resistance R vs. $10000/T$ for a thin-LSGM SOFC. Shown for comparison are the calculated ohmic resistances of YSZ and LSGM thin films [172].

While the present results show that good LSGM-electrolyte anode-supported SOFCs can be made with co-firing, it is clear that the use of LDC inter-layers involves trade-offs. While the LDC minimizes reactions/interdiffusion between LSGM and the electrodes, it substantially increases the total resistance. Improvements will be needed in order to achieve lower electrolyte resistance, and hence, better low-temperature performance than YSZ electrolyte cells. It may be possible to reduce the cathode LDC layer thickness, since no Co or Fe were found in

the electrolyte. The LSGM layer thickness could also be decreased slightly to help reduce the electrolyte resistance. On the other hand, it will be difficult to reduce the anode LDC layer thickness because this would increase Ni diffusion into the LSGM layer, further reducing the OCV. An alternate approach would be to alter the LDC composition, e.g. by adding another dopant, in order to increase its conductivity closer to that for Sm-doped or Gd-doped Ceria [187,188]. Finally, a reduced co-firing temperature, but still high enough to achieve a dense LSGM electrolyte, may be useful to reduce Ni diffusion even for relatively thin inter-layers.

6.4 Summary and Conclusions

Anode-supported SOFCs with dense thin LDC/LSGM/LDC electrolytes were fabricated by co-sintering. Maximum power densities were $1.12\text{W}/\text{cm}^2$, $0.91\text{W}/\text{cm}^2$ and $0.60\text{W}/\text{cm}^2$ at 750°C , 700°C and 650°C , respectively. The good performance and low ohmic resistance suggests that there was no significant formation of interfacial phases. The results indicate a trade-off regarding the thicknesses of the LDC barrier layers: reducing the LDC thickness would be useful for reducing ohmic resistance but would also increase in-diffusion of impurities such as Ni into the LSGM electrolyte. The situation could be improved if co-firing temperatures and/or times could be reduced, or a more conductive barrier layer composition used. Finally, the impedance measurements show that improved electrodes are needed to achieve really good low-temperature performance.

CHAPTER SEVEN

**A Study of $\text{La}_{0.9}\text{Sr}_{0.1}\text{Ga}_{0.8}\text{Mg}_{0.2}\text{O}_{3-\delta}$ -
 $\text{La}_{0.6}\text{Sr}_{0.4}\text{Fe}_{0.8}\text{Co}_{0.2}\text{O}_{3-\delta}$ Composite Cathode for
Intermediate-Temperature Solid Oxide Fuel Cells**

Chapter 7: A Study of $\text{La}_{0.9}\text{Sr}_{0.1}\text{Ga}_{0.8}\text{Mg}_{0.2}\text{O}_{3-\delta}$ - $\text{La}_{0.6}\text{Sr}_{0.4}\text{Fe}_{0.8}\text{Co}_{0.2}\text{O}_{3-\delta}$ Composite Cathode for Intermediate-Temperature Solid Oxide Fuel Cells Electrolytes

7.1 Introduction

As an efficient energy converter, solid oxide fuel cells (SOFCs) have attracted much attention due to the fuel flexibility, tolerance to fuel impurities and potential of heat-power co-generation. Currently, the major development interest in SOFCs is focused on reducing the operating temperature into the intermediate range (600-700°C) without the penalty of power density. At this temperature range, low-cost stable interconnect and sealing materials can be adopted and there will be fewer problems with thermal management and degradation [8]. Previous studies have shown that the major limiting factor on the power densities at intermediate temperatures is from cathode polarization resistance, which can be substantially reduced by the adoption of composite cathode [189]. The composite cathode typically consists of an oxygen ion conductive material and an electronically or mixed conducting material. The electrochemical active sites, also known as triple-phase boundary (TPB), can be significantly increased and extended into the cathode by the dual phases [190,191]. The total polarization resistance of composite cathode is determined by the intrinsic properties of its components, such as oxygen ionic conductivity of the electrolyte materials, the electronic and catalytic properties of the electrocatalytic materials, also influenced by the microstructure and compositions, such as porosity, thickness, grain sizes, phase distribution.

Strontium and magnesium doped lanthanum gallate $(\text{La,Sr})(\text{Ga,Mg})\text{O}_{3-\delta}$ (LSGM), first reported as a fast oxide ion conductor by Ishihara *et al* in 1994 [55], exhibits several times higher

oxide ionic conductivity than YSZ. Therefore, LSGM is a good substitute for YSZ in the composite cathode for intermediate temperature operation. Strontium and iron doped lanthanum cobaltite (La,Sr)(Co,Fe)O_{3-δ} (LSCF), a mixed ionic-electronic conductor (MIEC), is a promising cathode material for intermediate temperature SOFCs (IT-SOFCs) due to its high electronic and ionic conductivity as well as its high catalytic activity for oxygen reduction [189].

In the present work, we explored the LSCF-LSGM composite cathode for IT-SOFCs. The compositional, microstructural, electrochemical and electrical measurements give the composition and preparation parameters for optimal cathode performance. Thin LSGM-electrolyte SOFCs was also fabricated to test the performance with the cathode.

7.2 Experimental Procedure

7.2.1 Fabrication of the Support Pellet

La_{0.9}Sr_{0.1}Ga_{0.8}Mg_{0.2}O_{3-δ} (LSGM) powder prepared with solid-state reaction as reported in Section 6.2.1 was die-pressed into pellets with diameter of 19 mm and thickness of about 0.5 mm under pressure of 20000 psi. The electrolyte pellets were sintered at 1450°C for 6 hours to achieve a dense structure.

7.2.2 Preparation of the Symmetrical Cell

La_{0.6}Sr_{0.4}Co_{0.2}Fe_{0.8}O_{3-δ} (LSCF, Praxair Inc.) powder was ball milled in ethanol with 30, 40, 50, 60 and 70wt% LSGM powder. Because the theoretical densities of LSGM (6.340g/cm³, JCPDF card # 70-2788) and LSCF (6.426g/cm³, JCPDF card # 89-5720) are very close to each other, the weight percentage of either phase can be taken as its volumetric ratio. In this study, the

composition ranges for LSGM and LSCF are chosen to be from 30 to 70wt%, which is within the percolation threshold for continuous pathway for both phases [8]. Nano-sized LSGM powder (Pechini method) from Ceramatec, Inc was also used in this study. Other than specifically indicated, LSGM-LSCF composite cathodes were made with solid-state reacted LSGM powder.

The milled powder mixture was dried, sieved with 120# mesh screen and made into ink with V-737 screen-printing vehicle (Heraeus) in a weight ratio of 50:50 by using a three-roll mill. The composite cathode paste was applied on both sides of the LSGM electrolyte pellets and fired at 1000-1300°C for 1 hour. Another layer of pure LSCF was applied on top of the composite cathode as a current collector layer, fired at 1000-1100°C for 1 hour. A current collector grid was applied on top of the cathodes with silver paste (DAD-87, Shanghai Research Institute of Synthetic Resin). The cell was mounted on an alumina tube with both sides exposed to ambient air. Silver wires were attached to the electrodes with two on each side for electrochemical characterization.

7.2.3 Electrochemical Characterization

The electrochemical tests were carried out by using a two-probe configuration under open circuit conditions, as shown in Fig 7.1. The electrochemical impedance spectra (EIS) of the symmetrical cells were taken with an Electrochemical Workstation (IM6, ZAHNER) from 550 to 800°C. The frequency range for the impedance measurement was 0.1Hz to 1MHz and the signal amplitude was 20mV. The cathode microstructure was observed after testing using scanning electron microscopy (SEM) in a Hitachi 3500 microscope. The electrical conductivities of the

composite cathodes were tested with van der Pauw method on samples with only LSGM-LSCF layer from 400 to 800°C.

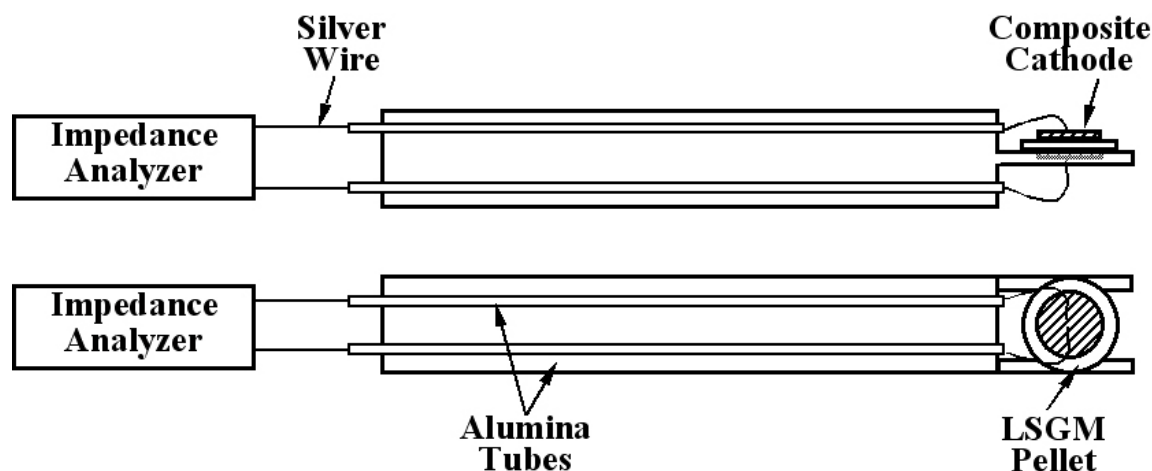


Figure 7.1 Schematic views of electrochemical impedance testing setup or symmetric cell EIS measurements. The upper one is a side view; lower one is a top view of the setup.

7.3 Results and Discussion

7.3.1 Chemical Compatibility of LSGM and LSCF

LSGM is chemically stable in a very narrow compositional region from the phase diagram [61]. Previous research has shown that resistive phases of LaSrGaO_3 and $\text{LaSrGa}_3\text{O}_7$ could result from the La enrichment or depletion in LSGM [54]. It is essential to ensure that the La chemical activity in LSCF is the same as that in LSGM to avoid low electrode performance from deleterious phases [54]. Figure 7.2 shows the XRD patterns of pure LSGM powder, pure LSCF powder, the mixture of 50wt% LSGM-50 wt% LSCF after ball milling, and the pellets from the mixture sintered at 1000-1200°C for 4 hours. Both LSCF and LSGM have perovskite structures. From the XRD patterns, no peaks corresponding to secondary phases (>3%) were detected. These results indicate that LSGM and LSCF are chemically compatible and no La-ion diffusion

happens during preparation processes. Although there might be diffusion of Co or Fe into LSGM [192], this doping would only introduce electronic conduction in LSGM other than resistive phases that decrease electrode performance [182-184].

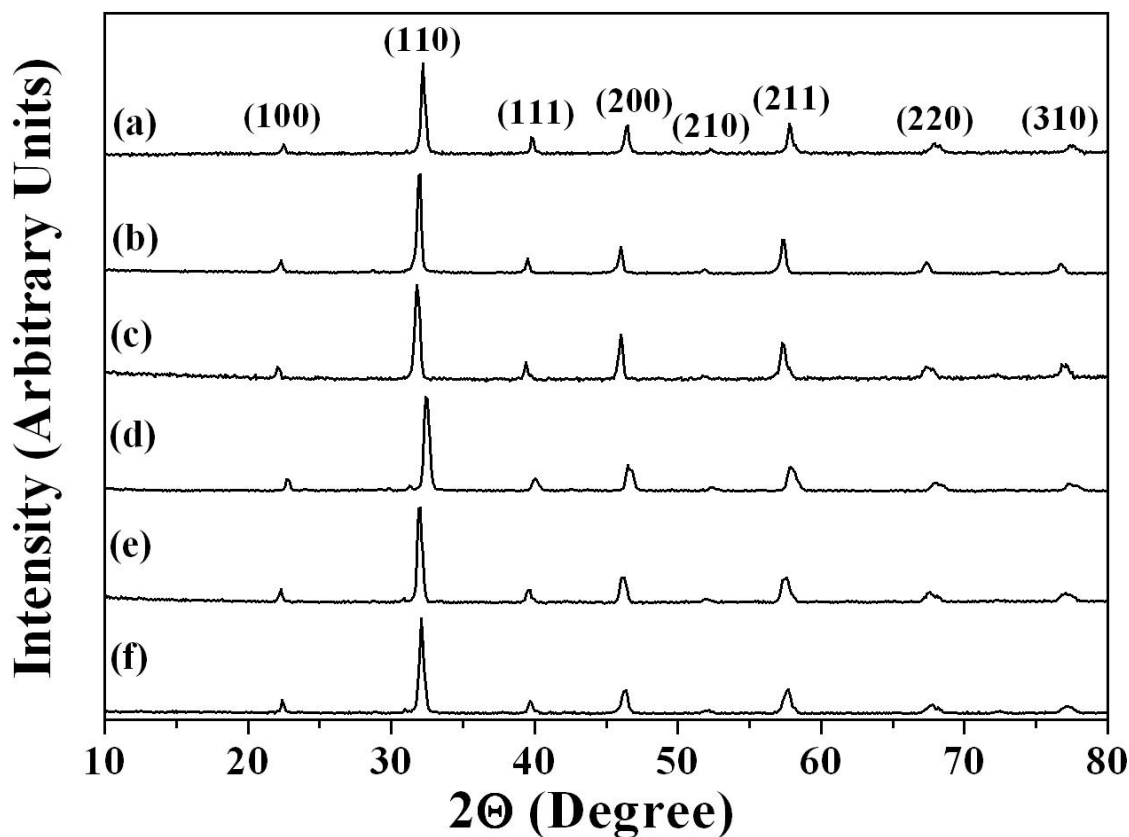


Figure 7.2 XRD patterns from (a) pure LSCF powder, (b) pure LSGM powder, mixture of LSCF and LSGM (50:50 wt%) (c) after ball milling, (d) after firing at 1000°C for 4 hours, (e) 1100°C for 4 hours, (f) 1200°C for 4 hours. All peaks correspond to those for the perovskite structure.

7.3.2 Effect of Sintering Temperature

Figure 7.3(a)-(d) show the morphologies of cross-sectional SEM images of the composite cathodes (50wt% LSGM-50wt% LSCF) sintered at 1000-1300°C respectively. The LSGM substrate is at the bottom. In Fig. 7.3(a), two distinct phases of LSGM particles of sub-micro size

and nano-size LSCF grains were presented in the composite cathode fired at 1000°C. The two components were not sintered well as indicated by poor mechanical strength, and the cathode was loosely bonded to the electrolyte pellet. At a temperature of 1100°C and above, the two phases were better sintered as indicated by better mechanical strength and good adhesion to the electrolyte. However, at elevated temperature of 1200°C and 1300°C, the cathodes showed larger grain sizes and less porosity, as shown in fig. 7.3(b)-(d).

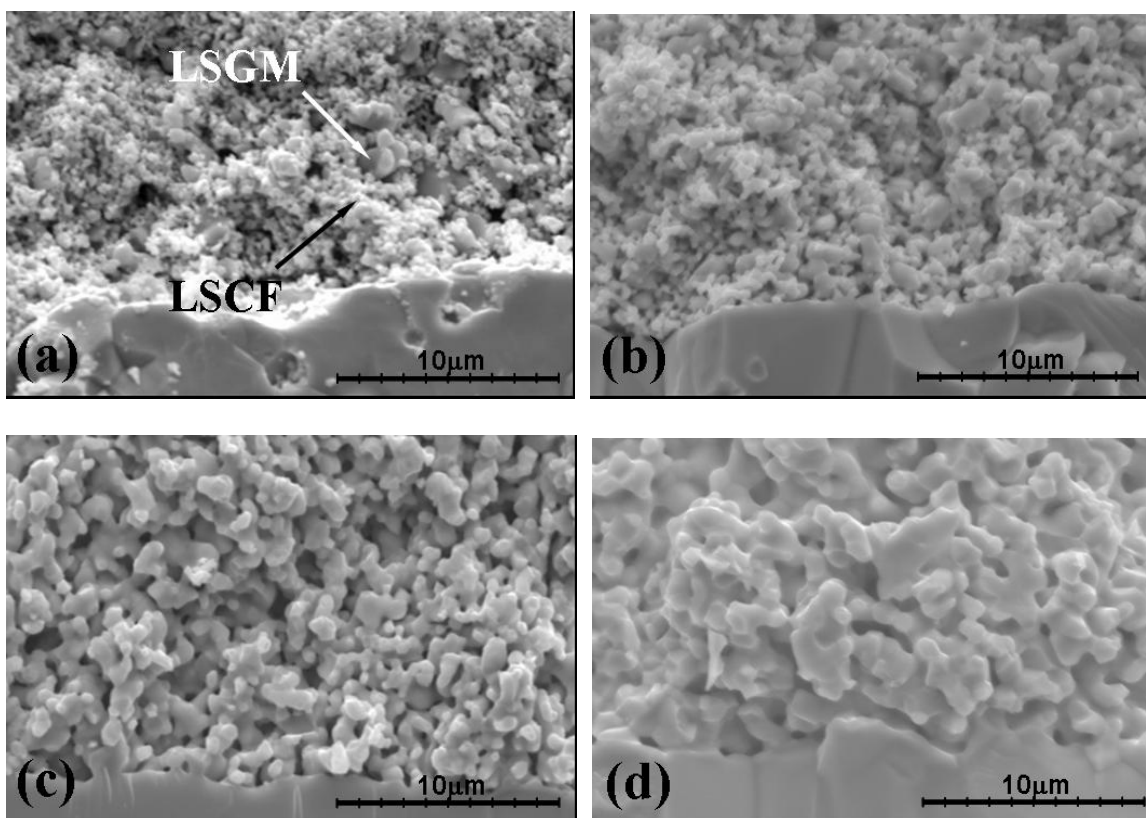


Figure 7.3 Cross-sectional SEM images of the composite cathodes (50wt% LSGM-50wt% LSCF) sintered at (a) 1000, (b) 1100, (c) 1200 and (d) 1300°C for 1 hours respectively with the LSGM substrate at the bottom.

Table 1 shows the total interfacial polarization area specific resistances, R_{AS} (*i.e.* the difference between the real axis intercepts of the impedance arcs) from electrochemical impedance

measurements for the cathodes sintered at temperatures. The cathode sintered at 1100°C showed the lowest R_{AS} in the intermediate temperature range (550-700°C). For a given electrode composition, the difference of total R_{AS} between samples sintered at various temperatures can be attributed to different mechanisms. Generally, larger grain sizes, less surface areas, and less porosity from high sintering temperatures tend to show higher R_{AS} due to the reduced triple-phase boundary (TPB) lengths [193], which are electrochemical active sites, and less gas diffusion channels. On the other side, the better connectivity between components (LSCF-LSGM, LSCF-LSCF, and LSGM-LSGM) at higher calcination temperatures can drive R_{AS} down. Collectively, the microstructural and electrochemical measurements gave the optimal sintering temperatures as 1100 to 1200°C.

Table 7.1 Summary of the total interfacial polarization resistances for the cathodes with 50wt% LSGM – 50wt% LSCF sintered at different temperatures. The electrochemical testing was taken at various temperatures from 550 to 800°C.

Temperature (°C)	Total Interfacial Polarization R_{AS} ($\Omega \cdot \text{cm}^2$)			
	$T_{\text{Sintering}}=1000^\circ\text{C}$	$T_{\text{Sintering}}=1100^\circ\text{C}$	$T_{\text{Sintering}}=1200^\circ\text{C}$	$T_{\text{Sintering}}=1300^\circ\text{C}$
550	4.6205	3.04773	3.11702	4.5541
600	0.90822	0.69045	0.6757	0.79302
650	0.24007	0.18723	0.18888	0.19555
700	0.07307	0.06085	0.0704	0.07325
750	0.02198	0.02454	0.02833	0.02853
800	0.00845	0.01203	0.01295	0.01459

7.3.3 Effect of Cathode Composition

Figure 7.4 illustrates the total R_{AS} for cathodes with different compositions tested in air at 600, 650 and 700°C. In general, the overall sizes of the impedance arcs were smaller for LSCF compositions from 40-60wt%. The lowest R_{AS} was found at 40wt%, *i.e.* 0.569, 0.181 and 0.0579 ($\Omega\cdot\text{cm}^2$) at 600, 650 and 700°C, respectively. However, at the same temperature, the impedance measurements showed no significant difference between samples with LSCF content from 40 to 60wt%. This suggests that the cathode composition was not the primary factor determining the electrochemical performance as long as similar contents of LSGM and LSCF were present. This is probably related to maximizing the TPB density and percolation of both phases.

Figure 7.5 shows the temperature dependence of the total interfacial polarization R_{AS} values for different LSCF-LSGM compositions. As discussed above, the R_{AS} values of different compositions are very close to each other, except for the case with 70wt% LSCF whose R_{AS} values are noticeably higher than others. However, the slopes of the $\log R_{AS}$ vs. $1/T$ data were nearly the same for all compositions, yielding an activation energy of 1.67 ± 0.04 eV. This value is nearly identical to that of LSCF-GDC composite cathode reported previously [189], and in reasonable agreement with previous studies of LSCF cathodes whose activation energies are around 1.5eV [194,195].

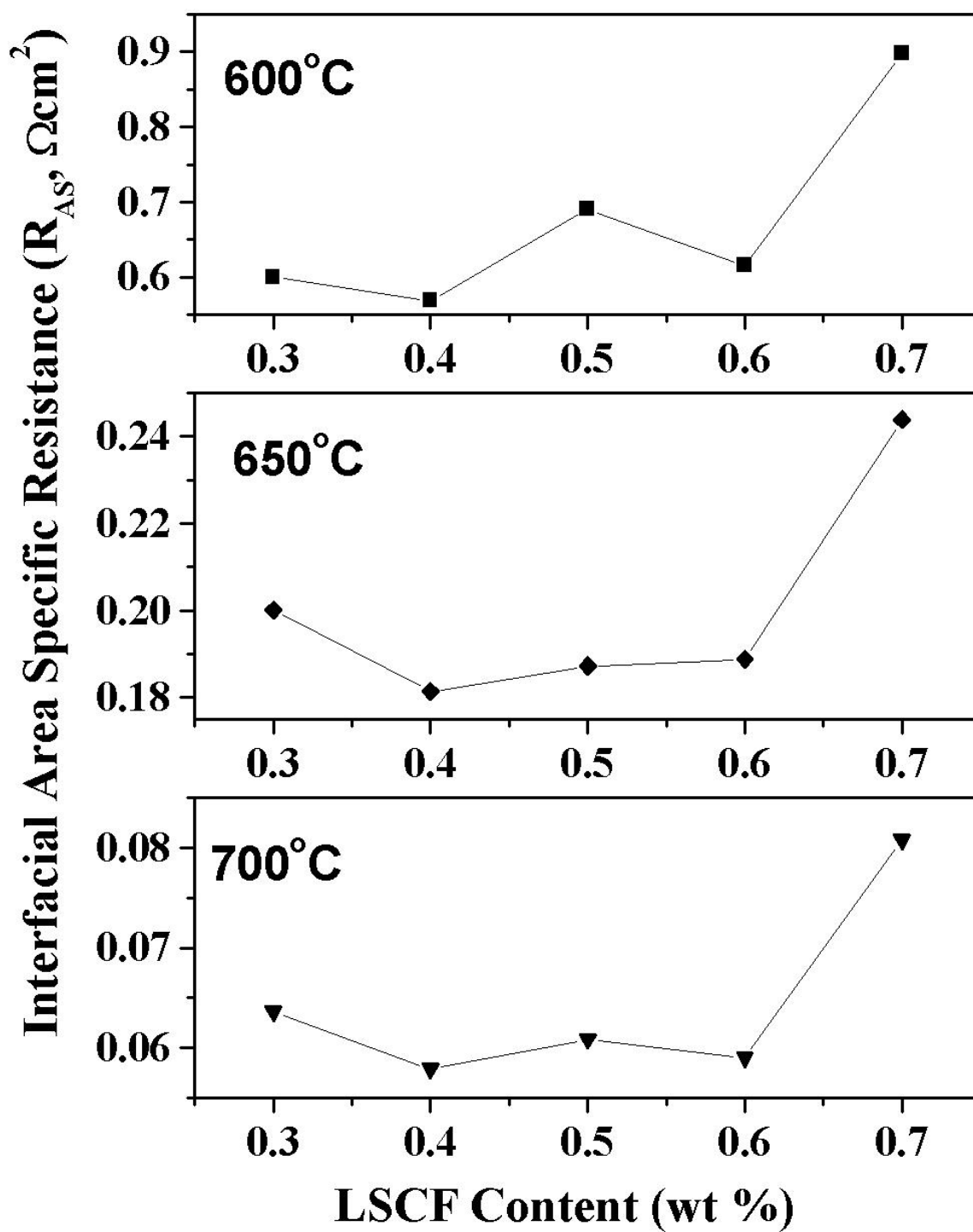


Figure 7.4 Total R_{AS} of composite cathodes as a function of LSCF content from 600 to 700°C.

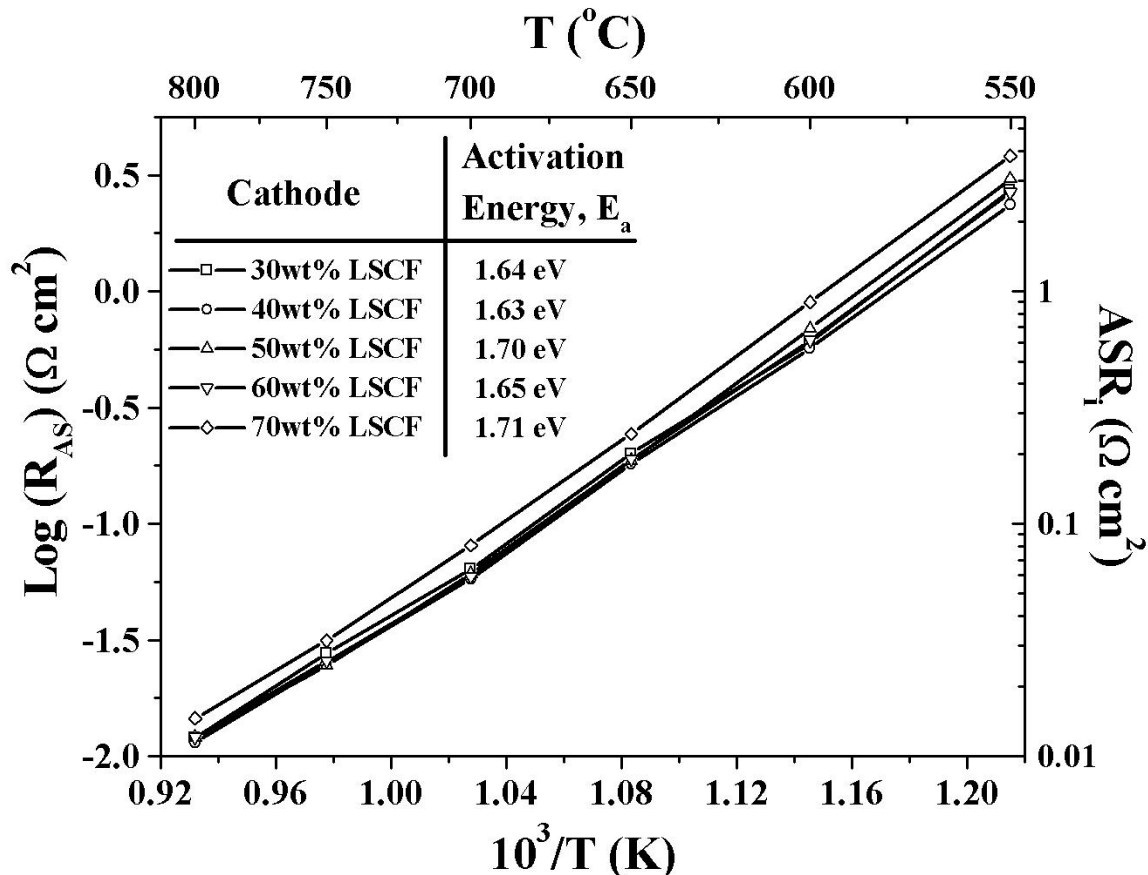


Figure 7.5 Temperature dependence of the total R_{AS} values for different LSCF-LSGM compositions measured over a temperature range of 550-800°C in air under open circuit condition.

It is important to assure that the cathode retains good conductivity despite the addition of LSGM to LSCF. To measure the electrical conductivities of the composite cathodes with different compositions, only composite layers were applied on one side of LSGM pellets without additional LSCF layers. Figure 7.6 plots the DC electrical conductivity of different cathodes tested with the van der Pauw methods [196] for temperatures from 400 to 800°C. Considering that the electrical conductivity from LSGM is low (0.10 S/cm at 800°C in air) [86], the major contribution to electrical conductivity is from the LSCF phase. At a given temperatures, higher

LSCF contents yield higher electrical conductivities, with the highest value of 34.6 S/cm at 800°C for 30wt% LSGM-70wt% LSCF. This trend may be attributed to the increase in the continuity of electronic conductive phase LSCF in the porous composite. Pure dense LSCF was reported to have high intrinsic electrical conductivity of 300-400 S/cm at 600°C for the composition in this study, *i.e.* $\text{La}_{0.6}\text{Sr}_{0.4}\text{Co}_{0.2}\text{Fe}_{0.8}\text{O}_{3-\delta}$ [86,197]. The measured conductivity values were about one to two orders of magnitude lower than the above reported values (27.7 S/cm for 30wt% LSGM-70wt% LSCF and 1.90 S/cm for 70wt% LSGM-30wt% LSCF at 600°C). We believe that this was mainly due to the dilution effect of LSGM, the porous structure of the composite plus the composition deviation of LSCF from the Co, Fe diffusion into LSGM lattice. For a given composition, the electrical conductivity increases with temperature, which has been explained by the temperature-dependant conduction mechanisms of LSCF [198]. The conductivity of a thin-film electrode (25 μm) with a current-collector layer (e.g. pure LSCF) should be $\geq 1\text{S/cm}$ for negligible performance loss ($R_{AS}=0.0025\Omega\text{cm}^2$) from ohmic resistance. At intermediate temperature range, this requires that the LSCF content should be over 40wt% for LSGM-LSCF composite cathodes. All of the components thus had sufficient conductivity.

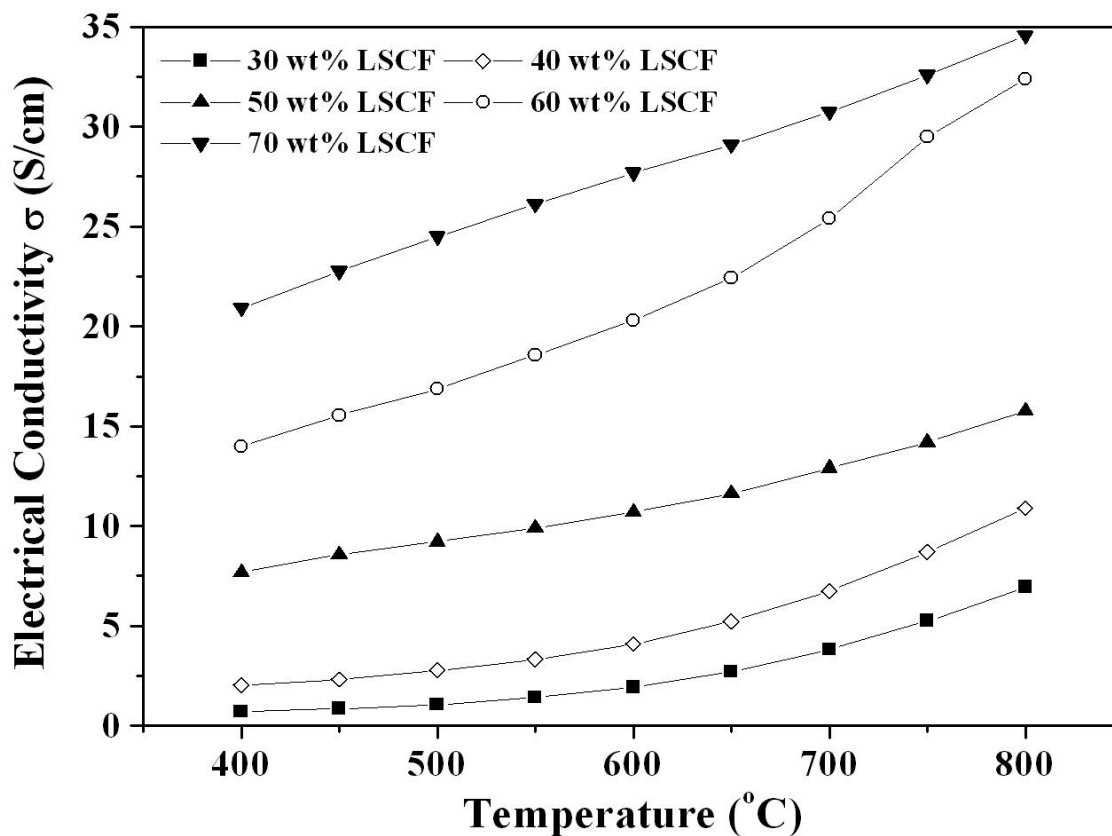


Figure 7.6 Plot of total conductivity versus temperatures for different cathode compositions.

7.3.4 Effect of Oxygen Partial Pressure

The oxygen partial pressure dependence of total R_{AS} values were measured at 600-800 $^{\circ}$ C over oxygen partial pressure of 0.01-1atm. Overall, a relatively weak oxygen partial pressure dependence for the cathodes with different compositions was observed, for example at 650 $^{\circ}$ C, $R_{AS} \propto (PO_2)^{-0.204 \pm 0.035}$, as shown in Figure 7.7. The usual form of $R_{AS} \propto (PO_2)^{-m}$, where $m=0 \sim 1/3$, and activation energy ≈ 1 eV, suggests that adsorption was the rate limiting mechanism for LSCF-LSGM cathodes [199], the same as for the composite cathodes systems reported

previously [189,200]. The weak PO_2 dependence indicates that the cathodes will work well in the down stream section of a SOFC stack, where oxygen in air is highly depleted.

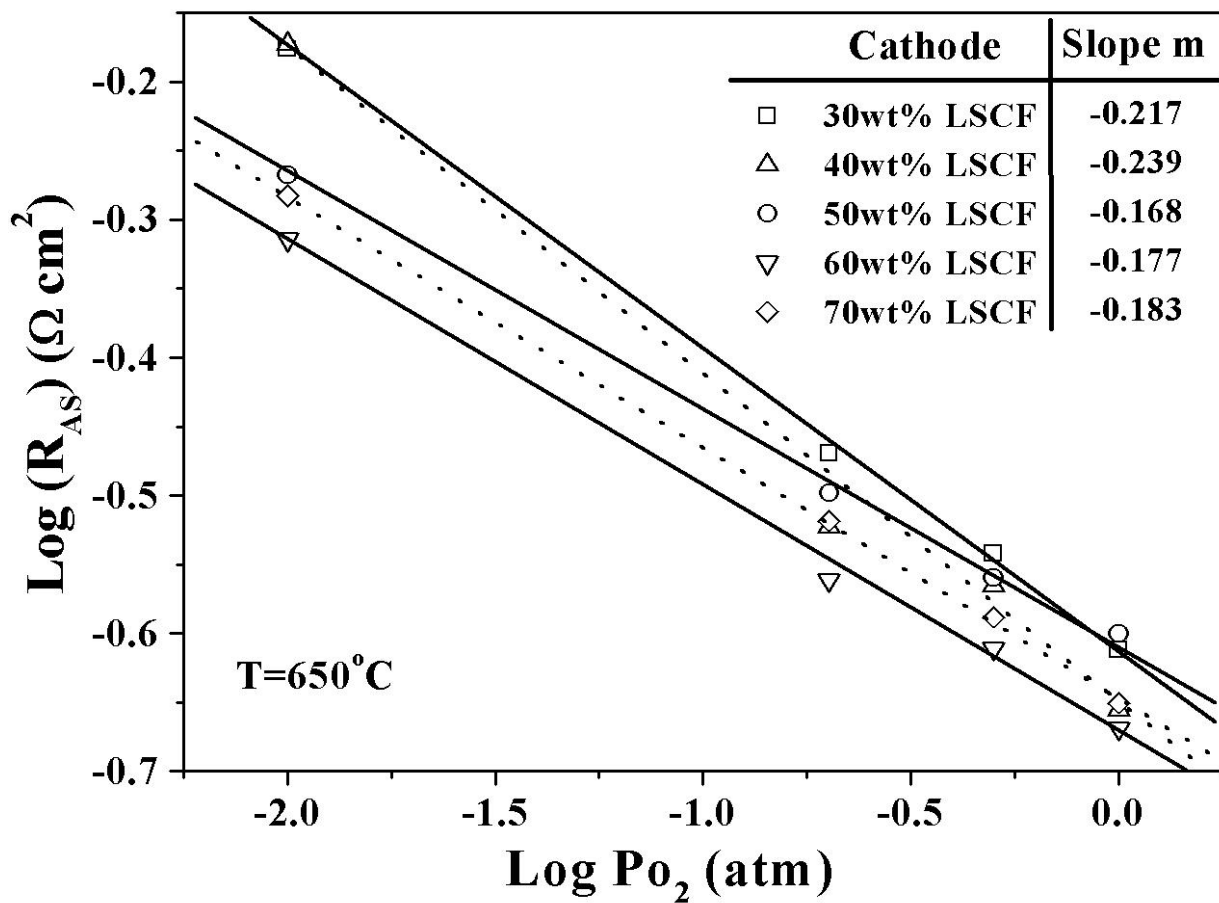


Figure 7.7 Total interfacial polarization resistance, R_{AS} , versus oxygen partial pressure for various LSCF-LSGM cathode compositions measured at 650°C .

7.3.5 Stability of LSCF-LSGM Composite Cathode

Figure 7.8 shows the R_{AS} of the cathode with 70 wt% LSCF- 30wt% LSGM under a constant current load of $0.5\text{A}/\text{cm}^2$ at 650°C in air. The hindrance of cathode degradation from sintering under a current load was reported by Jiang et al. for LSM in air [201], and it was attributed to the

elimination of the cation vacancies at the A-sites. The result demonstrates that good stability can be achieved with LSGM-LSCF cathodes operated under realistic conditions.

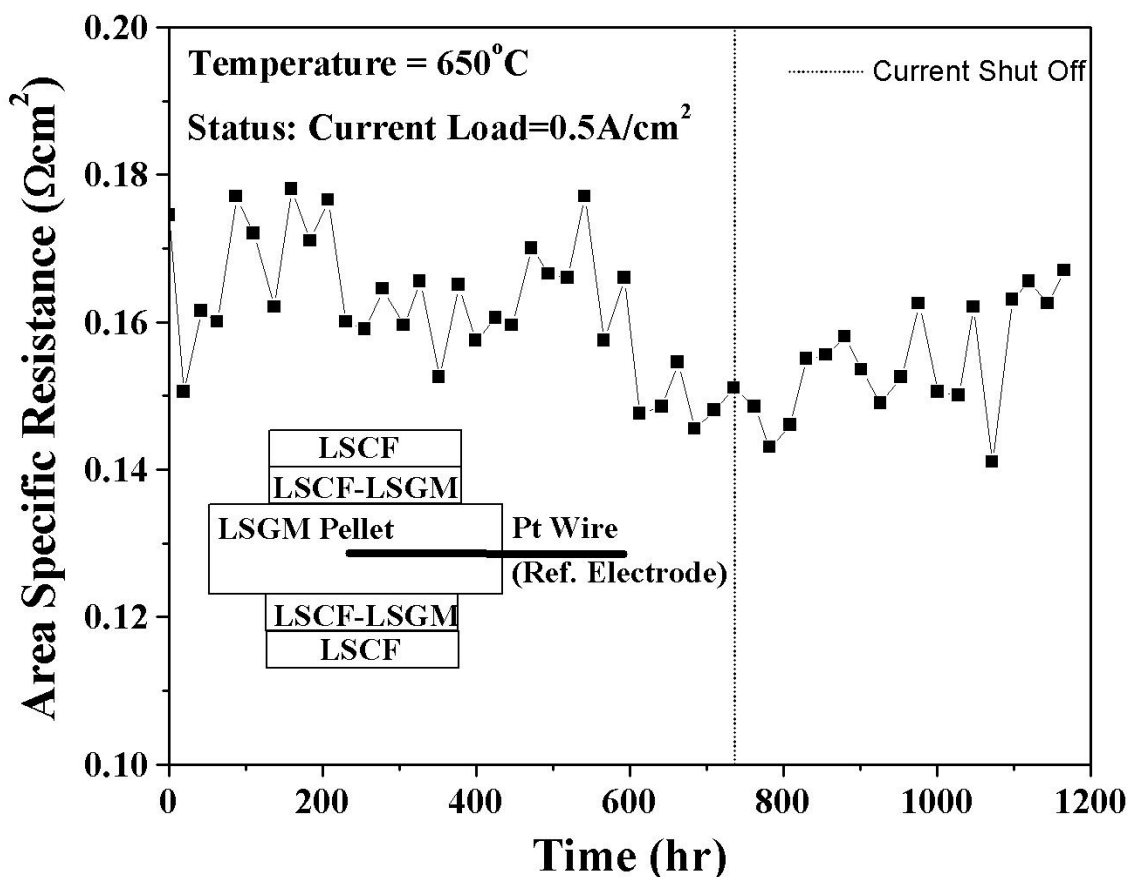


Figure 7.8 Long-term stability behavior of the cathode with 70 wt% LSCF- 30wt% LSGM under a constant current load of 0.5A/cm² at 650°C in air. The insert plot shows the symmetric cell under current load for the EIS measurements.

7.3.6 Cell Performance with LSCF-LSGM composite cathode

Anode-supported SOFCs with thin-film LSGM electrolyte were prepared by colloidal deposition. Figure 7.9 illustrates typical cell performance with 50/50 LSGM/LSCF composite cathode tested at different temperatures. The peak power densities were 1.09, 0.88, 0.57, 0.31

and 0.15 W/cm^2 , at 750, 700, 650, 600 and 550°C, respectively. The lower open circuit voltage (OCV), 0.98V at 650°C, was explained by the diffusion of transition metal cations (e.g. Co, Fe, Ni) from electrodes into LSGM layer during sintering [49]. This demonstrates that the present cathodes provide good performance in thin-LSGM electrolyte SOFCs.

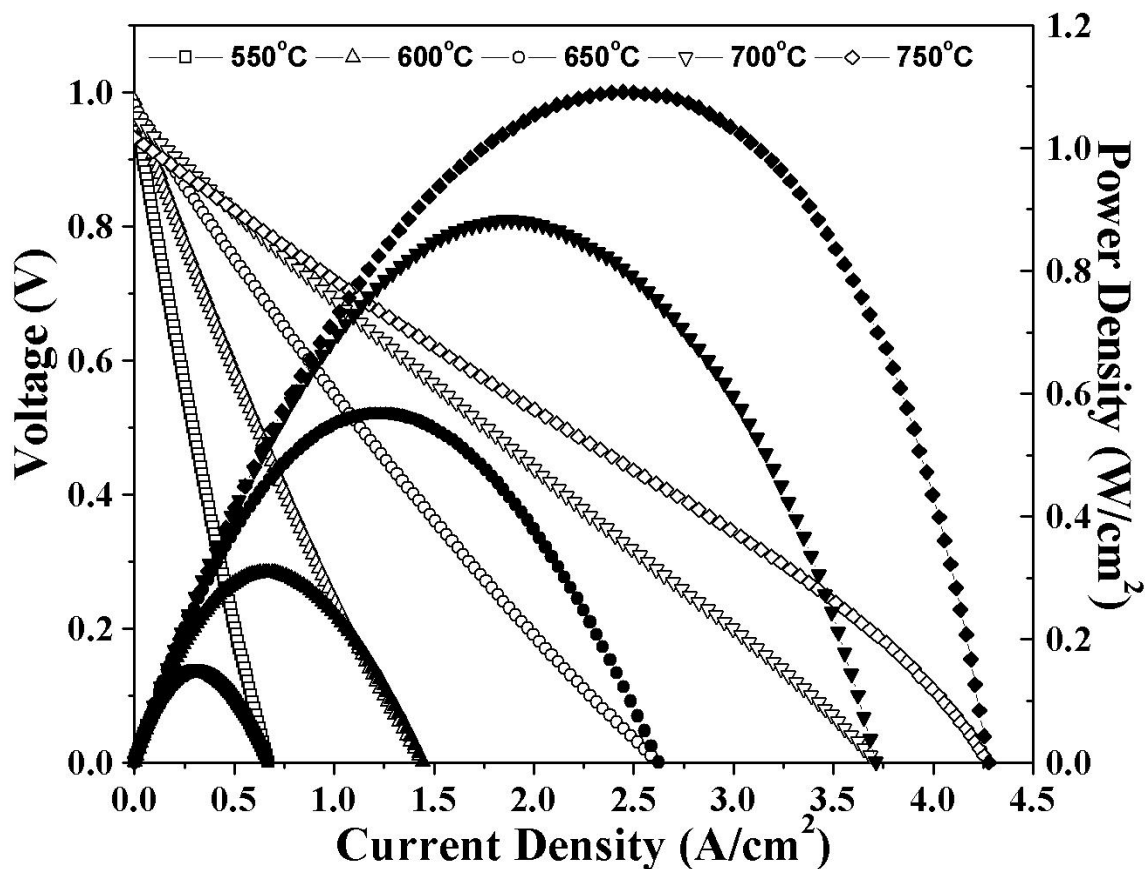


Figure 7.9 Voltage and power density vs. current density of a thin-film LSGM-electrolyte SOFC, with 50wt%LSCF-50wt% LSGM cathode, operated on air and humidified hydrogen with a flow rate of 100 mL/min.

7.4 Summary and Conclusions

LSCF-LSGM composite cathodes were investigated. The optimum sintering temperature was 1100°C. LSCF content between 40-60wt% gives the best electrochemical performance. The

oxygen partial pressure dependence of the composite cathodes is weak, which makes it suitable for stack applications. The composite cathode was stable under a certain current load but degraded at open circuit, which was attributed to the LSCF grain growth. Thin-film LSGM SOFCs with this composite cathode showed excellent performance at intermediate temperatures. Given that the cathode in this study is $\sim 20\mu\text{m}$ thick, the cell performance can be further improved with thicker cathode film around $40\mu\text{m}$.

CHAPTER EIGHT

Conclusions and Future Work

Chapter 8: Conclusions and Future Work

8.1 Conclusions

In this thesis, direct methane solid oxide fuel cells (SOFCs) and their related applications were investigated. The stable operation without coking was demonstrated by using current load, and further stability improvement was achieved by barrier layers. With stable direct methane operation, traditional Ni-YSZ SOFCs can also be used as an electrochemical partial oxidation (EPOx) reactor to generate synthesis gas and electricity from methane. LSGM-based electrolyte and cathode materials were shown to be promising for lowering the operation temperature of SOFCs without a performance penalty. Specific conclusions are listed as follows:

1. For traditional Ni-YSZ anode-support SOFCs, stable operation without coking was attained at high current density at $T \leq 700^\circ\text{C}$, except for very low current densities ($< 100\text{mA}/\text{cm}^2$). At higher temperatures ($750\text{--}800^\circ\text{C}$), increasingly large currents ($1.2\text{A}/\text{cm}^2$ and $1.8\text{ A}/\text{cm}^2$ for 750°C and 800°C , respectively) were required to avoid coking and cell failure. Mass spectrometer analysis of the effluents showed that H_2 and CO were the main reaction products, with H_2O and CO_2 minor products – all the products increased with increasing cell current density. The results suggest that coke-free SOFC operation was achieved due to kinetic limitations on the methane cracking reaction, particularly at low temperature. It is suggested that oxidation of hydrogen, produced by methane reforming by reaction products within the anode, is an important electrochemical reaction; the resulting steam helps remove solid C, thereby suppressing coking at high current densities.

2. At high temperatures of 750~800°C, the high current densities needed for stable operation on methane is not practical for the real stack operation. It was demonstrated that diffusion barrier layers increase the stable operating parameter range of Ni-YSZ anode-supported SOFCs operating directly with methane. At 800°C, for example, the current density needed for coke-free operation was reduced by a factor of 3. These results are consistent with the simple model wherein the diffusion barrier concentrated reaction products and reduced the methane concentration within the anode.
3. The achievement of coking-free operation on methane at high temperature over 750°C and relatively low current densities extended the applications of SOFCs from power generators to EPOx reactors. We have demonstrated that Ni-YSZ anode-supported SOFCs operated with pure methane fuel can produce both syngas and electricity without coking. The results show that SOFCs operated at $T \approx 750^\circ\text{C}$, $V \approx 0.4\text{V}$, and $\text{O}^{2-}/\text{CH}_4 \approx 1.2$ yield stable high electrical power output ($\sim 0.7\text{W}/\text{cm}^2$) and high syngas production rates ($\sim 20\text{ sccm}/\text{cm}^2$). Equilibrium calculations suggested that the EPOx reactor should be thermally self-sustaining under these conditions.
4. At the intermediate temperature range (600~700°C), the coking rate is significantly lower and cheap materials can be adopted for interconnector and sealing. However, traditional Ni-YSZ anode-supported SOFCs show poor performance due to the high resistance of YSZ electrolyte and high interfacial polarization of LSM-YSZ cathode. Anode-supported SOFCs with dense thin LDC/LSGM/LDC electrolytes were fabricated by co-sintering. Maximum power densities were $1.12\text{W}/\text{cm}^2$, $0.91\text{W}/\text{cm}^2$ and

0.60W/cm² at 750°C, 700°C and 650°C, respectively. The good performance and low ohmic resistance suggests that there was no significant formation of interfacial phases.

5. A LSGM-LSCF composite cathode was investigated for intermediate SOFCs. The optimum sintering temperature is 1100°C. LSCF content between 40-60wt% gives the best electrochemical performance. The oxygen partial pressure dependence of the composite cathodes is weak, which makes it suitable for stack applications. The composite cathode was stable under a given current for over 700 hours. Thin-film LSGM SOFCs with this composite cathode showed excellent performance at intermediate temperatures.

8.2 Future Work

For each section of this thesis, more work can be done to further our understanding of direct methane SOFCs:

1. The critical current densities for stable operation of real fuels like natural gas or propane on Ni-YSZ anode-supported SOFCs need to be determined. The higher hydrocarbons and sulfur contaminants in real fuels can significantly affect the stability of Ni-based SOFCs. Higher current densities may not be the solution for stable operation in these cases. Anodes with higher coking and sulfur resistance like ceramic anodes can be adopted for direct operation of real fuels.
2. The effects of structural properties of barrier layer such as thickness and porosity on the stability and performance of SOFCs can be determined to give the optimal structural parameters for the balancing between performance loss and coking-free operation.

3. Current EPOx reactor was demonstrated on single button cells. Tubular SOFCs have been proven to yield nearly complete conversion of methane to syngas. This was due to the long dwelling time of the fuel in the SOFC chamber. The methane conversion rate can be improved with modified reactor setup.
4. The thin-film LSGM-electrolyte SOFCs results indicate a trade-off regarding the thicknesses of the LDC barrier layers: reducing the LDC thickness would be useful for reducing ohmic resistance but would also increase in-diffusion of impurities such as Ni into the LSGM electrolyte. The situation could be improved if co-firing temperatures and/or times could be reduced, or a more conductive barrier layer composition used.
5. Given that the composite cathode of LSGM-LSCF in this study is of 10~20 μm thick, the cathode performance can be further improved with thicker films around 40 μm .

References

1. "<http://www.fuelcells.org/basics/apps.html>", (2000).
2. J. Liu and S.A. Barnett, "Operation of anode-supported solid oxide fuel cells on methane and natural gas", *Solid State Ionics*, **158** (1-2), p.11-16,(2003).
3. J. Liu, B.D. Madsen, Z. Ji, and S.A. Barnett, "A Fuel-Flexible Ceramic-Based Anode for Solid Oxide Fuel Cells ", *Electrochem. Solid-State Lett.*, **5** (6), p.A122-A124,(2002).
4. E.P. Murray, T. Tsai, and S.A. Barnett, "A direct-methane fuel cell with a ceria-based anode", *Nature*, **400** (6745), p.649-651,(1999).
5. S. Park, R. Craciun, J.M. Vohs, and R.J. Gorte, "Direct Oxidation of Hydrocarbons in a Solid Oxide Fuel Cell: I. Methane Oxidation", *J. Electrochem. Soc.*, **146** (10), p.3603-3605,(1999).
6. Y. Takeda, R. Kanno, M. Noda, Y. Tomida, and O. Yamamoto, "Cathodic Polarization Phenomena of Perovskite Oxide Electrodes with Stabilized Zirconia ", *J. Electrochem. Soc.*, **134**, p.2656-2661,(1987).
7. T. Tsai and S.A. Barnett, "Increased solid-oxide fuel cell power density using interfacial ceria layers", *Solid State Ionics*, **98** (3-4), p.191-196,(1997).
8. N.Q. Minh, "Ceramic Fuel Cells", *J. Am. Ceram. Soc.*, **76** (3), p.563-588,(1993).
9. W. Nernst, *Z. Elektrochem.*, **6**, p.41-43,(1937).
10. E. Baur and H. Preis, *Z. Elektrochem.*, **43**, p.727-732,(1937).
11. "http://www.eere.energy.gov/hydrogenandfuelcells/fuelcells/fc_types.html", U.S. Department of Energy, Energy Efficiency and Renewable Energy, "Hydrogen, Fuel Cells & Infrastructure Technologies Program", (2006).
12. B.d. Boer, "SOFC Anodes : Hydrogen oxidation at porous nickel and nickel/yttria-stabilised zirconia cermet electrodes", **Ph.D.**, (1998).
13. N.P. Brandon, S. Skinner, and B.C.H. Steele, "Recent Advances in Materials For Fuel Cells", *Annu. Rev. Mater. Res.*, **33**, p.183-213,(2003).

14. "<http://www.eia.doe.gov/emeu/international/reserves.html>", U.S. Department of Energy, Energy Information Administration, (2006).
15. "http://www.eia.doe.gov/oil_gas/natural_gas/analysis_publications/natbro/gasprices.htm", U.S. Department of Energy, Energy Information Administration, (2006).
16. R.F. Probst and R.E. Hicks, "Synthetic Fuels", Mc-Graw Hill, (1982).
17. U. Bossel, "Well-to-Wheel Studies, Heating Values and the Energy Conservation Principle", European Fuel Cell Forum Report, (2003).
18. G. Thomas, "Overview of Storage Development DOE Hydrogen Program", Livermore, CA. Sandia National Laboratories. DOE Hydrogen Program Review, San Ramon, CA (2000).
19. W. Zittel and R. Wurster, "Hydrogen in the Energy Sector. Chapter 2: Physical Properties", <http://www.hydrogen.org/Knowledge/w-i-energiew-eng2.html>, (2006).
20. S.Freni, G. Calogero, and S. Cavallaro, "Hydrogen production from methane through catalytic partial oxidation reactions", J. Power Sources, **87** (1-2), p.28-38,(2000).
21. A. Sacco, F.W.A.H. Geurts, G.A. Jablonski, S. Lee, and R.A. Gately, "Carbon deposition and filament growth on Fe, Co, and Ni foils using CH₄---H₂---H₂O---CO---CO₂ gas mixtures", J. Catalysis, **119** (2), p.322-341,(1989).
22. S.-I. Lee, S. McIntosh, J.M. Vohs, and R.J. Gorte. "Copper-plated stainless steel for bipolar plates in direct-oxidation SOFC". in *Solid Oxide Fuel Cells VIII*, S.C. Singhal and M. Dokiya Eds, The Electrochemical Society Proceedings Series: The Electrochemical Society: Pennington NJ, 2003 p.865-871.
23. J.R. Rostrup-Nielsen, *Catalytic Steam Reforming*. 5th ed. 1984, Berlin: Springer-Verlag.
24. Y.H. Hu and E. Ruckenstein, "Binary MgO-Based Solid Solution Catalysts for Methane Conversion to Syngas", Catal. Reviews, **44** (3), p.423 - 453,(2002).
25. D.L. Trimm, "Catalysts for the control of coking during steam reforming", Catalysis Today, **49** (1-3), p.3-10,(1999).
26. R.J. Farrauto and C.H. Bartholomew, *Fundamentals of Industrial Catalytic Processes*. 1st ed. 1997, Blackie Academic and Professional: London, p 351.
27. S.C. Tsang, J.B. Claridge, and M.L.H. Green, "Recent advances in the conversion of methane to synthesis gas", Catal. Today, **23** (1), p.3-15,(1995).

28. B.C.H. Steele, I. Kelly, H. Middleton, and R. Rudkin, "Oxidation of methane in solid state electrochemical reactors", *Solid State Ionics*, **28-30**, p.1547-1552,(1988).
29. J. Liu, B.D. Madsen, Z. Ji, and S.A. Barnett, "A Fuel-Flexible Ceramic-Based Anode for Solid Oxide Fuel Cells", *Electrochem. Solid-State Lett.*, **5** (6), p.A122-A124,(2002).
30. R.J. Gorte, H. Kim, and J.M. Vohs, "Novel SOFC anodes for the direct electrochemical oxidation of hydrocarbon", *J. Power Sources*, **106** (1-2), p.10-15,(2002).
31. S. Park, J.M. Vohs, and R.J. Gorte, "Direct oxidation of hydrocarbons in a solid-oxide fuel cell", *Nature*, **404**, p.265-267,(2000).
32. M. Mogensen and K. Kammer, "Conversion of Hydrocarbons in Solid Oxide Fuel Cells", *Annu. Rev. Mater. Res.*, **33**, p.321-331,(2003).
33. J.-H. Koh, Y.-S. Yoo, J.-W. Park, and H.C. Lim, "Carbon deposition and cell performance of Ni-YSZ anode support SOFC with methane fuel", *Solid State Ionics*, **149** (3-4), p.157-166,(2002).
34. O.A. Marina and M. Mogensen, "High-temperature conversion of methane on a composite gadolinia-doped ceria-gold electrode", *Applied Catalysis A: General*, **189** (1), p.117-126,(1999).
35. S. Katikaneni, C. Yuh, S. Abens, and M. Farooque, "The direct carbonate fuel cell technology: advances in multi-fuel processing and internal reforming", *Catalysis Today*, **77**, p.99-106,(2002).
36. C. Song, "Fuel processing for low-temperature and high-temperature fuel cells: Challenges, and opportunities for sustainable development in the 21st century", *Catalysis Today*, **77** (1-2), p.17-49,(2002).
37. J. Larminie and A.L. Dicks, *Fuel Cell Systems Explained*. 2000, New York: Wiley.
38. S.C. Singhal and K. Kendall, *High Temperature Solid Oxide Fuel Cells: Fundamentals, Design and Applications*. 2003, New York, Elsevier Inc.
39. A.D. McNaught and A. Wilkinson, *IUPAC Compendium of Chemical Terminology*. 2nd ed. 1997, Blackwell Science.
40. C.H. Hamann, A. Hamnett, and W. Vielstich, *Electrochemistry*. 1998, New York: J. Wiley & Sons.

41. J.O.M. Bockris and A.K.N. Reddy, *Modern Electrochemistry*. 1998, New York: Kluwer Academic-Plenum Press.
42. M. Suzuki, H. Sasaki, S. Ootoshi, A. Kajimura, and M. Ippommatsu, "High power density solid oxide electrolyte fuel cells using Ru/Y₂O₃ stabilized zirconia cermet anodes", *Solid State Ionics*, **62** (1-2), p.125-130,(1993).
43. H. Sasaki, M. Suzuki, S. Ootoshi, A. Kajimura, and M. Ippommatsu, "High-Power-Density-Solid-Oxide-Electrolyte Fuel Cells", *J. Electrochem. Soc.*, **139** (1), p.L12-L13,(1992).
44. R. Kikuchi, N. Koashi, T. Matsui, K. Eguchi, and T. Norby, "Novel anode materials for multi-fuel applicable solid oxide fuel cells", *Journal of Alloys and Compounds*, **408-412**, p.622-62,(2006).
45. S. McIntosh, J.M. Vohs, and R.J. Gorte, "Effect of Precious-Metal Dopants on SOFC Anodes for Direct Utilization of Hydrocarbons", *Electrochem. Solid-State Lett.*, **6** (11), p.A240-A243,(2003).
46. R.J. Gorte, J.M. Vohs, and S. McIntosh, "Recent developments on anodes for direct fuel utilization in SOFC", *Solid State Ionics*, **175** (1-4), p.1-6,(2004).
47. T.J. Armstrong and J.G. Rich, "Anode-supported solid oxide fuel cells with La_{0.6}Sr_{0.4}CoO_{3-lambda} - Zr_{0.84}Y_{0.16}O_{2-delta} composite cathodes fabricated by an infiltration method", *J. Electrochem. Soc.*, **153** (3), p.A515-A520,(2006).
48. F. Zhao, T.J. Armstrong, and A.V. Virkar, "Measurement of O₂-N₂ Effective Diffusivity in Porous Media at High Temperatures Using an Electrochemical Cell", *J. Electrochem. Soc.*, **150** (3), p.A249-A256,(2003).
49. Y. Lin and S.A. Barnett, "Co-firing of anode-supported SOFCs with thin La_{0.9}Sr_{0.1}Ga_{0.8}Mg_{0.2}O_{3-delta} electrolytes", *Electrochem. Solid-State Lett.*, **9** (6), p.A285-A288,(2006).
50. *Fuel Cell Handbook*. 6th ed. 2002: U.S. Department of Energy.
51. Y. Arachi, H. Sakai, O. Yamamoto, Y. Takeda, and N. Imanishai, "Electrical conductivity of the ZrO -Ln₂O₃ (Ln = Lanthanides) system", *Solid State Ionics*, **121** (1-4), p.133-139,(1999).
52. C.B. Choudhary, H.S. Maiti, and E.C. Subbarao, *Solid Electrolyte and Their Applications*. 1980, New York: Plenum Press. p. 1-80.

53. S.M. Haile, "Fuel cell materials and components ", *Acta Materialia*, **51** (19), p.5981-6000,(2003).
54. K. Huang, J.-H. Wan, and J.B. Goodenough, "Increasing Power Density of LSGM-Based Solid Oxide Fuel Cells Using New Anode Materials", *J. Electrochem. Soc.*, **148** (7), p.A788-A794,(2001).
55. T. Ishihara, H. Matsuda, and Y. Takita, "Doped LaGaO₃ Perovskite-Type Oxide as a New Oxide Ionic Conductor", *J. Am. Cer. Soc.*, **116** (9), p.3801-3803,(1994).
56. M. Feng and J.B. Goodenough, "A Superior Oxide-Ion Electrolyte", *Eur. J. Solid State Inorg. Chem.*, **31** (8-9), p.663-67,(1994).
57. M. O'Connell, A.K. Norman, C.F. Hüttermann, and M.A. Morris, "Catalytic oxidation over lanthanum-transition metal perovskite materials", *Catal. Today*, **47** (1-4), p.123-132,(1999).
58. T. Takahashi and H. Iwahara, "Ionic Conduction in Perovskite-Type Oxide Solid Solution and Its Application to Solid Electrolyte Fuel Cell", *Energy Conversion*, **11** (3), p.105,(1971).
59. Y. Ishihara, T. Ohmi, H. Hasegawa, T. Ikeda, T. Takasaki, S. Yamane, and R. Fukushima, "Electrical Conductivity Measurement in Liquified Hydrogen Chloride", *J. Electrochem. Soc.*, **141** (1), p.246-250,(1994).
60. T. Ishihara, H. Matsuda, and Y. Takita, "Effects of rare earth cations doped for La site on the oxide ionic conductivity of LaGaO₃-based perovskite type oxide", *Solid State Ionics*, **79**, p.147-151,(1995).
61. P.-N. Huang and A. Petric, "Superior Oxygen Ion Conductivity of Lanthanum Gallate Doped with Strontium and Magnesium", *J. Electrochem. Soc.*, **143** (5), p.1644-1648,(1996).
62. K. Huang, R. Tichy, J.B. Goodenough, and C. Milliken, "Superior Perovskite Oxide-Ion Conductor; Strontium- and Magnesium-Doped LaGaO₃: III, Performance Tests of Single Ceramic Fuel Cells", *J. Am. Cer. Soc.*, **81** (10), p.2581-2585,(1998).
63. T. Ishihara, H. Furutani, M. Honda, T. Yamada, T. Shibayama, T. Akbay, N. Sakai, H. Yokokawa, and Y. Takita, "Improved oxide ion conductivity in La_{0.8}Sr_{0.2}Ga_{0.8}Mg_{0.2}O₃ by doping Co", *Chem. Mater.*, **11** (8), p.2081-2088,(1999).
64. T. Ishihara, T. Akbay, H. Furutani, and Y. Takita, "Improved oxide ion conductivity of Co doped La_{0.8}Sr_{0.2}Ga_{0.8}Mg_{0.2}O₃ perovskite type oxide", *Solid State Ionics*, **113-115**, p.585-591,(1998).

65. *Handbook of Fuel Cell, Fundamentals Technology and Applications, Volume 4*, ed. W. Vielstich, A. Lamm, and H.A. Gasteiger. 2003, West Sussex: John Wiley & Sons Ltd. p. 1112.
66. J. Drennan, V. Zelizko, D. Hay, F.T. Ciacchi, S. Rajendran, and S.P.S. Badwal, "Characterisation, conductivity and mechanical properties of the oxygen-ion conductor $\text{La}_{0.9}\text{Sr}_{0.1}\text{Ga}_{0.8}\text{Mg}_{0.2}\text{O}_{3-x}$ ", *J. Mater. Chem.*, **7** (1), p.79-85,(1997).
67. Y. Du and N.M. Sammes, "Fabrication of tubular electrolytes for solid oxide fuel cells using strontium- and magnesium-doped LaGaO_3 materials", *J. Eur. Ceram. Soc.*, **21** (6), p.727-735,(2001).
68. I. Yasuda, Y. Matsuzaki, T. Yamakawa, and T. Koyama, "Electrical conductivity and mechanical properties of alumina-dispersed doped lanthanum gallates", *Solid State Ionics*, **135** (1-4), p.381-388,(2000).
69. A.V. Berenov, J.L. MacManus-Driscoll, and J.A. Kilner, "Oxygen tracer diffusion in undoped lanthanum manganites", *Solid State Ionics*, **122** (1-4), p.41-49,(1999).
70. C.Brugnoni, U. Ducati, and M. Scagliotti, "SOFC cathode/electrolyte interface. Part I: Reactivity between $\text{La}_{0.85}\text{Sr}_{0.15}\text{MnO}_3$ and $\text{ZrO}_2\text{-Y}_2\text{O}_3$ ", *Solid State Ionics*, **76** (3-4), p.177-182,(1995).
71. S.J. Skinner, "Recent advances in Perovskite-type materials for solid oxide fuel cell cathodes", *Intl. J. Inorg. Mater.*, **3** (2), p.113-121,(2001).
72. O. Yamamoto, Y. Takeda, R. Kanno, and M. Noda, "Perovskite-type oxides as oxygen electrodes for high temperature oxide fuel cells", *Solid State Ionics*, **22** (2-3), p.241-246,(1987).
73. H. Yokokawa, N. Sakai, T. Kawada, and M. Dokiya, "Thermodynamic analysis on interface between perovskite electrode and YSZ electrolyte", *Solid State Ionics*, **40-41** (1), p.398-401,(1990).
74. M. Suzuki, H. Sasaki, S. Otsu, A. Kajimura, N. Sugiura, and M. Ippommatsu, "High Performance Solid Oxide Fuel Cell Cathode Fabricated by Electrochemical Vapor Deposition", *J. Electrochem. Soc.*, **141** (7), p.1928-1931,(1994).
75. H. Takeuchi, H. Nishiyama, A. Ueno, S. Aikawa, M. Aizawa, H. Tajiri, T. Nakayama, S. Suehiro, and K. Shukuri. "Current Status of SOFC Development by Wet Process". in *Solid Oxide Fuel Cells VI*, S.C. Singhal and M. Dokiya Eds, The Electrochemical Society Proceedings: The Electrochemical Society, Pennington, NJ, 1999 p.879-884.

76. M. Dokiya, N. Sakai, T. Kawada, H. Yokokawa, T. Iwata, and M. Mori. *Solid Oxide Fuel Cells I*, S.C. Singhal Eds, The Electrochemical Society Proceedings: The Electrochemical Society, Pennington, NJ., 1989 p.325-336.
77. M. Mori and Y. Hiei. "Thermal Expansion Behavior of Ca-, or Sr-Doped Lanthanum Manganites under Oxidizing Atmospheres". in *Solid Oxide Fuel Cells VI*, S.C. Singhal and M. Dokiya Eds, The Electrochemical Society Proceedings: The Electrochemical Society, Pennington, NJ, 1999 p.347-354.
78. Y. Sakaki, Y. Takeda, A. Kato, N. Imanishi, O. Yamamoto, M. Hattori, M. Iio, and Y. Esaki, " $\text{Ln}_{1-x}\text{Sr}_x\text{MnO}_3$ (Ln=Pr, Nd, Sm and Gd) as the cathode material for solid oxide fuel cells", *Solid State Ionics*, **118** (3-4), p.187-194,(1999).
79. S.T. Aruna, M. Muthuraman, and K.C. Patil, "Studies on strontium substituted rare earth manganites", *Solid State Ionics*, **120** (1-4), p.275-280,(1999).
80. T.-L. Wen, H. Tu, Z. Xu, and O. Yamamoto, "A study of (Pr, Nd, Sm) $_{1-x}\text{Sr}_x\text{MnO}_3$ cathode materials for solid oxide fuel cell", *Solid State Ionics*, **121** (1-4), p.25-30,(1999).
81. G.C. Kostogloudis and C. Ftikos, "Characterization of $\text{Nd}_{1-x}\text{Sr}_x\text{MnO}_{3\pm\delta}$ SOFC cathode materials", *J. Eur. Ceram. Soc.*, **19** (4), p.497-505,(1999).
82. M.B. Phillipps, N.M. Sammes, and O. Yamamoto, " $\text{Gd}_{1-x}\text{A}_x\text{Co}_{1-y}\text{Mn}_y\text{O}_3$ (A=Sr, Ca) as a cathode for the SOFC", *Solid State Ionics*, **123** (1-4), p.131-138,(1999).
83. T. Ishihara, T. Kudo, H. Matsuda, and Y. Takita, "Doped PrMnO_3 Perovskite Oxide as a New Cathode of Solid Oxide Fuel Cells for Low Temperature Operation ", *J. Electrochem. Soc.*, **142** (5), p.1519-1524,(1995).
84. Y. Ohno, S. Nagata, and H. Sato, "Properties of oxides for high temperature solid electrolyte fuel cell", *Solid State Ionics*, **9-10** (2), p.1001-1007,(1983).
85. B.C.H. Steele, "Appraisal of $\text{Ce}_{1-y}\text{Gd}_y\text{O}_{2-y/2}$ electrolytes for IT-SOFC operation at 500°C", *Solid State Ionics*, **129** (1-4), p.95-110,(2000).
86. H. Ullmann, N. Trofimenko, F. Tietz, D. Stöver, and A. Ahmad-Khanlou, "Correlation between thermal expansion and oxide ion transport in mixed conducting perovskite-type oxides for SOFC", *Solid State Ionics*, **138** (1-2), p.79-90,(2000).
87. Z. Shao and S.M. Haile, "A high-performance cathode for the next generation of solid-oxide fuel cell", *Nature*, **431**, p.170-173,(2004).
88. W.Z. Zhu and S.C. Deevi, "A review on the status of anode materials for solid oxide fuel cells", *Mat. Sci. Engr. A*, **362** (1-2), p.228-239,(2003).

89. D.W. Dees, T.D. Claar, T.E. Easler, D.C. Fee, and F.C. Mrazek, "Conductivity of Porous Ni/ZrO₂-Y₂O₃ Cermets ", J. Electrochem. Soc., **134** (9), p.2141-2146,(1987).
90. S.K. Pratihari, R.N. Basu, S. Mazumder, and H.S. Maiti. "Electrical Conductivity and Microstructure of Ni-YSZ Anode Prepared by Liquid Dispersion Method". in *Solid Oxide Fuel Cells VI*, S.C. Singhal and M. Dokiya Eds, The Electrochemical Society Proceedings Series: The Electrochemical Society: Pennington NJ, 1999 p.513-521.
91. T. Iwata, "Characterization of Ni-YSZ Anode Degradation for Substrate-Type Solid Oxide Fuel Cells", J. Electrochem. Soc., **143** (5), p.1521-1525,(1996).
92. H. Itoh, T. Yamamoto, M. Mori, T. Horita, N. Sakai, H. Yokokawa, and M. Dokiya, "Configurational and Electrical Behavior of Ni-YSZ Cermet with Novel Microstructure for Solid Oxide Fuel Cell Anodes", J. Electrochem. Soc., **144** (2), p.641-646,(1997).
93. S. Primdahl and M. Mogensen, "Oxidation of Hydrogen on Ni/Yttria-Stabilized Zirconia Cermet Anodes", J. Electrochem. Soc., **144** (10), p.3409-3419,(1997).
94. S. Primdahl and M. Mogensen, "Gas Conversion Impedance: A Test Geometry Effect in Characterization of Solid Oxide Fuel Cell Anodes", J. Electrochem. Soc., **145** (7), p.2431-2438,(1998).
95. N. Nakagawa, H. Sakurai, K. Kondo, T. Morimoto, K. Hatanaka, and K. Kato, "Evaluation of the Effective Reaction Zone at Ni(NiO)/Zirconia Anode by Using an Electrode with a Novel Structure", J. Electrochem. Soc., **142** (10), p.3474-3479,(1995).
96. T. Inoue, K. Eguchi, T. Setoguchi, and H. Arai, "Cathode and anode materials and the reaction kinetics for the solid oxide fuel cell", Solid State Ionics, **40-41** (1), p.407-410,(1990).
97. J.-H. Lee, H. Moon, H.-W. Lee, J. Kim, J.-D. Kim, and K.-H. Yoon, "Quantitative analysis of microstructure and its related electrical property of SOFC anode, Ni-YSZ cermet", Solid State Ionics, **148** (1-2), p.15-26,(2002).
98. W. Huebner, D.M. Reed, and H.U. Anderson. "Solid Oxide Fuel Cell Performance Studies: Anode Development". in *Solid Oxide Fuel Cells VI*, S.C. Singhal and M. Dokiya Eds, The Electrochemical Society Proceedings: The Electrochemical Society, Pennington, NJ, 1999 p.503-512.
99. J.-H. Lee, J.-W. Heo, D.-S. Lee, J. Kim, G.-H. Kim, H.-W. Lee, H.S. Song, and J.-H. Moon, "The impact of anode microstructure on the power generating characteristics of SOFC", J. Electrochem. Soc., **158** (3-4), p.225-232,(2003).

100. D. Simwonis, F. Tietz, and D. Stöver, "Nickel coarsening in annealed Ni/8YSZ anode substrates for solid oxide fuel cells", *Solid State Ionics*, **132** (3-4), p.241-251,(2000).
101. A. Tsoga and P. Nikolopoulos. "Additives for improved long-term behavior of the SOFC anode cermet". in *Solid Oxide Fuel Cells V*, U. Stimming, S.C. Singhal, H. Tagawa, and W. Lehnert Eds, The Electrochemical Society Proceedings Series: The Electrochemical Society: Pennington NJ, 1997 p.823-832.
102. S.d. Souza, S.J. Visco, and L.C.D. Jonghe, "Thin-film solid oxide fuel cell with high performance at low-temperature", *Solid State Ionics*, **98** (1-2), p.57-61,(1997).
103. J.-W. Kim, A.V. Virkar, K.-Z. Fung, K. Mehta, and S.C. Singhal, "Polarization Effects in Intermediate Temperature, Anode-Supported Solid Oxide Fuel Cells", *J. Electrochem. Soc.*, **146** (1), p.69-78,(1999).
104. C.M. Finnerty and R.M. Ormerod. "Internal Reforming and Electrochemical Performance Studies of Doped Nickle/Zirconia Anodes in SOFCs Running on Methane". in *Solid Oxide Fuel Cells VI*, S.C. Singhal and M. Dokiya Eds, The Electrochemical Society Proceedings: The Electrochemical Society, Pennington, NJ, 1999 p.583-592.
105. M. Itome and A.E. Nelson, "Methane oxidation over M-8YSZ and M-CeO₂/8YSZ (M = Ni, Cu, Co, Ag) catalysts", *Catal. Lett.*, **106** (1-2), p.21-27,(2006).
106. Y. Nabae, I. Yamanaka, S. Takenaka, M. Hatano, and K. Otsuka, "Direct Oxidation of Methane by Pd-Ni Bimetallic Catalyst over Lanthanum Chromite Based Anode for SOFC", *Chem. Lett.*, **34** (6), p.774-775,(2005).
107. S. McIntosh, J.M. Vohs, and Raymond J. Gorte, "Effect of Precious-Metal Dopants on SOFC Anodes for Direct Utilization of Hydrocarbons", *Electrochem. Solid-State Lett.*, **6** (11), p.A240-A243,(2003).
108. T. Bunluesin, R.J. Gorte, and G.W. Graham, "Studies of the water-gas-shift reaction on ceria-supported Pt, Pd, and Rh: Implications for oxygen-storage properties", *Applied Catalysis B: Environmental*, **15** (1-2), p.107-114,(1998).
109. S. Sharma, S. Hilaire, J.M. Vohs, R.J. Gorte, and H.-W. Jen, "Evidence for Oxidation of Ceria by CO₂", *J. Catalysis*, **190** (1), p.199-204,(2000).
110. A. Atkinson, S. Barnett, R.J. Gorte, J.T.S. Irvine, A.J. McEvoy, M. Mogensen, S.C. Singhal, and J. Vohs, "Advanced anodes for high-temperature fuel cells", *Nature Materials*, **3**, p.17-27,(2004).

111. H. Uchida, H. Suzuki, and M. Watanabe, "High-Performance Electrode for Medium-Temperature Solid Oxide Fuel Cells", *J. Electrochem. Soc.*, **145** (2), p.615-620,(1998).
112. M. Mogensen, T. Lindegaard, U.R. Hansen, and G. Mogensen, "Physical Properties of Mixed Conductor Solid Oxide Fuel Cell Anodes of Doped CeO₂", *J. Electrochem. Soc.*, **141** (8), p.2122-2128,(1994).
113. S. Tao and J.T.S. Irvine, "Optimization of Mixed Conducting Properties of Y₂O₃-ZrO₂-TiO₂ and Sc₂O₃-Y₂O₃-ZrO₂-TiO₂ Solid Solutions as Potential SOFC Anode Materials", *J. Solid State Chem.*, **165** (1), p.12-18,(2002).
114. S. Tao and J.T.S. Irvine, "A redox-stable efficient anode for solid-oxide fuel cells", *Nature Materials*, **2**, p.320-323,(2003).
115. J. Canales-Vázquez, S.W. Tao, and J.T.S. Irvine, "Electrical properties in La₂Sr₄Ti₆O_{19.8}: a potential anode for high temperature fuel cells", *Solid State Ionics*, **159** (1-2), p.159-165,(2003).
116. S. Hui and A. Petric, "Conductivity and stability of SrVO₃ and mixed perovskites at low oxygen partial pressures ", *Solid State Ionics*, **143** (3-4), p.275-283,(2001).
117. P. Vernoux, M. Guillo, J. Fouletier, and A. Hammou, "Alternative anode material for gradual methane reforming in solid oxide fuel cells", *Solid State Ionics*, **135** (1-4), p.425-431,(2000).
118. G. Pudmich, B.A. Boukamp, M. Gonzalez-Cuenca, W. Jungen, W. Zipprich, and F. Tietz, "Chromite/titanate based perovskites for application as anodes in solid oxide fuel cells", *Solid State Ionics*, **135** (1-4), p.433-438,(2000).
119. Y.-H. Huang, R.I. Dass, Z.-L. Xing, and J.B. Goodenough, "Double Perovskites as Anode Materials for Solid-Oxide Fuel Cells", *Science*, **312** (14), p.254-257,(2006).
120. O.A. Marina, N.L. Canfield, and J.W. Stevenson, "Thermal, electrical, and electrocatalytical properties of lanthanum-doped strontium titanate", *Solid State Ionics*, **149** (1-2), p.21-28,(2001).
121. P.R. Slater and J.T.S. Irvine, "Synthesis and electrical characterisation of the tetragonal tungsten bronze type phases, (Ba/Sr/Ca/La)_{0.6}M_xNb_{1-x}O_{3-δ} (M=Mg, Ni, Mn, Cr, Fe, In, Sn): evaluation as potential anode materials for solid oxide fuel cells", *Science*, **124** (1-2), p.61-72,(1999).

122. P.R. Slater and J.T.S. Irvine, "Niobium based tetragonal tungsten bronzes as potential anodes for solid oxide fuel cells: synthesis and electrical characterisation", *Science*, **120** (1-4), p.125-134,(1999).
123. C.M. Reich, A. Kaiser, and J.T.S. Irvine, "Niobia Based Rutile Materials as SOFC Anodes", *Fuel Cells*, **1** (3-4), p.249-255,(2001).
124. S. Tao and J.T.S. Irvine, "Discovery and Characterization of Novel Oxide Anodes for Solid Oxide Fuel Cells", *Chem. Record*, **4** (2), p.83-95,(2004).
125. S. Primdahl, J.R. Hansen, L. Grahl-Madsen, and P.H. Larsen, "Sr-Doped LaCrO₃ Anode for Solid Oxide Fuel Cells", *J. Electrochem. Soc.*, **148** (1), p.A74-A81,(2001).
126. A. Magneli, *Ark. Kemi.*, **1**, p.213,(1949).
127. P. Holtappels, J. Bradley, J.T.S. Irvine, A. Kaiser, and M. Mogensen, "Electrochemical Characterization of Ceramic SOFC Anodes", *J. Electrochem. Soc.*, **148** (8), p.A923-A929,(2001).
128. B.D. Madsen and S.A. Barnett. "The influence of Ni Content on Ceramic-Based Solid Oxide Fuel Cell Anodes". in *Solid Oxide Fuel Cells IX*, S.C. Singhal and J. Mizusaki Eds, The Electrochemical Society Proceedings Series: The Electrochemical Society: Pennington NJ, 2005 p.1185-1199.
129. B.D. Madsen, W. Kobsiriphat, Y. Wang, L.D. Marks, and S.A. Barnett, "A Novel Method for Preparing Solid Oxide Fuel Cell Anodes with Nanometer Scale Electrocatalyst Particles", **In preparation**, (2006).
130. A.L. Lee, R.F. Zabransky, and W.J. Huber, "Internal reforming development for solid oxide fuel cells", *Industrial & Engineering Chemistry Research*, **29** (5), p.766 - 773,(1990).
131. G.L. Semin, V.D. Belyaev, A.K. Demin, and V.A. Sobyanin, "Methane conversion to syngas over Pt-based electrode in a solid oxide fuel cell reactor", *Applied Catalysis A: General*, **181** (1), p.131-137,(1999).
132. S. McIntosh, J.M. Vohs, and R.J. Gorte, "Role of Hydrocarbon Deposits in the Enhanced Performance of Direct-Oxidation SOFCs", *J. Electrochem. Soc.*, **150** (4), p.A470-A476,(2003).
133. C. Xia, F. Chen, and M. Liu, "Reduced-Temperature Solid Oxide Fuel Cells Fabricated by Screen Printing", *Electrochem. Solid-State Lett.*, **4** (5), p.A52-A54,(2001).

134. J. Liu and S.A. Barnett, "Thin Yttrium-Stabilized Zirconia Electrolyte Solid Oxide Fuel Cells by Centrifugal Casting", *J. Am. Cer. Soc.*, **85** (12), p.3096-3098,(2002).
135. S.d. Souza, S.J. Visco, and L.C.D. Jonghe, "Reduced-Temperature Solid Oxide Fuel Cell Based on YSZ Thin-Film Electrolyte", *J. Electrochem. Soc.*, **144** (3), p.L35-L37,(1997).
136. S.B. Adler, "Reference Electrode Placement in Thin Solid Electrolytes", *J. Electrochem. Soc.*, **149** (5), p.E166-E172,(2002).
137. J.-H. Koh, B.-S. Kang, H.C. Lim, and Y.-S. Yoo, "Thermodynamic Analysis of Carbon Deposition and Electrochemical Oxidation of Methane for SOFC Anodes", *Electrochem. Solid-State Lett.*, **4** (2), p.A12-A15,(2001).
138. K. Ukai, Y. Mizutani, and Y. Kume. "Current Status of SOFC Development Using Scandia Doped Zirconia". in *Solid Oxide Fuel Cells VII*, H. Yokokawa and S.C. Singhal Eds, The Electrochemical Society Proceedings Series: The Electrochemical Society: Pennington NJ, 2001 p.375-383.
139. C.M. Finnerty, N.J. Coe, R.H. Cunningham, and R.M. Ormerod, "Carbon formation on and deactivation of nickel-based/zirconia anodes in solid oxide fuel cells running on methane", *Catal. Today*, **46** (2-3), p.137-145,(1998).
140. S.B. Adler, J.A. Lane, and B.C.H. Steele, "Electrode Kinetics of Porous Mixed-Conducting Oxygen Electrodes", *J. Electrochem. Soc.*, **143** (11), p.3554-3564,(1996).
141. *Operating Manual of Transpector 2*. 2006: Gas analysis system from Inficon, IPN 074-276.
142. A. Abudula, M. Ihara, H. Komiyama, and K. Yamada, "Oxidation mechanism and effective anode thickness of SOFC for dry methane fuel", *Solid State Ionics*, **86-88** (2), p.1203-1209,(1996).
143. Y. Jiang and A.V. Virkar, "Fuel Composition and Diluent Effect on Gas Transport and Performance of Anode-Supported SOFCs", *J. Electrochem. Soc.*, **150** (7), p.A942-A951,(2003).
144. T. Kawada, I. Anzai, N. Sakai, H. Yokokawa, and M. Fokiys. *High Temperature Electrode Materials and Characterization*, D.D. Macdonald and A.C. Khandkar Eds, The Electrochemical Society Proceedings Series: The Electrochemical Society: Pennington NJ, 1991 p.165.
145. S. Onuma, A. Kaimai, K.-i. Kawamura, Y. Nigara, T. Kawada, J. Mizusaki, H. Inaba, and H. Tagawa, "Electrochemical Oxidation in a CH₄-H₂O System at the Interface of a Pt

- Electrode and Y_2O_3 -Stabilized ZrO_2 Electrolyte ", J. Electrochem. Soc., **145** (9), p.3117-3122,(1998).
146. S. Onuma, A. Kaimai, K.-i. Kawamura, Y. Nigara, T. Kawada, J. Mizusaki, H. Inaba, and H. Tagawa, "Electrochemical Oxidation in a CH_4 - H_2O System at the Interface of a Pt Electrode and Y_2O_3 -Stabilized ZrO_2 Electrolyte ", J. Electrochem. Soc., **145** (3), p.920-925,(1998).
 147. M.L. Toebes, J.H. Bitter, A.J.v. Dillen, and K.P.d. Jong, "Impact of the structure and reactivity of nickel particles on the catalytic growth of carbon nanofibers", Catal. Today, **76** (1), p.33-42,(2002).
 148. V.V. Galvita, V.D. Belyaev, A.K. Demin, and V.A. Sobyanin, "Electrocatalytic conversion of methane to syngas over Ni electrode in a solid oxide electrolyte cell", Applied Catalysis A: General, **165** (1-2), p.301-308,(1997).
 149. A. Weber, B. Sauer, A.C. Müller, D. Herbstritt, and E. Ivers-Tiffée, "Oxidation of H_2 , CO and methane in SOFCs with Ni/YSZ-cermet anodes", Solid State Ionics, **152-153**, p.543-550,(2002).
 150. J.B. Wang, J.-C. Jang, and T.-J. Huang, "Study of Ni-samarium-doped ceria anode for direct oxidation of methane in solid oxide fuel cells", Solid State Ionics, **122** (2), p.122-131,(2003).
 151. Y. Lin, Z. Zhan, J. Liu, and S.A. Barnett, "Direct operation of solid oxide fuel cells with methane fuel", Solid State Ionics, **176** (23-24), p.1827-1835,(2005).
 152. E. Ramírez-Cabrera, A. Atkinson, and D. Chadwick, "Catalytic steam reforming of methane over $Ce_{0.9}Gd_{0.1}O_{2-x}$ ", Applied Catalysis B: Environmental, **47** (2), p.127-131,(2004).
 153. Z. Zhan and S.A. Barnett, "An Octane-Fueled Solid Oxide Fuel Cell", Science, **308**, p.844-847,(2005).
 154. M. Krumpelt and D.-J. Liu, U.S. Patent Application Publication, Cont-n-part of U.S. Serial No. 423,461, p.18,(2004).
 155. U. Balachandran, J.T. Dusek, P.S. Maiya, B. Ma, R.L. Mieville, M.S. Kleefisch, and C.A. Udovich, "Ceramic membrane reactor for converting methane to syngas", Catal. Today, **36** (3), p.265-272,(1997).
 156. P.N. Dyer, R.E. Richards, S.L. Russek, and D.M. Taylor, "Ion transport membrane technology for oxygen separation and syngas production", Solid State Ionics, **134** (1-2), p.21-33,(2000).

157. S. Hamakawa, T. Hayakawa, K. Suzuki, K. Murata, K. Takehira, S. Yoshino, J. Nakamura, and T. Uchijima, "Methane conversion into synthesis gas using an electrochemical membrane reactor", *Solid State Ionics*, **136-137**, p.761-766,(2000).
158. H.J.M. Bouwmeester, "Dense ceramic membranes for methane conversion", *Catal. Today*, **82** (1-4), p.141-150,(2003).
159. T. Ishihara, T. Yamada, T. Akbay, and Y. Takita, "Partial oxidation of methane over fuel cell type reactor for simultaneous generation of synthesis gas and electric power", *Chemical Engineering Science*, **54** (10), p.1535-1540,(1999).
160. V.A. Sobyenin and V.D. Belyaev, "Gas-phase electrocatalysis: methane oxidation to syngas in a solid oxide fuel cell reactor", *Solid State Ionics*, **136-137**, p.747-752,(2000).
161. H.-E. Vollmar, C.-U. Maier, C. Nölscher, T. Merklein, and M. Poppinger, "Innovative concepts for the coproduction of electricity and syngas with solid oxide fuel cells", *J. Power Sources*, **86** (1-2), p.90-97,(2000).
162. X. Zhang, S. Ohara, H. Chen, and T. Fukui, "Conversion of methane to syngas in a solid oxide fuel cell with Ni-SDC anode and LSGM electrolyte", *Fuel*, **81** (8), p.989-996,(2002).
163. J.H. Lunsford, "Catalytic conversion of methane to more useful chemicals and fuels: a challenge for the 21st century", *Catal. Today*, **63** (2-4), p.165-174,(2000).
164. J.R. Rostrup-Nielsen, "Syngas in perspective", *Catal. Today*, **71** (3-4), p.243-247,(2002).
165. D.J. Wilhelm, D.R. Simbeck, A.D. Karp, and R.L. Dickenson, "Syngas production for gas-to-liquids applications: technologies, issues and outlook", *Fuel Processing Technology*, **71** (1-3), p.139-148,(2001).
166. Z. Zhan, J. Liu, and S.A. Barnett, "Operation of anode-supported solid oxide fuel cells on propane-air fuel mixtures", *Applied Catalysis A: General*, **262** (2), p.255-259,(2004).
167. I. Barin and F. Sauert, *Thermochemical data of pure substances*. 1989, New York, NY, USA: Weinheim, Federal Republic of Germany ; VCH.
168. S.A. Barnett, *Direct Hydrocarbon Solid Oxide Fuel Cells. Handbook of Fuel Cell, Fundamentals Technology and Applications, Volume 4*, ed. W. Vielstich, A. Lamm, and H.A. Gasteiger. 2003, West Sussex: John Wiley & Sons Ltd.

169. J.W. Stevenson. "Solid oxide Fuel Cell development in PNNL". in *Solid Oxide Fuel Cells VIII*, S.C. Singhal and M. Dokiya Eds, The Electrochemical Society Proceedings Series: The Electrochemical Society: Pennington NJ, 2003 p.31-39.
170. Z. Zhan, Y. Lin, and S.A. Barnett. "Anode catalyst layers for direct hydrocarbon and internal reforming SOFCs". in *Solid Oxide Fuel Cells IX*, S.C. Singhal and J. Mizusaki Eds, The Electrochemical Society Proceedings Series: The Electrochemical Society: Pennington NJ, 2005 p.1321-1330.
171. Y. Lin and S.A. Barnett, "Anode barrier layers for tubular solid-oxide fuel cells with methane fuel streams", *J. Power Sources*, **161** (1), p.413-419,(2006).
172. T. Ishihara, H. Arikawa, T. Akbay, H. Nishiguchi, and Y. Takita, "Nonstoichiometric $\text{La}_{2-x}\text{GeO}_5$ -delta monoclinic oxide as a new fast oxide ion conductor", *J. Am. Chem. Soc.*, **123** (2), p.203-209,(2001).
173. Z. Bi, B. Yi, Z. Wang, Y. Dong, H. Wu, Y. She, and M. Cheng, "A High-Performance Anode-Supported SOFC with LDC-LSGM Bilayer Electrolytes", *Electrochem. Solid-State Lett.*, **7** (5), p.A105-A107,(2004).
174. J.-H. Wan, J.-Q. Yan, and J.B. Goodenough, "LSGM-Based Solid Oxide Fuel Cell with 1.4 W/cm^2 Power Density and 30 Day Long-Term Stability", *J. Electrochem. Soc.*, **152** (8), p.A1511-A1515,(2005).
175. Z. Bi, M. Cheng, Y. Dong, H. Wu, Y. She, and B. Yi, "Electrochemical evaluation of $\text{La}_{0.6}\text{Sr}_{0.4}\text{CoO}_3$ - $\text{La}_{0.45}\text{Ce}_{0.55}\text{O}_2$ composite cathodes for anode-supported $\text{La}_{0.45}\text{Ce}_{0.55}\text{O}_2$ - $\text{La}_{0.9}\text{Sr}_{0.1}\text{Ga}_{0.8}\text{Mg}_{0.2}\text{O}_{2.85}$ bilayer electrolyte solid oxide fuel cells", *Solid State Ionics*, **176** (7-8), p.655-661,(2005).
176. J. Yan, H. Matsumoto, M. Enoki, and T. Ishihara, "High-Power SOFC Using $\text{La}_{0.9}\text{Sr}_{0.1}\text{Ga}_{0.8}\text{Mg}_{0.2}\text{O}_{3-\text{delta}}/\text{Ce}_{0.8}\text{Sm}_{0.2}\text{O}_2$ Composite Film", *Electrochem. Solid-State Lett.*, **8** (8), p.A389-A391,(2005).
177. J.W. Yan, Z.G. Lu, Y. Jiang, Y.L. Dong, C.Y. Yu, and W.Z. Li, "Fabrication and Testing of a Doped Lanthanum Gallate Electrolyte Thin-Film Solid Oxide Fuel Cell", *J. Electrochem. Soc.*, **149** (9), p.A1132-A1135,(2002).
178. M. Feng, J.B. Goodenough, K. Huang, and C. Milliken, "Fuel cells with doped lanthanum gallate electrolyte", *J. Power Sources*, **63** (1), p.47-51,(1996).
179. K. Huang, R.S. Tichy, and J.B. Goodenough, "Superior Perovskite Oxide-Ion Conductor; Strontium- and Magnesium-Doped LaGaO_3 : I, Phase Relationships and Electrical Properties", *J. Am. Cer. Soc.*, **81** (10), p.2565-2575,(1996).

180. P. VonDollen and S.A. Barnett, "A Study of Screen Printed Yttria-Stabilized Zirconia Layers for Solid Oxide Fuel Cells", *J. Am. Cer. Soc.*, **88** (12), p.3361-3368,(2005).
181. V.V. Kharton, A.P. Viskup, A.A. Yaremchenko, R.T. Baker, B. Gharbage, G.C. Mather, F.M. Figueiredo, E.N. Naumovich, and F.M.B. Marques, "Ionic conductivity of $\text{La}(\text{Sr})\text{Ga}(\text{Mg},\text{M})\text{O}_{3-\delta}$ (M=Ti, Cr, Fe, Co, Ni): effects of transition metal dopants", *Solid State Ionics*, **132** (1-2), p.119-130,(2000).
182. T. Ishihara, T. Shibayama, M. Honda, H. Nishiguchi, and Y. Takita, "Solid oxide fuel cell using Co doped $\text{La}(\text{Sr})\text{Ga}(\text{Mg})\text{O}_3$ perovskite oxide with notably high power density at intermediate temperature", *Chem. Commun.*, **13**, p.1227-1228,(1999).
183. T. Ishihara, T. Shibayama, H. Nishiguchi, and Y. Takita, "Oxide ion conductivity in $\text{La}_{0.8}\text{Sr}_{0.2}\text{Ga}_{0.8}\text{Mg}_{0.2-x}\text{Ni}_x\text{O}_3$ perovskite oxide and application for the electrolyte of solid oxide fuel cells", *J. Mater. Sci.*, **36** (5), p.1125-1131,(2001).
184. T. Ishihara, T. Shibayama, M. Honda, H. Nishiguchi, and Y. Takita, "Intermediate Temperature Solid Oxide Fuel Cells Using LaGaO_3 Electrolyte II. Improvement of Oxide Ion Conductivity and Power Density by Doping Fe for Ga Site of LaGaO_3 ", *J. Electrochem. Soc.*, **147** (4), p.1332-1337,(2000).
185. T. Shimonosono, Y. Hirata, S. Sameshima, and T. Horita, "Electronic Conductivity of La-Doped Ceria Ceramics", *J. Am. Cer. Soc.*, **88** (8), p.2114-2120,(2005).
186. G.-B. Jung, T.-J. Huang, and C.-L. Chang, "Effect of temperature and dopant concentration on the conductivity of samaria-doped ceria electrolyte", *J. Solid State Electrochem.*, **6** (4), p.225-230,(2002).
187. H. Yoshida, H. Deguchi, K. Miura, M. Horiuchi, and T. Inagaki, "Investigation of the relationship between the ionic conductivity and the local structures of singly and doubly doped ceria compounds using EXAFS measurement", *Solid State Ionics*, **140** (3-4), p.191-199,(2001).
188. T. Mori, J. Drennan, J.-H. Lee, J.-G. Li, and T. Ikegami, "Oxide ionic conductivity and microstructures of Sm- or La-doped CeO_2 -based systems", *Solid State Ionics*, **154-155**, p.461-466,(2002).
189. E.P. Murray, M.J. Sever, and S.A. Barnett, "Electrochemical performance of $(\text{La},\text{Sr})(\text{Co},\text{Fe})\text{O}_3$ - $(\text{Ce}, \text{Gd})\text{O}_3$ composite cathodes", *Solid State Ionics*, **148** (1-2), p.27-34,(2002).
190. S.B. Adler, "Factors Governing Oxygen Reduction in Solid Oxide Fuel Cell Cathodes", *Chemical Reviews*, **104** (10), p.4791-4843,(2004).

191. H. Fukunaga, M. Ihara, K. Sakaki, and K. Yamada, "The relationship between overpotential and the three phase boundary length", *Solid State Ionics*, **86-88** (2), p.1179-1185,(1996).
192. A. Naoumidis, A. Ahmad-Khanlou, Z. Samardzija, and D. Kolar, "Chemical interaction and diffusion on interface cathode/electrolyte of SOFC", *Fresenius Journal of Analytical Chemistry*, **365** (1-3), p.277-281,(1999).
193. M.J. Jørgensen, S. Primdahl, C. Bagger, and M. Mogensen, "Effect of sintering temperature on microstructure and performance of LSM- YSZ composite cathodes", *Solid State Ionics*, **139** (1-2), p.1-11,(2001).
194. D. Waller, J.A. Lane, J.A. Kilner, and B.C.H. Steele, "The effect of thermal treatment on the resistance of LSCF electrodes on gadolinia doped ceria electrolytes", *Solid State Ionics*, **86-88** (2), p.767-772,(1996).
195. V. Dusastre and J.A. Kilner, "Optimisation of composite cathodes for intermediate temperature SOFC applications", *Solid State Ionics*, **126** (1-2), p.163-174,(1999).
196. L.J. Van der Pauw, "A method of measuring specific resistivity and Hall effect of discs of arbitrary shape", *Philips Research Reports*, **13** (1), p.1-9,(1958).
197. L.-W. Tai, M.M. Nasrallah, H.U. Anderson, D.M. Sparlin, and S.R. Sehlin, "Structure and electrical properties of $\text{La}_{1-x}\text{Sr}_x\text{Co}_{1-y}\text{Fe}_y\text{O}_3$. Part 2. The system $\text{La}_{1-x}\text{Sr}_x\text{Co}_{0.2}\text{Fe}_{0.8}\text{O}_3$ ", *Solid State Ionics*, **76** (3-4), p.273-283,(1995).
198. A. Esquirol, N.P. Brandon, J.A. Kilner, and M. Mogensen, "Electrochemical Characterization of $\text{La}_{0.6}\text{Sr}_{0.4}\text{Co}_{0.2}\text{Fe}_{0.8}\text{O}_3$ Cathodes for Intermediate-Temperature SOFCs", *J. Electrochem. Soc.*, **151** (11), p.A1847-A1855,(2004).
199. J.V. Herle, A.J. McEvoy, and K.R. Thampi, "A study on the $\text{La}_{1-x}\text{Sr}_x\text{MnO}_3$ oxygen cathode", *Electrochimica Acta*, **41** (9), p.1447-1454,(1996).
200. E.P. Murray and S.A. Barnett, "(La,Sr) MnO_3 -(Ce,Gd) O_{2-x} composite cathodes for solid oxide fuel cells", *Solid State Ionics*, **143** (3-4), p.265-273,(2001).
201. S.P. Jiang and W. Wang, "Sintering and grain growth of (La,Sr) MnO_3 electrodes of solid oxide fuel cells under polarization", *Solid State Ionics*, **176** (13-14), p.1185-1191,(2005).